UNIVERSIDADE ESTADUAL PAULISTA – UNESP
Faculdade de Engenharia e Ciências
Câmpus de Guaratinguetá

SPH analysis of collisions between macroscopic bodies immersed in planetary rings

Advisor: Profº Dr. Rafael Sfair
Co-advisor: Dr. Christoph Schäfer

Author
Patricia Buzzatto Siqueira

Guaratinguetá - SP
2024

Patricia Buzzatto Siqueira

SPH analysis of collisions between macroscopic bodies immersed in planetary rings

Doctoral Thesis presented to the Graduate Program in Physics and Astronomy of the Sao Paolo State University "Júlio de Mesquita Filho" as a partial requirement to obtain the degree of Doctor in Physics and Astronomy

Universidade Estadual Paulista "Júlio de Mesquita Filho"
Graduate Program in Physics and Astronomy

Advisor: Profº Dr. Rafael Sfair
Co-advisor: Dr. Christoph Schäfer

Guaratinguetá - SP
2024

Siqueira, Patricia Buzzatto
S618a SPH analysis of collisions between macroscopic bodies immersed in planetary rings / Patricia Buzzatto Siqueira - Guaratinguetá, 2024.
141 f : il.
Bibliografia: f. 130-139

Tese (Doutorado) – Universidade Estadual Paulista, Faculdade de Engenharia e Ciências de Guaratinguetá, 2024.

Orientador: Prof. Dr. Rafael Sfair

1. Planetas - Órbitas. 2. Poeira cósmica. 3. Satélites. 4. Sistema solar. I. Título.

CDU 523.4(043)

Luciana Máximo
Bibliotecária/CRB-8/3595

unesp

UNIVERSIDADE ESTADUAL PAULISTA
CAMPUS DE GUARATINGUETÁ

PATRÍCIA BUZZATTO SIQUEIRA

ESTA TESE FOI JULGADA ADEQUADA PARA OBTENÇÃO DO TÍTULO DE
"DOUTORA EM FÍSICA"

PROGRAMA: FÍSICA
CURSO: DOUTORADO

APROVADA EM SUA FORMA FINAL PELO PROGRAMA DE PÓS-GRADUAÇÃO

Documento assinado digitalmente
gov.br
ERNESTO VIEIRA NETO
Data: 15/04/2024 15:23:38-0300
Verifique em https://validar.iti.gov.br

Prof. Dr. Ernesto Vieira Neto
Coordenador

B A N C A E X A M I N A D O R A:

Documento assinado digitalmente
gov.br
RAFAEL SFAIR DE OLIVEIRA
Data: 08/02/2024 22:54:02-0300
Verifique em https://validar.iti.gov.br

Prof. Dr. RAFAEL SFAIR DE OLIVEIRA
Orientador - UNESP

Documento assinado digitalmente
gov.br
OTHON CABO WINTER
Data: 14/04/2024 16:04:19-0300
Verifique em https://validar.iti.gov.br

Prof. Dr. OTHON CABO WINTER
UNESP

Documento assinado digitalmente
gov.br
DANIELA CARDOZO MOURAO
Data: 12/04/2024 16:49:51-0300
Verifique em https://validar.iti.gov.br

Profª. Drª. DANIELA CARDOZO MOURÃO
UNESP

ASSINADO DIGITALMENTE
FERNANDO VIRGILIO ROIG
CPF 21313254878
DATA 09/02/2024
A conformidade com a assinatura pode ser verificada em: http://serpro.gov.br/assinador-digital
SERPRO

Prof. Dr. FERNANDO VIRGILIO ROIG
ON

FIRMADO DIGITALMENTE
tuid
CERTIFICACION DIGITAL AVANZADA
GONZALO TANCREDI

Prof. Dr. GONZALO TANCREDI
Universidad de la República

FEVEREIRO de 2024

CURRICULAR DATA

Patricia Buzzatto Siqueira

BIRTH	30/03/1992 - Cachoeira Paulista / SP
FILIATION	Fernando Antorio Rosa de Siqueira Alcineia Aparecida Buzzatto
2019 / 2024	Doctorate in Physics Faculdade de Engenharia e Ciências de Guaratinguetá Universidade Estadual Paulista "Júlio de Mesquita Filho" (UNESP)
2020 / 2021	Split-site doctoral Computational Physics Department and Numerical Particle Methods Group - Eberhard Karls University of Tübingen, Germany
2016 / 2019	Master in Physics Faculdade de Engenharia e Ciências de Guaratinguetá Universidade Estadual Paulista "Júlio de Mesquita Filho" (UNESP)
2011 / 2016	Bachelor in Physics Faculdade de Engenharia e Ciências de Guaratinguetá Universidade Estadual Paulista "Júlio de Mesquita Filho" (UNESP)
2008 / 2010	Technician's license in Industrial Computing Industrial Technical College from Guaratinguetá - São Paulo State University (UNESP)

ACKNOWLEDGEMENTS

My thanks to all family, friends, colleagues, staff and professors at FEG-UNESP, who contributed to the completion of this work. In particular, I would like to thank:

- For all my family who always supported me, even my crazy dreams, they always stayed beside and celebrated every achievement. Especially my mom who has always been an inspiring woman.

- To my best friends, Larissa and Ana Luiza, who have been like a second family to me since high school. They are my safe harbor, and I know that no matter how far I am from them or how long we go without being in touch, I can always rely on them. Their unwavering support and friendship have been invaluable to me throughout this journey.

- To my love Luca who makes me feel special every day, removing all my insecurities and has been a great partner. Thanks for always staying with me, even when it was not easy to deal. Thanks for reading and correcting this thesis, even if it was not your field. You have a great inspiring heart.

- To my friends and classmates who directly or indirectly helped me through this cycle.

  But the principal my great friend Thami whom I miss every day for not being physically close, with nowadays always an ocean between us, you are a spectacular person who is good in all aspects of life, a great friend, an excellent professional, the most creative person I know and so many other things.

  Also to my friends and colleagues Victor and Tiago, this journey would be impossible without you guys. Thank you for all your help, studies together, and research projects, but especially for all the good laughs, parties and celebrations.

- To my advisor and friend Prof. Dr. Rafael Sfair, for the trust, patience, guidance and especially for being one of the best teachers I had during my career. Your enthusiasm and thirst for knowledge make me want to be a better professional. I hope that one day I will be half the human being you are.

- To my co-advisor Dr. Christoph Schaefer for welcoming me in Germany. Your guidance, support, and expertise have been fundamental in the completion of this thesis. The opportunity to work with you and the experiences gained during my time abroad have profoundly enriched both my personal and academic life.

- The examining board for its suggestions and teachings;

This study was financially supported by: Coordenação de Aperfeiçoamento de Pessoal de Nível Superior – Brasil (CAPES) – Finance
Code 001
CAPES-PRINT Process 88887.467295/2019-00
DFG German Research Foundation project 46102036

“To shine like the sun you must burn like it¡‘
(Leona)

Abstract

Planetary rings, a common feature around giant planets, have recently been discovered around centaurs and dwarf planets. These rings often contain azimuthally confined structures known as arcs, associated with increased particle density due to corotation resonances. One well-known example is Saturn's G ring arc, attributed to the Aegaeon satellite's presence and the resonant confinement by Mimas. However, the conventional explanation of dust production by Aegaeon struggles to account for the arc's brightness within the observed period. Our study explores an alternative model of dust generation within planetary rings. Building upon that some of those systems could have macroscopic bodies, below the resolution limit of cameras and have the potential to collide, generating the visible dust or even forming new satellites. For studying the impacts between the macroscopic bodies, we used Smooth Particle Hydrodynamics (SPH) by performing detailed simulations including shock propagation, material modification and gravitational reaccumulation. Unlike previous approaches that assume gravitational regimes Leinhardt and Stewart [2011], we consider a wide range of body sizes, making no geometric constraints on collisions. This approach includes physical properties like fragmentation and porosity that cannot be addressed through N-body simulations alone. Incorporating these properties, we model the collision outcomes, exploring how bodies with such characteristics deform, compress, or fracture based on various strength models. The results of these simulations are critical for understanding the dust production and longevity of objects within planetary rings. Comparing multiple strength models ensures the accuracy of the simulations. The unique properties of planetary ring particles, including mixed ice-rock composition, high porosity, and low material strength, present computational challenges. Our research addresses these challenges by employing a hybrid method, combining detailed SPH simulations with analytical models and N-body simulations to estimate dust production rates. Overall, this work offers a comprehensive approach to understanding dust generation within planetary rings, shedding light on the dynamics and physical properties of macroscopic bodies immersed in planetary rings.

Contents

1 Introduction **10**

2 Theoretical fundaments **13**
2.1 Planetary rings . . . 13
2.2 Dust production models . . . 18
2.3 Analytical collision model . . . 22

3 Smoothed-particle hydrodynamics (SPH) **28**
3.1 Density estimator and continuity equations . . . 29
3.2 The kernel functions convolution . . . 33
3.3 Errors . . . 35
3.4 Solid body mechanics . . . 36
3.4.1 Stress and Strain . . . 37
3.4.2 Material properties - strength, ductility and toughness . . . 42
3.4.3 Damage model for Brittle Materials . . . 46
3.4.4 Porosity . . . 52
3.4.5 Strength models . . . 56

4 Simulations to define the initial conditions. **78**
4.1 Initial conditions . . . 78
4.2 Initial particle arrangement . . . 78
4.3 Different number of neighbors . . . 86
4.4 Plasticity models . . . 88
4.5 Comparison with laboratory experiments . . . 91

5 General rings and arcs simulations **95**
5.1 Simulation Comparison with Analytical Collision Models . . . 95
5.2 Common dynamics and physical properties of rings/arcs . . . 103

6 Formation of small satellite and dust rings at G Arc **109**
6.1 Numerical Setup . . . 110
6.1.1 N-Body simulations . . . 110

6.1.2 SPH simulations 114
6.2 Analysis and discussion 116
6.2.1 Dynamics and evolution of the post-collisional fragments 121

7 Final remarks **128**

Appendices **141**

A Parameters of SPH simulations. **142**

Chapter 1

Introduction

It is a well-established fact that the giant planets in the Solar System are surrounded by rings [de Pater and Lissauer, 2001]. Recently it was discovered that even dwarf planets Haumea [Ortiz et al., 2017] and Quaoar[Morgado et al., 2023], also at centaurs such as Chariko [Braga-Ribas et al., 2014] and Chiron [Ortiz et al., 2015] have this structure.

Neptune's arcs' discovery had shown that planetary rings do not always form azimuthally continuous structures [Hubbard et al., 1986]. In these arcs, the density number of particles is higher than in the neighborhood, resulting in an increment of the detected brightness (or a more pronounced drop in the case of stellar occultations). Also, Cassini spacecraft data revealed that Saturn's rings also have some denser regions, for instance, the arcs of Anthe and Methone [Hedman et al., 2009b]. The most widely accepted mechanism for the existence of arcs is confinement through corotation resonances. This kind of resonance creates stable points so that the particles are azimuthally confined, thus increasing the surface density Hedman et al. [2009a].

Usually, arcs appear brighter when viewed at higher phase angles. This indicates that the particle size distribution that forms these structures is dominated by grains of dust (typically from 0.1 to 10 μm). The arc formation process is generally related to the presence of a satellite. For instance, the G ring arc whose formation is credited to the small Aegaeon satellite and its confinement is due to a corotation resonance with Mimas [Hedman et al., 2007].

Moreover, according to Hedman et al. [2007], collisions with Aegaeon could generate the micrometric particles that populate the G ring. However, Madeira et al. [2018] showed that due to the solar radiation pressure, the dust particles ejected from Aegeon are lost on a scale of a few decades, while the production mechanism requires at least 30,000 years to accumulate enough mass to account for the arc's brilliance.

A more elaborated model of dust generation to explain the formation of the G ring arc has been proposed in Lattari [2019], and it fits with the data collected during a Cassini flyby. The data indicated the existence of a population of macroscopic bodies immersed in the arc, which, although large, would be below the resolution limit of the cameras. These bodies may eventually collide with each other and, depending on the collision parameters, they can fragment (generating more dust) or merge (creating new satellites).

To test this hypothesis, Lattari [2019] conducted N-body simulations to analyze the collision between macroscopic bodies. The collisions were computed using the semi-analytical treatment proposed by Leinhardt and Stewart [2011], which employs a simplified model considering only the collision geometry and the relative speed of the objects, without accounting for information regarding the type of material or internal properties of the bodies.

However, these physical properties cannot be modeled with N-body simulations. A more suitable method to model this kind of system is through hydrodynamic codes, such as a meshfree Lagrangian method, smoothed particle hydrodynamics (SPH), pioneered by Gingold and Monaghan and Lucy in 1977. This method offers the flexibility to model the internal properties based on various parameters, enabling the investigation of material responses across different pressure and temperature ranges.

Bodies within planetary rings typically range from centimeters to a few tens of meters in size. However, existing collisional models in the literature often presume a gravitational regime, implying a minimum size of 100 meters. Therefore, caution is necessary when employing equations like those presented by Leinhardt and Stewart [2011], particularly regarding their validity for smaller bodies. Not all bodies within planetary rings necessarily adhere to a gravitational regime, as fragments of varying sizes can exist in a non-gravitational state Benz and Asphaug [1999]. Moreover, this project aims to analyze collisions across a broad spectrum of body sizes without imposing constraints on collision geometry, as such variations naturally arise from trajectories generated by N-body simulations.

In this study, we will explore certain physical properties of bodies that influence collision outcomes, such as fragmentation and porosity. The efficacy of deformation mechanisms hinges on assumed strength, acting forces, and how bodies with such properties compress or fracture based on strength models. These models are integrated into numerical simulations, aligning closely with outcomes observed in laboratory experiments and explaining orbital dynamics observed through observations. Given that simulation outcomes directly correlate with strength models, it's crucial to compare all available models to derive meaningful results.

The planetary ring's expected physical properties, such as its composite nature comprising ice and rock, considerable porosity, and limited material resilience, present notable computational com-

plexities. Addressing these challenges requires the development of a methodology capable of facilitating in-depth modeling of shock propagation, material alterations, and gravitational reaccumulation. Moreover, this approach must ensure efficient simulation execution within reasonable timeframes while maintaining minimal errors. To achieve this objective, the study will incorporate comprehensive simulations encompassing shock wave dynamics, material transformation processes, and gravitational mass reaccumulation. These simulations will employ a hybrid hydrocode for analyzing small celestial body disruptions during collisions, coupled with the computational techniques of the N-body code.

The outline of this thesis follows this structure: the next chapter explains planetary rings, their features, theories concerning dust production, and collisional models. In the introductory sections (2.1 and 2.2), we introduce systems that may have macroscopic bodies and discuss the primary source of dust production. We explain how to calculate it and understand the possible production mechanisms required to accumulate enough mass for the arc's brightness. The last introductory section (2.3) presents the analytical collision model by Leinhardt and Stewart [2011], one of the most widely used and accepted models. Consequently, we aim to compare our numerical results and verify the validity of macroscopic bodies. Chapter 3 explains the numerical method used in our project, specifically the SPH method based on the MILUPHCUDA code [Schäfer et al., 2016]. Within this chapter, we showcase the primary models necessary for implementing or testing the code. Finally, a dedicated chapter (3) delves into numerical simulations using SPH. We start by presenting numerical tests defining our initial conditions, followed by a comparison of collisional ice bodies with laboratory results. Eventually, we apply these methods to Saturn's G arc and compare our findings with the Leinhardt and Stewart [2011] model. Our analysis includes calculating dust production, identifying fragments remaining in the system after collisions, and outlining the properties necessary for moon-like formations, such as Aegeaon.

Chapter 2

Theoretical fundaments

2.1 Planetary rings

The first time a ring system was observed was in 1610 by Galileo, who discovered this structure around Saturn. However, at that time, the phenomenon was unclear to him and he interpreted it as two moons. Lately, in 1859 Huygens presented the hypothesis that the system seen by Galileo was a solid and elliptic ring. Nevertheless, in 1675, a dark stripe divided the ring into two parts, then Giovanni Domenico Cassini proposed that the rings were composed of a myriad of small satellites, contrary to the old theories. This theory was lately proved by Clerk Maxwell who showed mathematically that a ring around a planet would be stable only if it was composed of small independent particles, opposite to the hypothesis of a continuous ring.

A stellar occultation by Uranus led to the accidental detection of a ring around the planet. Further investigations revealed the presence of rings around Neptune as well. Additionally, an optically thick portion of a faint ring system was observed and identified as arcs. This discovery marks a significant breakthrough in our understanding of planetary ring systems.

A significant breakthrough in our understanding of planetary ring systems occurred with the advent of spacecraft missions, as the limitations of ground-based telescopes' resolution became apparent. The Voyager spacecraft played a crucial role in this progress, as it detected a faint ring around Jupiter during its mission. Furthermore, the Voyager spacecraft's flybys of the outer planets, coupled with ongoing observations from both ground-based and space-based instruments, have unveiled a diverse range of dynamic phenomena within these ring systems [Murray and Dermott, 2000]. Saturn's ring systems have been studied for decades. Murray's 2000 paper discussed their dynamic phenomena. The Voyager I and II missions discovered small inner satellites like Prometheus and external satellites

like Pandora within the rings. They also provided images of bands arranged radially in some regions. These images led to the development of the first models that explain the complex interactions between the rings.

In the past, it was believed that only Gas Giant planets possessed ring structures. However, a significant breakthrough occurred in 2013 when a stellar occultation provided evidence for the existence of a tightly packed and compact ring encircling the small centaur known as Chariklo. This groundbreaking discovery of the Chariklo rings, coupled with the suggestions made by Ruprecht et al. and Ortiz et al. in 2015 regarding the potential presence of rings around Chiron, raises an intriguing question: Could rings also be observed around other minor planets. Furthermore, in 2007, further occultation events of stars may have provided the first glimpse of exoplanetary rings around a giant planet orbiting that particular star. These findings indicate that rings may be more prevalent in the universe than previously believed.

Another important mission was achieved by the Cassini mission, which unveiled a prominent arc positioned at a specific orbital resonance known as the 7:6 corotation eccentricity resonance with Mimas, one of Saturn's moons. The primary focus of Cassini's cameras was to study the abundance of dust particles within this area, ranging in size from 1 to 10 micrometers. However, an intriguing finding emerged when a substantial decrease in the flux of energetic electrons was detected near this arc. This observation strongly suggests the presence of larger celestial bodies, ranging from centimeter- to meter-sized, whose collective mass is equivalent to that of a moonlet rich in ice, estimated to be approximately 100 meters wide.Hedman et al. [2007]

The resolution limitations of the Cassini spacecraft hinder its ability to identify individual particles within the rings, presenting a considerable obstacle in understanding the intriguing discoveries it has made [Tiscareno et al., 2019]. While Cassini's images show the existence of radial bands within the rings, they lack the detail needed to examine individual particles. Delving into the complex dynamics of these particles is not only essential for elucidating Cassini's findings but also holds significance in unraveling the origins of our solar system. Similar processes likely occurred in the protoplanetary disks that formed it, making this research vital for understanding planetary formation.

To determine the physical properties of the planetary rings, valuable insights are gathered through observations made by spacecraft, ground telescopes, and the remarkable Hubble Space Telescope. In particular, data obtained from radio occultations using various wavelengths provide important information about the size of particles within the rings of Saturn and Uranus, spanning a range from approximately 1 cm to 10 m. For narrower size ranges, crucial details are obtained through photometry and differential opacity analyses during stellar occultations. Furthermore, Cassini's Cosmic Dust

Analyzer has provided a direct sampling of the tiniest particles within the rings. The resulting sample size distributions bear a resemblance to the outcomes derived from the catastrophic fragmentation of small solid objects.

The rings exhibit several characteristics indicative of their youthfulness in various planetary systems. Saturn's rings showcase a striking brightness, with the ice components appearing relatively untarnished by meteoritic dust accumulation. Similarly, the rings from Uranus appear to be thin, boasting narrow dimensions. In the case of Neptune, its ring system consists of arcs confined within a limited range of longitudes, suggesting a unique configuration. Lastly, the ring particles surrounding Jupiter are very small, to the extent that their continued existence in the planet's atmosphere is unsustainable, as they will likely succumb to atmospheric drag within a millennium or less.[Esposito, 2014].

To provide visual context, representative images captured by the Voyager spacecraft showcasing the ring systems of the outer planets are presented in Figure 2.1, displaying the ring systems of the outer planets along with the radial positions of their surrounding satellites. Notably, the dashed line indicates the synchronous orbit, which carries important dynamical implications. The prograde satellites located beyond this orbit are subject to tidal forces that lead to a gradual outward drift from the planet, while those situated within it experience an inward motion, ultimately culminating in their disintegration.

The composition and dynamics of dust rings vary across different planetary systems and moons. While some rings are associated with specific moons and contain dust particles originating from those moons, others may consist of interstellar or interplanetary dust captured by the gravitational influence of the planet or moon, or yet with the presence of macroscopic bodies where their collision produces dust. The color and distribution of the rings can provide clues about the size, composition, and surface properties of the dust particles.

Studies conducted by de Pater et al. [2006] have provided insights into the outer rings of Uranus through a comparison of Hubble Space Telescope results with near-infrared observations. These findings have revealed similarities between the rings of Uranus and those of Saturn, particularly in terms of their colors. By utilizing an adaptive optics (AO) system, it is possible to discern the specific colors reflected by the rings. This color information serves as a crucial indicator of the composition and size of the particles present within the rings, shedding light on the origins of these embedded bodies.

The color of the dust particles is influenced by their size relative to the wavelength of light. When the dust particle sizes are smaller or similar to the light wavelength, the particle size effects on reflected

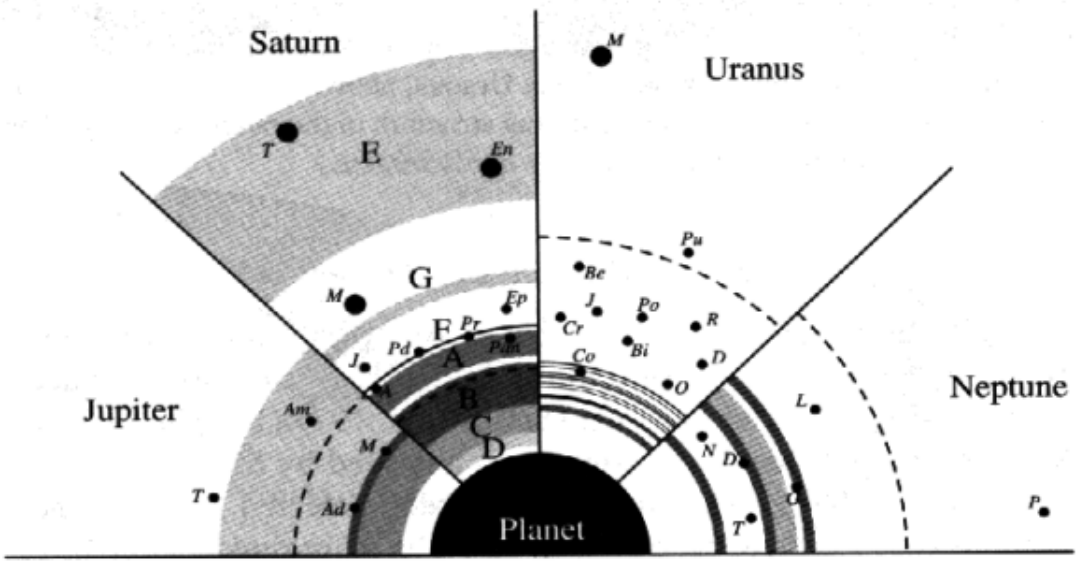


Figure 2.1: The representation of the ring system of the outer planets and their associated moons is standardized to match planetary radii. The dashed curve in the illustration indicates the position of the synchronous orbit for each planet (Murray, 2000).

color become more pronounced than the inherent color of the material. When the distribution of particle sizes within the rings is steeper, with an abundance of tiny dust grains, predominantly blue light is reflected. Conversely, when flatter size distributions are dominated by larger grains, red light is reflected. This phenomenon explains the presence of blue and red colors in the rings of Uranus. Blue is associated with rings most likely built due to its embedded moon, like Saturn's E ring duo to Enceladus, which is the main dust source. Red is usually a color associated with dust, such as Jupiter's ring system and Saturn's G ring. On the other hand, neutral color can be seen in the main rings of Uranus, where particle sizes of $\sim$ 10 cm to 10 m are dominant. de Pater et al. [2006].

Uranus's ν reminds Saturn's G in many ways. Besides the fact both rings reflect the blue color (Figure 2.2), they also have no known source bodies and both rings fall at similar distances from their planets, which peak at 2.77 and 2.63 planetary radius, for Saturn's G and Uranus' ν respectively.

The ν and μ rings of Uranus were effectively detected through forward-scattered visual light by Showalter and Lissauer [2006]. Furthermore, de Pater et al. [2006] conducted analyses on the ratio of brightness between high-phase and low-phase angles, indicating that both rings comprise a substantial quantity of dust particles primarily ranging from sub-millimeter to millimeter sizes. Nevertheless, owing to the influence of different removal and destruction mechanisms on these fine particles, their persistence in the planet's orbit is restricted, requiring an ongoing process of replenishment.

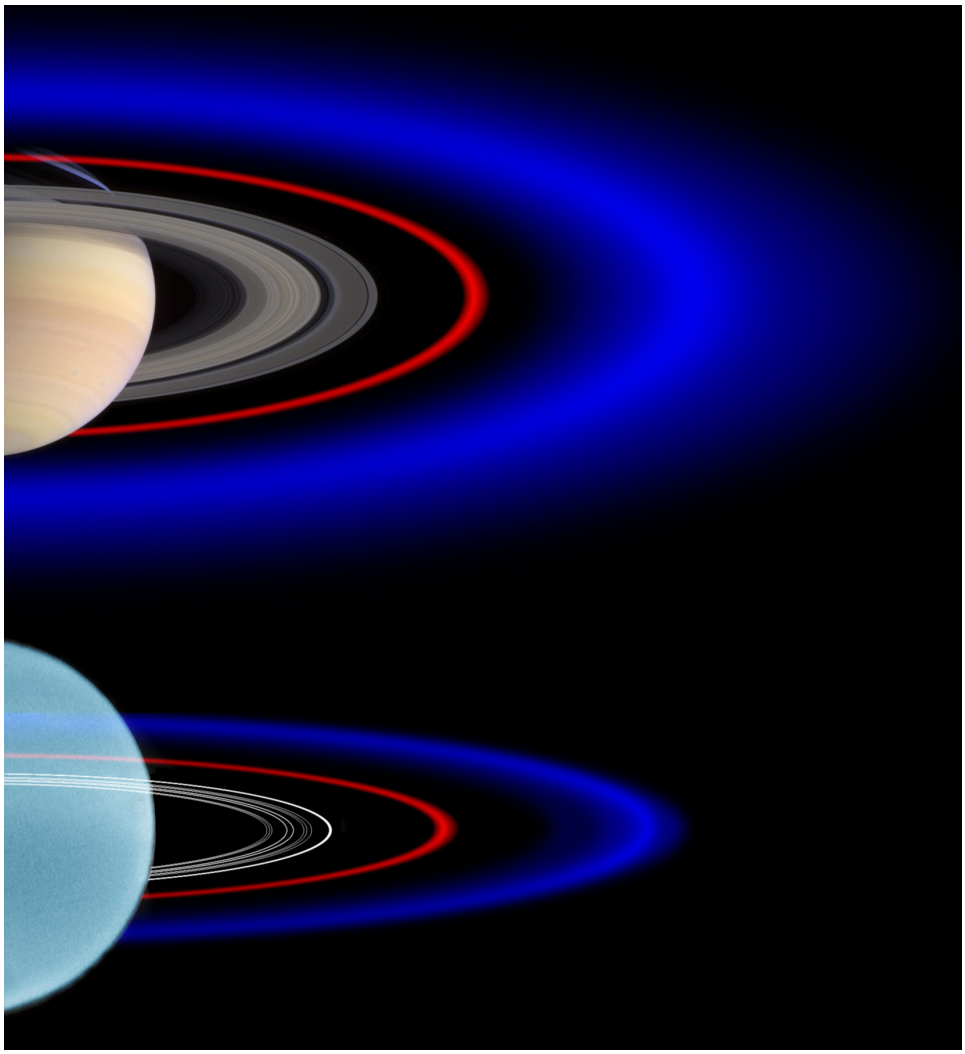


Figure 2.2: A schematic view of the outer rings of Saturn and Uranus, in which each system has been scaled to a common planetary radius. Extract from: de Pater et al. [2006].

The absorption signatures of high-energy protons were detected by the Pioneer 11 spacecraft as it traversed the G ring [Dermott et al., 1980]. The inability of dust grains to absorb such energetic particles suggests the presence of macroscopic bodies, measuring centimeters or larger, within the ring structure [Showalter et al., 1991]. It is plausible that the G ring originated from collisions involving these macroscopic bodies or through meteoroid impacts. A similar process is responsible for the creation of Uranus' μ ring. The observed variations in longitude could arise between gravitational interactions with dust particles and larger bodies, either through resonant interactions or due to the presence of these larger bodies embedded within the ring.

Sfair and Winter [2012] and Showalter and Lissauer [2006] discussed the origin of the μ uranian due to the absence of known embedded source bodies. While the possibility of a single moon existing in the region remains, the current detection threshold suggests that a single moon might not be responsible for creating such a prominent ring. An alternative hypothesis for the dust production in the ν ring proposes the presence of numerous macroscopic bodies between Portia and Rosalind. Collisions among these bodies could be generating the dust observed in the ring. This region lies close to the Roche limit, implying that these bodies may have originated from a disrupted moon unable to recreate, resulting in a transient ring. Significant external impactors might have caused such disruptions, considering that other uranian moons have also experienced disruptions throughout history Colwell and Esposito [1990].

Similar to the faint Saturn G ring, the dust in the arcs of Methone and Anthe also is maintained by an impact-ejecta process. Cassini's observations showed that the Methone and Anthe moons are enveloped by dusty ring-arcs and near Pallene's orbit there is a torus. These moons are most probably the sources of the arcs, being produced by ejecta impacts of interplanetary micrometeoroids of the moons' surface [Sun et al., 2015]. Those moons are tiny and have less than 3km of diameter, due to their sizes, hypervelocity impacts on their surfaces can easily eject material.

In summary, our exploration of planetary ring systems has progressed significantly over the centuries, from Galileo's early observations to recent spacecraft missions like Voyager and Cassini. These discoveries have deepened our understanding of ring dynamics, composition, and origins. Moreover, the discovery of rings around minor planets and exoplanets underscores the widespread presence of such structures. By using different tools and new technology, scientists are eager to learn even more about these fascinating features, advancing our knowledge of how planets form and change in our solar system and beyond.

2.2 Dust production models

In this section, an analytical model for dust production is presented. This method can be used to estimate the efficiency of impacts on an embedded moon by producing dust to populate a ring. With those calculations, it can be determined whether the moon is the main source of the rings or whether a different mechanism is necessary, such as the collision between meter-sized bodies.

Due to the forces acting on the dust particles in the ring, particularly radiation, these forces can remove micrometric particles in a few hundred years. For this reason, it is necessary to have a mechanism to replace the ring continuously and keep the particle population in a steady state.

High-speed collisions are rare, resulting in the inefficiency of generating dust. Low-energy collisions are frequent but insufficient. Then it is necessary for an alternative method that makes it possible to create new particles for the ring, for instance, one mechanism is the collision of micrometeors – or IDPs (Interplanetary Dust Particles).

Sfair and Winter [2012] presented a method to determine the mass production rate given by the flux of interplanetary dust particles (IDPs) onto a satellite's surface. The rate of production of new particles for the ring is directly proportional to the amount of micrometeor effects on the surface of the satellite, which depends on the flux of projectiles in interplanetary space.

To determine the amount of dust generated from collision impacts, it is necessary to characterize the impactors and the targets. However, there is a lack of information from the system, making it necessary to estimate the derived quantities.

IDP density is difficult to measure observationally, so the best way to measure it is locally through spacecraft. Some studies were carried out to determine the amount of solid particles at different heliocentric distances. Grün et al. [1985] using data mostly from near-Earth probes, calculated the flux of IDPs up to 1 g at a distance of 1AU. The extrapolation of these data to other mass values and heliocentric distances was conducted by Colwell and Esposito [1990], while a more elaborate model was developed by Divine [1993].

Krivov et al. [2003] conducted calculations to determine the fluxes of interplanetary grains onto spheres with a unit cross-section ($\pi R^2 = 1$). These spheres were assumed to be moving in circular Keplerian orbits around the Sun at distances of 5.2 and 9.5 AU, corresponding to the heliocentric distances of Jupiter and Saturn, respectively. According to Krivov's model, the mass flux of impactors at Jupiter's heliocentric distance amounts to $F_{imp}^{\infty} = 7.6 \times 10^{-17}$g cm^{-2}s^{-1}, while at Saturn's distance, it is $F_{imp}^{\infty} = 1.8 \times 10^{-17}$g cm^{-2}s^{-1}. The superscript ∞ denotes that these values represent the impactor flux "far" from Jupiter or Saturn.

The flow of mass predominantly originates from particles having masses around 10^{-5} g (equivalent to sizes of approximately 100μm, assuming a bulk density of 2 g cm^{-3}). These particles are categorized as belonging to the "asteroidal population" (characterized by low eccentricities and inclinations) and the "halo population" (exhibiting moderate eccentricities and a wide distribution of inclinations) as defined by Divine's nomenclature.

The impacts of projectiles directly onto the surface of the satellite, the mass production rate (M^+) is given as

$$M^+ = F_{imp} Y S \tag{2.1}$$

where S is the cross-section of the satellite and Y is the ejecta yield.

The alteration of the satellite's surface characteristics affects the efficiency of dust production, which can be quantified through the ejecta yield, denoted as Y. This parameter is defined as the ratio of the overall mass of ejected material to the mass of the impacting object. For a satellite characterized by an exclusively icy surface devoid of silicate components, the ejecta yield can be expressed following the findings of [Koschny, 2001]:

$$Y = 2.64 \times 10^{-5} m_{imp}^{0.23} v_{imp}^{2.46} \tag{2.2}$$

the calculation of Y assumes a typical impactor mass of 10^{-8} kg, which corresponds to a grain with an approximate radius of 100 μm. The velocity parameter, denoted as v_{imp}, is determined by the following relationship:

$$\frac{v_{imp}}{v_{imp}^{\infty}} = \sqrt{1 + \frac{2GM_p}{a(v_{imp}^{\infty})^2}} \tag{2.3}$$

here, M_p represents the mass of the planet, and G is the gravitational constant. Given the characteristics of the IDPs population, the speed of particles away from the planet can be written as

$$v_{imp}^{\infty} = V_p \sqrt{e^2 + i^2} \tag{2.4}$$

where the orbital velocity of the planet is V_p and $e \approx i \approx 0.3$.

In order to determine whether the dust that is visible in the ring comes from the material ejected by the embedded moon, it is crucial to estimate its mass. This estimation is dependent on analyzing the distribution of particle sizes, which is usually represented as a power law function.

$$dN = Cr^{-q}dr \tag{2.5}$$

where $q = 3.5$ is a typical value and the number of particles is dN. The optical depth is

$$\tau = \int_{r_1}^{r_2} d\tau = \int_{r_1}^{r_2} \pi r^2 dN \tag{2.6}$$

and the mass of the dust can be calculated as

$$m = A_{arc} \left(\frac{4}{3} \pi \rho \right) \int_{r_1}^{r_2} r^3 dN \tag{2.7}$$

where A_{arc} is the surface area of the arc.

Hence, by employing the equation denoted as 2.2, we can estimate the mass production rate (M^+) resulting from collisions with a particular embedded satellite. By subsequently comparing this rate with the total mass of a nearby ring or arc, given by equation 2.2, and taking into account the influence of disturbing forces and the time required for populating the ring/arc, we can make a reasoned estimation regarding whether this embedded satellite is the primary source responsible for its formation by presented mechanism.

In the study conducted byMadeira et al. [2018], for instance, they investigated the production of dust grains in the G arc due to impacts with Aegaeon. The rate at which dust grains are generated through the previously discussed method was found to be $M^+ \sim 2 \times 10^{-7}$ kg/s. To analyze the dust distribution in the arc, they made assumptions using a simplified model with a uniform optical depth, denoted as $\tau = 10^{-5}$, predominantly composed of small ice particles ranging in radius from 1 to 10 μm, as expected from the impact process. The total mass of dust in the arc was estimated to be around 2×10^6 kg. Considering the accumulation of dust in the arc over time, the study suggested that without accounting for any loss mechanisms, it would take roughly 30,000 years to reach the calculated mass. However, the inclusion of radiation pressure in the system significantly altered the particle lifetime. For particles with a radius of ten μm, their lifetime reduced to only 26 years, and for particles with a radius of one μm, it further decreased to merely three years. This outcome led Madeira and colleagues to propose the existence of a yet unknown mechanism responsible for

reconstituting the particles in the arc.

2.3 Analytical collision model

In this section, we will describe the scale laws according to Leinhardt and Stewart [2011]. These analytical formulations allow mapping the results of a collision involving two bodies and are determined from the radii and masses of these bodies. From this model is possible to predict the collision outcomes, how the bodies will fragment and the dust generation. We will use them to compare the results of our simulations in SPH to frame the collisions in the appropriate regimes, according to the bodies involved.

During a collision, the angle and velocity of impact, the size of the bodies, and their masses are some of the necessary characteristics to describe the outcome of the impact. For example, a collision with a high impact velocity can cause a loss of mass and destroy part of the target body, thus this collision would fall under a rupture regime. Depending on the angle of impact the damage dealt to the target could be even greater. In the case of a head-on collision, the damage due to the involved mass is greater than in an oblique case. Thus, the impact could be framed in a super-catastrophic rupture regime. However, it is difficult to predict in which regime each collision is found only with the data of the cited parameters. For example, by varying the masses of bodies, a collision with the same impact geometry may have different results. Quantitative analysis would be an even more arduous task, since we want to know, not only how the collisions happened, but also how to calculate the amount of material lost in the impact.

According to Leinhardt and Stewart [2011], erosive regimes have been studied comprehensively in some laboratory studies [Holsapple, 1993, Holsapple et al., 2002]. However, the transition boundaries between the regimes were not demarcated. Leinhardt and Stewart [2011] describes that the impact parameters that made it possible to demarcate the transition between accretion and hit-and-run regimes were only recently established. This was after empirical analysis of more than a thousand hydrocode impact simulations, using an N-body code with finite-sized spherical particles, PKDGRAV [Stadel, 2001].

So we will introduce a summary of how Leinhardt and Stewart [2011] estimate the result of the collision. They divide the collisions into six categories:

- **perfect merging** is when two bodies collide in a perfectly inelastic regime;
- **graze-and-merge** is when the two bodies destroy themselves, and after they agglutinate into

a new one with a mass equal to the total mass of the collision;

- **partial-accretion** occurs when only a fraction of the projectile mass is obtained by the target, while the rest of the projectile mass is spread in smaller objects;
- **partial-erosion** occurs when a small part of the target is lost, and the impact destroys the projectile.

To determine these regimes, we must first define the catastrophic failure criterion, Q'^{*}_{RD}, which represents the failure energy required to disperse half of the total mass taking into account the impact angle and mass ratio of two bodies in a collision. Collision parameters are V_i is the relative velocity, θ is the collision angle, B and l are parameters to determine the effective area of the projectile that interpolates with the target, while R and r are the target and projectile radii, respectively (Figure 2.3).

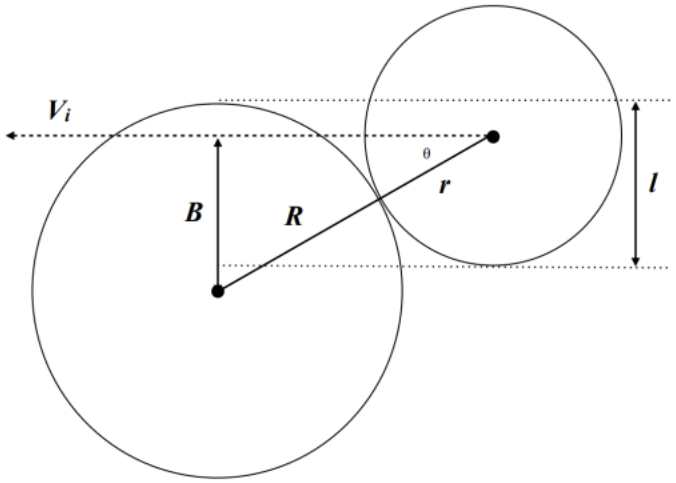


Figure 2.3: Collision geometry, where θ is the impact angle at the time of first contact, $b = \sin\theta$ is the impact parameter and the target is stationary and the projectile is moving from right to left with speed V_i. source: Leinhardt and Stewart [2011]

The specific impact energy at the center of mass is defined, which is given by

$$Q_R = \frac{\mu V_i^2}{2M_{tot}} \tag{2.8}$$

where M_{tot} is the total mass given by $M_{tot} = M_p + M_t$ and $\mu = M_p M_t / M_{tot}$, the indices p and t indicate the projectile and the target, respectively.

The energy necessary to destroy the target (Q^*_{RD}) is proportional to the mass and the relative velocity of the bodies. An empirical equation that determines this energy to a head-on-collision:

$$Q^*_{RD} = q_g(\rho_1 G)^{3\overline{\mu}/2} R_{C1}^{3\overline{\mu}} V^{*(2-3\overline{\mu})} \tag{2.9}$$

where G gravitational constant, V^* is the relative velocity, R_{C_1} is the equivalent radius of a spherical body with total mass M_{tot} and density $\rho_1 \equiv 1000$ kg m^{-3}. The coefficient q_g is about 1 and $\overline{\mu} = 0.36 \mp 0.01$. These parameters were obtained empirically from a large number of simulations with different materials. The variable R_{C1} takes out the dependence on Q^*_{RD} for different radius, densities, and projectile-target mass ratios.

The equation 2.3 assumes that the projectile transfers all the kinetic energy to the target, and the collision is independent of the impact angle. However, to consider oblique impacts and only the mass that interacts with the target, the general catastrophic destruction criteria is

$$Q'^*_{RD} = \left(\frac{\mu}{\mu_\alpha}\right)^{2-3\overline{\mu}/2} Q^*_{RD}. \tag{2.10}$$

where μ_α is a coefficient that considers the impact angle and the mass that interact with the target.

To estimate the mass of the largest body reminiscent of the collision (M_{lr}) as a function of the kinetic energy (Q_r) and the catastrophic destruction energy (Q'^*_{RD}) is determined as

$$\frac{M_{lr}}{M_{tot}} = \begin{cases} -0.5\left(\dfrac{Q_r}{Q'^*_{RD} - 1}\right) + 0.5, & \text{if} \quad Q'^*_{RD} < Q_R, \\ \dfrac{0.1}{1.8^n}\left(\dfrac{Q_r}{Q'^*_{RD}}\right)^n & \text{otherwise.} \end{cases} \tag{2.11}$$

Therefore, it is possible to determine the outcome of the collisions and create a map of the collision regime according to the function of the impact angle and the ratio V_i/V_{esc}, where V_{esc} is the escape velocity defined as

$$V_{esc} = \sqrt{2GM_{tot}/(R_p + R_t)}, \tag{2.12}$$

Also, the critical impact velocity adjusted for different mass ratios and impact angles

$$V^{'*} = \sqrt{2Q'^{*}_{RD} M_{tot}/\mu}. \tag{2.13}$$

Then the collision outcomes in terms of the mass of the largest fragment can be classified as:

i. Perfect merging

$$M_{lr} = M_t$$

ii. Graze-and-merge

$$M_{lr} \cong M_t$$

iii. Hit-and-run

$$M_{lr} = M_{target}$$

iv. Partial accretion

$$M_{target} < M_{lr} < M_t$$

v. Partial erosion

$$0.1M_{tot} < M_{lr} < M_t$$

vi. Super-catastrophic

$$M_{lr} < 0.1M_t$$

The regimes are also delimited by the mass of the largest fragment (M_{lr}) due to the collision. The fragments may either be an intact fragment (in the strength-dominated regime) or a gravitationally

bound aggregate of fragments (gravity-dominated regime) (Figure 2.4). But note that for Leinhardt and Stewart [2011], the model is delimited where both the target and projectile are assumed to be rubble piles: gravitational aggregates with no bulk tensile strength.

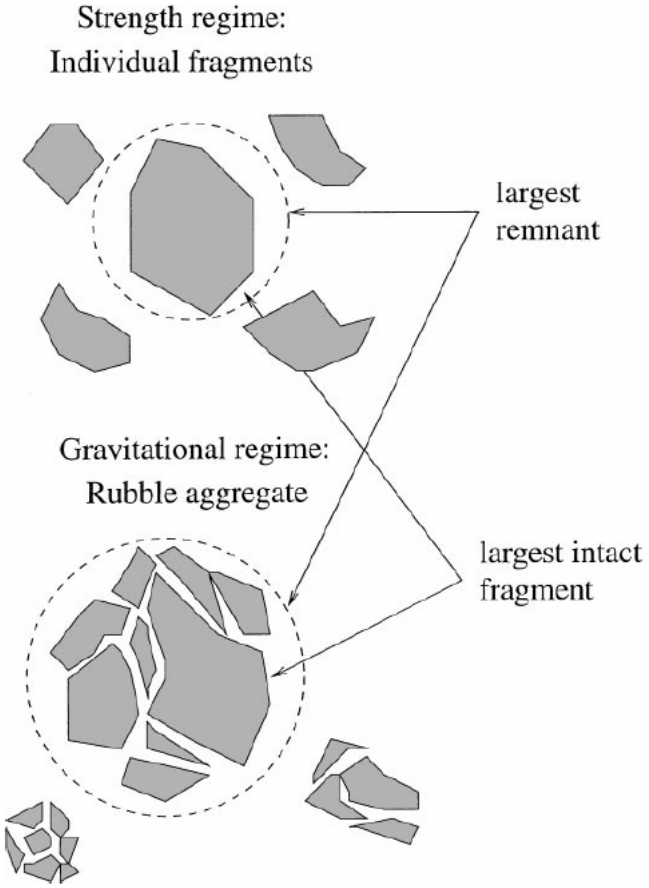


Figure 2.4: In the domain characterized by the regime of strength, the primary outcome consists of a solitary, undamaged fragment. Conversely, within the domain ruled by gravitational forces, the predominant result is an assemblage of fragments, varying in size, that remain bound together due to gravitational attraction Benz and Asphaug [1999]

With the analytical results from Leinhardt and Stewart [2011], it is possible to estimate dust production, cratering, and agglutination for an embedded satellite in a planetary ring. Using only N-body simulation with the analytical model, it is possible to predict what will happen with the bodies inside a ring, but it's not possible to take all the body's physical properties into consideration. In addition, the analytical model is limited to bodies in the gravitational regime, which represents a limitation in our case, since we are also interested in the strength regime case. For this reason, we

will use SPH for our simulations. By doing that we can take into account porosity, the strength of the bodies and reaccumulation in any regime. Since the bodies included in our simulation are near the boundaries of different regimes, we will then compare our results with Leinhardt and Stewart [2011] Also, using the Leinhardt and Stewart [2011] collisional categories, we can also provide our empirical analysis from SPH impact simulations and introduce a surrogate model.

Chapter 3

Smoothed-particle hydrodynamics (SPH)

In this chapter, we introduce the Smooth Particle Hydrodynamics (SPH) numerical method and discuss its application in the field of astrophysics. Also, it will provide a preamble of the formulations of the equations that describe the relevant physics of the problems.

Smooth Particle Hydrodynamics (SPH) is a Lagrangian particle technique initially developed by Lucy [1977] and later refined by Gingold and Monaghan [1977] in the same year. It's called a "Lagrangian particle technique" because it tracks the movement and properties of individual particles as they move through space, rather than focusing on fixed points in a grid. So unlike traditional mesh-based methods, SPH is gridless and meshless, making it well-suited for modeling complex astrophysical phenomena. It discretizes the fluid into particles and interpolates their properties, allowing for accurate and efficient simulation of fluid dynamics.

SPH has become a crucial and widely adopted tool for astrophysical simulations due to its ability to handle irregular boundaries, shock waves, and strong gravitational interactions. It offers valuable insights into various astrophysical phenomena, including galaxy formation, stellar system behavior, and interstellar medium dynamics. The versatility and reliability of the SPH approach have made it an indispensable tool for conducting astrophysical simulations.

At the core of SPH lies the transformation of partial differential equations into ordinary differential equations through kernel interpolation. This step is essential for accurately representing hydrodynamics within the simulation. By employing SPH, we can effectively handle complex geometries and simulate the behavior of fluid flows or solid bodies with high fidelity.

In 1990, the solid-state mechanics for the Smooth Particle Hydrodynamics (SPH) method was first developed by Libersky and Petschek and initially for military applications, this method found utility in shielding research and the study of high-velocity impacts. Over time, numerous researchers

contributed to its enhancement and refinement Libersky et al. [1993], Stellingwerf and Wingate [1994], Randles and Libersky [1996], Libersky et al. [1997]. A significant development in the field occurred when Benz and Asphaug [1994] adapted the solid state mechanics principles to SPH simulations aimed at studying brittle materials for astrophysical scenarios and the collisions between planetesimals Benz and Asphaug [1999], Benz [2000]. This advancement allowed for more accurate investigations into these astrophysical phenomena. Leveraging the SPH method, researchers in the following decade embarked on studying the formation of asteroid families, with contributions from Michel et al. [2001], Michel [2002], Michel et al. [2003, 2004,b], Binzel et al. [2003]. By utilizing SPH, these investigations offered valuable insights into the processes shaping the dynamics of asteroid families.

In this research, we will use the MiluphCUDA code, which has been extensively developed by Dr. Schäfer and a team of researchers associated with the Center for Computational Physics at the University of Tübingen. The MiluphCUDA code, designed for Smooth Particle Hydrodynamics simulations, has undergone recent restructuring, resulting in its latest version being made publicly available [Schäfer et al., 2020][1]. By using MiluphCUDA, we aim to achieve high computational efficiency and precision in our simulations, enabling us to gain deeper insights into solid body dynamics.

MiluphCUDA is a comprehensive computational framework encompassing several specialized modules to facilitate simulations. One of the key modules is dedicated to hydrodynamics, which enables the accurate modeling of gaseous accretion discs. Also, there is the solid module can represent brittle, rocky materials, including smaller planetesimals with non-porous compositions. To further extend the capabilities of the code, the porosity module is incorporated, allowing for simulations of objects with varying levels of porosity, such as asteroids, comets, and objects in the Kuiper belt. When dealing with larger planetesimals or dwarf planets, combining the solid or hydro module with the self-gravity module becomes indispensable. Furthermore, the solid module offers flexibility in selecting different strength models, enabling the representation of materials with distinct properties, such as the modeling of a granular regolith layer covering a brittle and porous asteroid surface. These modules collectively provide a robust framework for conducting advanced simulations.

3.1 Density estimator and continuity equations

Smooth Particle Hydrodynamics (SPH) is founded on the principle of calculating density utilizing a distribution of discrete point mass particles. Various methods can be used to estimate density. Figure 3.1 illustrates the three most common approaches. The basic approach and most straightforward is

[1]Link to the MiluphCUDA repository: https://github.com/christophmschaefer/miluphcuda

a particle-mesh method (Fig. 3.1(a)), which computes the density by interpolating the mass to a grid. However, this approach has its limitations, one arises from the fact a fixed mesh when the mass is very clustered will over or under-sample the particles, also computationally the calculation of the forces needs to be particle-to-particle, implying a non-consistency and a loss of speed and accuracy. An alternative approach to address the issue of a fixed mesh is to calculate the density using local sampling of the mass distribution (as shown in Figure 3.1(b)). However, this method has a significant drawback, making the need to adjust the sampling volume appropriately. As a result, the estimation may be susceptible to noise due to the dependence on the distance of each particle to the volume's boundaries.

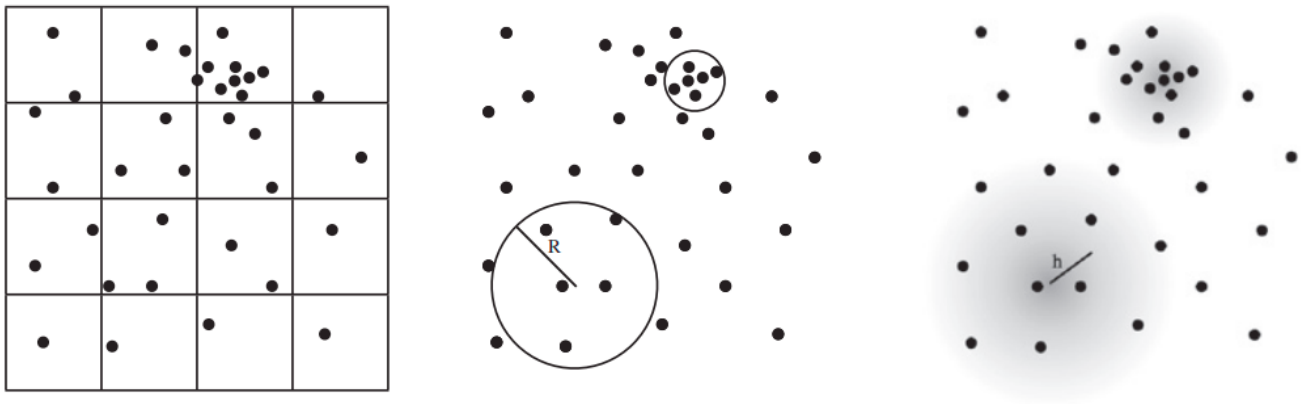


Figure 3.1: Different approaches to calculate the density from a collection of point mass particles. (a) In particle-mesh methods (left panel) (b) a non-mesh method by the local number density of particles scaling the sample volume. (c) This panel shows the approach adopted in SPH, where the density is computed via a weighted sum over neighboring particles, with the weight decreasing with distance from the sample point according to a scale factor h. From: Price [2012]

The last approach is the one SPH adopted (Fig. 3.1(c)), in this method, the density of a particle is estimated by performing a weighted summation over its neighboring particles. Here, m_a represents the mass of the particle, W_{ab} denotes the weight function

$$\rho_a = \sum_{b}^{N_{\text{neigh}}} m_b W_{ab}(x_a - x_b, h_a)$$

where m_a is the mass, W_{ab} is a weight function with dimensions of inverse volume, commonly referred to as the smoothing kernel. Additionally, h_a stands for a scaling factor that varies with distance from

the sample point, dictating the rate of decay of the smoothing kernel, W, concerning the particle spacing, being adapted for each particle-like,

$$h_a^{\nu}\hat{\rho}_a = \text{cte} \tag{3.1}$$

where ν is the number of spatial dimensions.

In SPH, it is of utmost importance to handle any discontinuities within the system, particularly in the context of initial conditions, with great care to ensure numerical stability and accuracy in simulations. One feasible approach to mitigate these issues is to incorporate dissipative terms into the system. By doing so, it is possible to smooth out the discontinuities on a resolvable scale, which is often quantified by a few times the smoothing length, denoted as h.

For evaluating the density, SPH circumvents the direct utilization of the continuity equation as described in equation 3.1. Instead, it involves a transformation of the continuity equation into SPH form. Through this approach, the continuity equation can be reformulated to achieve improved accuracy and consistency within the simulation. To do this, the continuity equation can be rewritten in the form

$$\frac{d\rho}{dt} + \rho\nabla.\vec{v} = 0 \tag{3.2}$$

where the flow of a fluid is described by the thermodynamic field quantities and its velocity field $\vec{v} = \vec{v}(\vec{x}, t)$.

The behavior of a physical system can be explained by certain principles such as the conservation laws for mass, momentum, and energy. These principles result in a group of partial differential equations (PDEs) that govern the system's behavior based on its position $\vec{x}$ and time t. In the SPH method, an effective solution to these PDEs is obtained by transforming them into a system of ordinary differential equations.

Central to the SPH method is the concept of transforming the original PDEs into a more manageable form. This transformation involves performing an averaging process of overall spatial field quantities, accomplished through convolution with a suitable kernel function. Subsequently, the discretization of this averaged representation allows for the practical implementation of SPH.

The nondissipative acceleration equation governing the fluid behavior in SPH can be deduced either from the continuum equations or by utilizing a Lagrangian approach [Gingold and Monaghan,

1977]. In a fluid without dissipation, the acceleration of a particle can be mathematically expressed

$$\frac{d\vec{v_a}}{dt} = -\sum_b m_b \left(\frac{P_a}{\rho_a^2} + \frac{P_b}{\rho_b^2} \right) \nabla_a W_{ab}(b) + \vec{g_a} \tag{3.3}$$

here, P represents the pressure at particles a or b, while $\vec{g_a}$ denotes an external force or mass acting on the system. The utilization of the SPH acceleration equation ensures the preservation of both linear and angular momentum. Furthermore, in the absence of dissipation, the application of SPH Lagrangian leads to the conservation of a discrete form of circulation [Monaghan and Lattanzio, 1985].

In astrophysical simulations using SPH, adding boundary force particles to represent rigid boundaries modifies the SPH equation of motion. This modified equation is referred to as

$$\frac{d\vec{v_a}}{dt} = -\sum_b m_b \left(\frac{P_a}{\rho_a^2} + \frac{P_b}{\rho_b^2} + \Pi_{ab} \right) \nabla_a W_{ab}(b) + \sum_j [\vec{f_{ab}} - m_j \Pi_{aj} \nabla_a W_{aj}] \tag{3.4}$$

following the notation established by Monaghan, involves the inclusion of a term denoted by $\vec{f_{ab}}$. Here, the index j pertains to the label assigned to a boundary force particle, while $\vec{f_{ab}}$ signifies the force per unit mass acting on particle a due to the presence of particle j.

In essence, the equation 3.4 acts as an SPH version of the Navier-Stokes equation, providing a way to introduce forces as an alternate method to represent boundary conditions regarding solid bodies in the simulation framework. This incorporation of boundary forces facilitates the treatment of rigid boundaries and their interactions with other SPH particles in a computationally efficient manner, contributing to the accuracy and robustness of the simulations. The Navier-Stokes equation can be expressed as shown in

$$\frac{dv_i}{dt} = \frac{1}{\rho} \frac{\partial \sigma_{ij}}{\partial x^j} + \frac{1}{\rho} \sigma_{ij} n_j \delta(s) \tag{3.5}$$

The motion of fluid flow is governed by an equation that incorporates the stress tensor, represented by σ_{ij}, a one-dimensional function denoted by $\delta(s)$, the perpendicular distance s from the surface to the specific location where fluid acceleration is sought, and the unit vector n_j that points from the surface into the fluid. The stress tensor σ_{ij} represents the distribution of stresses within the fluid,

while $\delta(s)$ relates to the characteristics of the one-dimensional function along the surface.

The equation represented as 3.4 shows a significant similarity to the equations of molecular dynamics. This similarity is due to the particle method's ability to not only approximate the continuous fluid equations but also provide robust equations for a particle system that effectively mimics the underlying molecular system. It is worth noting that these particle-based equations are more fundamental than the traditional continuum equations [Monaghan and Lattanzio, 1985]. This association between SPH and molecular dynamics holds considerable significance in understanding fluid dynamics at both macroscopic and microscopic scales, thus offering valuable insights for astrophysical investigations.

3.2 The kernel functions convolution

To achieve a successful Smooth Particle Hydrodynamics (SPH) simulation, it is crucial to carefully select the appropriate $W(x, h)$ kernel function and a suitable h smoothing length. The selection of a well-suited smoothing kernel is critical, and it should possess desirable attributes as outlined in [Dehnen and Aly, 2012].

1. It must yield a precise estimation of the density through equation 3.1;
2. The smoothing kernel ($W(x, h)$) must be twice continuously differentiable to ensure smoothness in the forces applied;
3. The SPH simulation should remain stable to paring when considering the desired number N_H of neighbors;
4. Both $\nabla W(x, h)$ and $W(x, h)$ should not impose excessive computational costs.

It is important to note that the first condition, implies $W(x, h)$ gets close to zero as h gets very small, but it also has to stay above zero and decrease steadily as $|x|$ increases. The second condition guarantees the preservation of smooth forces while also requiring that $\nabla W(0) = 0$.

In the first calculations with SPH, Gingold and Monaghan [1977] utilized a Gaussian kernel given by the expression:

$$W(r, h) = \frac{1}{h^d \pi^{d/2}} \exp(-\hat{r}^2/h^2), \tag{3.6}$$

where d represents the dimensionality of the system. It is worth noting that the Gaussian kernel's principal drawback lies in its slow decay to zero for large distances r, resulting in an algorithm with a complexity of N^2, where N signifies the total number of particles within the simulation. Despite this limitation, adopting the Gaussian function as the kernel offers certain advantages, particularly in facilitating a more feasible physical interpretation of the SPH equations, as analytical integrations can be performed effectively.

The standard kernel which is now extensively adopted in the SPH community was introduced by Monaghan and Lattanzio [1985] and is a cubic B-spline function. Its representation is as follows:

$$W(r,h) = \frac{\sigma}{h^d} \begin{cases} 6(r/h)^3 - 6(r/h)^2 + 1) & \text{for} \quad 0 \leq r/h < 1/2 \\ 2(1 - r/h)^3 & \text{for} \quad 1/2 \leq r/h \leq 1 \\ 0 & \text{for} \quad r/h > 1 \end{cases} \tag{3.7}$$

with the normalisation constant σ that depends on the dimension

$$\sigma = \begin{cases} \frac{4}{3} & \text{in one dimension} \\ \frac{40}{7\pi} & \text{in two dimension} \\ \frac{8}{\pi} & \text{in three dimension} \end{cases} \tag{3.8}$$

The kernel's first derivative, a critical component for the SPH algorithm, is expressed as

$$\frac{dW(r,h)}{dr} = \frac{6\sigma}{h^{d+1}} \begin{cases} 3(r/h)^2 - 2(r/h) & \text{for} \quad 0 \leq r/h < 1/2 \\ -(1 - r/h)^2 & \text{for} \quad 1/2 \leq r/h \leq 1 \\ 0 & \text{for} \quad r/h > 1 \end{cases} \tag{3.9}$$

Besides the B-spline, there are several other kernels, these kernels exhibit distinctions primarily in their scaling and are characterized by their unique central values. The lower order among them is the B-splines, which places reduced emphasis on small r values. This is one of the reasons this kernel function is widely used, for instance, the Gaussian functions do not decay rapidly for larger r. On the other hand, Gaussian functions are often quite useful since the integrations can be carried out analytically.

The literature offers limited options for kernels with orders higher than 2. This limitation stems

from the requirement of additional smoothing to encompass a larger number of particles effectively. Consequently, the utilization of such higher-order kernels tends to be less efficient compared to alternative kernel forms. Here was presented only the B-spline because is the one used in our simulations, however, there are others available at MILUPHCUDA, like the Wendland functions (continuity of 2, 4 and 6) and Spiky functions. How to choose a kernel, which one provides the best density estimations and more detailed investigation are at Fulk and Quinn [1996].

3.3 Errors

Many possible numerical errors can arise from an SPH simulation. They can be intrinsically associated with the model being used, the SPH particle distribution, the choice of smoothing kernel, and the number of neighboring particles.

In the SPH particles are not randomly distributed, unlike the Monte Carlo method. However, the complete elimination of particle disorder is challenging, particularly following collision shocks. An initially isotropic particle distribution, when subjected to compression along a specific direction, undergoes anisotropy. Consequently, the SPH force (refer to Equation 3.1) incorporates a stochastic "E_0 error," causing SPH simulations to converge at a slower rate than $\mathcal{O}(h^2)$ [Diehl et al., 2012]. The prevalence of shear flows and shocks in planetary and ring formation scenarios implies that the "E_0 error" could significantly influence the overall performance of astrophysical simulations.

Minimizing the "E_0 error" involves increasing the number N_H of contributing particles. One method is using a smoother, more extended kernel to allow for a larger N_H while maintaining a constant smoothing scale h. However, there are limitations to this approach, even with infinitely extended kernels like the Gaussian kernel. To overcome this, adjusting the smoothing length h becomes necessary, albeit at the expense of particle resolution. This trade-off is preferable to inaccurate outcomes. Achieving a balance between reducing the "E_0 error" and preserving resolution requires careful consideration, guided by thorough testing and convergence studies.

In summary, reducing the "E_0 error" in SPH simulations is crucial for accurate astrophysical modeling. This can be achieved by increasing the number of contributing particles and adjusting the smoothing length while considering the trade-offs between error reduction and resolution preservation. Such decisions should be informed by comprehensive testing and convergence analyses.

3.4 Solid body mechanics

Smoothed Particle Hydrodynamics (SPH) is a computer-based technique that models fluid flows and solid deformations by representing a continuous material as a collection of particles. To simulate the elastic behavior of a solid body within SPH, principles of solid body mechanics, such as deformation and stress, must be integrated into the particle-based framework. The computations follow the core principles of solid mechanics, and various numerical techniques are applied for stability and accuracy in the simulation. The biggest challenge is to accurately capture the complex interactions and behaviors of the material within the particle-based framework and maintain computational efficiency.

Implementing the elastic behavior of a solid body in SPH involves translating the principles of solid mechanics into a particle-based computational approach. These stress calculations, influenced by neighboring particles and weighted by the kernel function, facilitate the determination of forces acting on each particle. These forces encompass both external forces, like gravity, and internal forces due to stress. Consequently, employing Newton's second law, the particles' accelerations are calculated, enabling the simulation to capture their dynamic responses.

Appropriate time integration techniques are employed to update particles' positions and velocities over time. Boundary conditions, including fixed, reflective, or periodic constraints, are incorporated to simulate particle behavior within the desired context. To ensure stability and prevent numerical oscillations, damping mechanisms or stability-enhancing measures may be introduced. This meticulous computational process aligns the particle interactions with the principles of solid mechanics, ensuring the simulation's accuracy and reliability.

A notable application of these principles can be observed in the work of Libersky and Petschek [1990], where equations governing elastic dynamics were established, initially applying Hooke's law. Subsequent studies by Benz and Asphaug [1994, 1995] incorporated these equations alongside a Grady-Kipp fracture model to investigate asteroid impacts and fractures. Remarkable outcomes were observed, exemplified by the simulation of a basalt sphere shattering upon projectile impact. The elasticity equations, paired with techniques to mitigate tension instabilities, were utilized by Gray et al. [2001] for simulations involving bouncing balls and oscillating beams. Extending this approach, Gray and Monaghan [2004] studied fracture around magma chambers, showcasing the algorithm's capacity to simulate damaged beam breakup, rubber ball bouncing, and beam oscillations. Noteworthy advantages of SPH emerged, including the intrinsic carry-over of particle damage and the seamless transition from continuous material to post-impact fragments. This underlines the method's precision for such scenarios.

Moreover, SPH finds application in simulating early solar system events, notably the collision of porous bodies, as evidenced by studies conducted by Jutzi et al. [2008, 2009]. These diverse applications underscore the efficacy of SPH in capturing complex solid mechanics behaviors within a particle-based computational domain. We refer to the thorough description of our implementation in Schäfer et al. [2020].

3.4.1 Stress and Strain

In solid mechanics, the deformation of a solid body is described by the deformation gradient tensor (F), which characterizes the change in the position and shape of material points. To simulate deformation in SPH, it can define a deformation gradient for each particle using its neighboring particles. The gradient can be computed using a kernel function, which quantifies the influence of neighboring particles on a central particle. From the deformation gradient, it is possible to compute the strain tensor (ε) that describes the local deformation.

To analyze how a material responds to external forces, the fundamental principles are stress and strain. Stress, a cornerstone in continuum mechanics, serves as the measure of a material's internal resistance to deformation and is typically defined as the force per unit area acting upon an infinitesimal element within the material. The calculation of stress is pivotal, as it equips us with the capability to anticipate when an object may reach a critical point of failure.

The concept of stress can be further classified into two primary categories: Normal Stress (σ) and Shear Stress (τ). Normal Stress operates perpendicular to the material's surface, while Shear Stress acts parallel to the surface. Mathematically, the intensity of this force, also referred to as the Cauchy stress, is quantified as follows:

$$\sigma = \frac{N}{A}. \tag{3.10}$$

where $A = \pi D^2/4$ is the cross-sectional area. Normal stress can manifest in two principal forms: tensile stress and compressive stress. Tensile stress occurs when external forces act upon a material in a manner that elongates or stretches it. In contrast, compressive stress arises when these forces endeavor to compress or shorten the material. By convention, tensile stresses are regarded as positive values, while compressive stresses are considered negative.

To illustrate this concept further, consider Figure 3.2, which showcases the components of the Cauchy stress matrix. These components manifest as normal and shear stresses exerted on the lateral

surfaces of a stress cube. In a Cartesian coordinate system, the stress cube's sides align parallel to the Cartesian coordinate axes. This representation quantifies the stress states experienced by the material at that specific point.

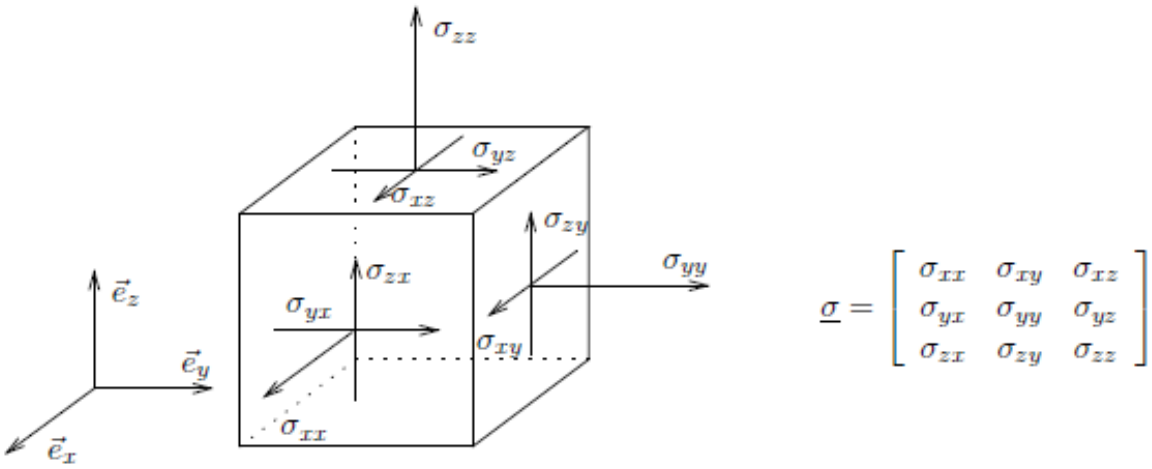


Figure 3.2: Cartesian stress cube. [Schreurs, 2014]

In SPH, stress at a particle is calculated by considering the interactions with neighboring particles. The stress tensor at a particle represents how forces are distributed within the material.

To describe the deformations that occur within a body is strain. As stress, the strain also can be divided into Norman Strain (ϵ), the ratio of the change in length to the original length in the direction of the applied force, and the Shear Strain (γ), the angular deformation due to the shear stress.

Strain provides insight into the degree to which a material has altered its shape and dimensions relative to its initial state. Mathematically, strain (ε) is calculated as the ratio of the change in length, denoted as ΔL, to the original length, represented as L:

$$\varepsilon = \frac{\Delta L}{L}. \tag{3.11}$$

This expression yields a non-dimensional quantity. In practice, strain is often expressed as a percentage, facilitating its intuitive interpretation.

In SPH, calculating the strain of a particular particle relies on analyzing its interactions with its neighboring particles. This method involves closely examining the relative motion and deformation patterns of these adjacent particles. Essentially, it measures how the particles in the system move in relation to each other.

When a material is subjected to loading conditions not aligned with its axis but perpendicular to it, internal forces develop within the material, oriented parallel to the cross-sectional area. These internal forces are termed shear forces. The calculation of shear stress (τ) follows a similar approach to that of normal stress, where the applied shear force (T) is divided by the cross-sectional area (A), as expressed by the equation:

$$\tau = \frac{T}{A}. \tag{3.12}$$

To gain a comprehensive understanding of shear stresses, it is instructive to consider the stresses acting on a small element within the material. When a shear stress is applied to one face of a material element, an equivalent shear stress of the same magnitude and in the opposite direction appears on the opposite face. In addition to these two shear stresses, to maintain rotational equilibrium, two more shear stresses come into play. Collectively, these four shear stresses, all having a magnitude equal to τ, define the shear stresses operating at a specific location within the material.

As an illustrative example, consider the phenomenon of axial torsion applied to a thin-walled tube, as depicted in Figure 3.3. In this scenario, the application of an axial torsional moment, denoted as torque (T), induces a shear stress (τ) within the cross-sectional wall of the tube. It is noteworthy that while the magnitude of this shear stress remains constant at every point across the cross-section, the orientation of the stress cube varies from one point to another due to the circumferential direction of τ. This variation arises from the rotational nature of the applied torque, causing the stress distribution within the material to exhibit distinct orientations at different points within the cross-sectional area.

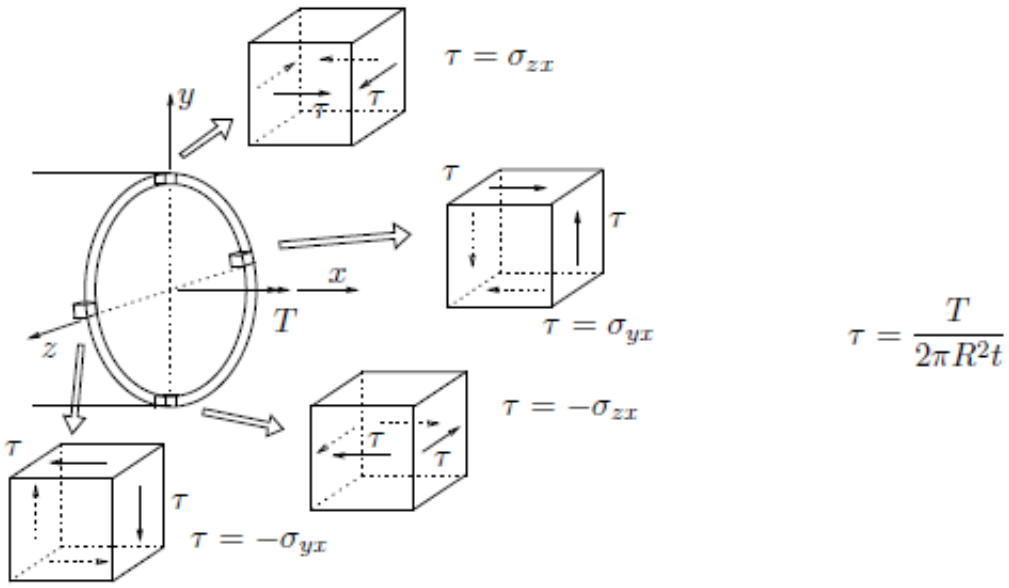


Figure 3.3: Stresses on a small material volume in the wall of a tube under shear loading. [Schreurs, 2014]

There is a deformation, so there is also a shear strain, which is defined as the change in angle shown γ. Shear strain and shear stresses are applied to Hooke's law, but the ratio between them is the shear modulus G instead of Young's modulus as

$$\tau = G\gamma. \tag{3.13}$$

The stress state at a single point within a body will have components in both the normal σ and the shear τ directions. The magnitudes of them will depend on the angle of the plane being used to observe the stresses. If instead, a perpendicular, inclined plane is to cut a material, there will be both normal and shear stress components.

The concepts of stress and strain are intimately linked, and their relationship can be elucidated through the depiction of a stress-strain diagram for a ductile material, as exemplified in Figure 3.4. The stress-strain diagram serves as a tool in defining the solid-body response of materials.

It is imperative to acknowledge that stress-strain diagrams are not universally constant but instead vary across different materials. Each material possesses its unique stress-strain response, shaped by its intrinsic properties. To elucidate these distinctive behaviors, a tensile test serves as an indispensable

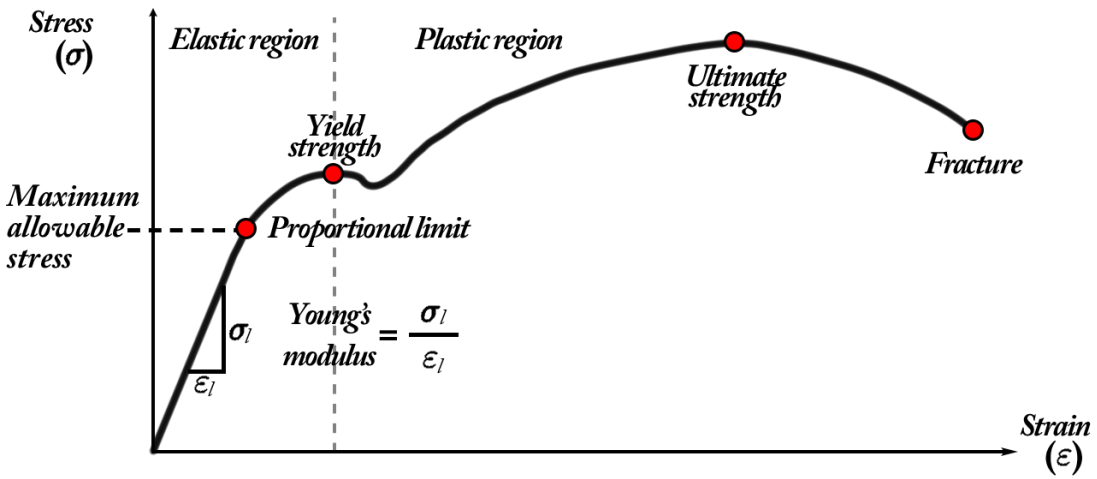


Figure 3.4: Schematic of stress-strain diagram of ductile material. For small stresses, the relation between stress and strain is almost linear (Hooke's law), until the "maximum allowable stress" point. Beyond this point is not linear anymore, but the deformation is still elastic until the "Yield strength" point, then the deformation starts to be plastic. For even larger stresses the material will feel the maximum given by the "Ultimate Strenght", then eventually will break at the "Fracture" point. This behavior helps to identify the difference between ductile and brittle materials, where brittle material exhibits much less plasticity.

tool. This experimental procedure entails the systematic application of forces to the material, while concurrently monitoring and recording the corresponding stress and strain values as the applied force increments.

The linear stress-strain relationship plays a central role in the characterization of a material's mechanical properties, which defines Young's modulus. This modulus serves as a critical indicator of a material's resistance to deformation under load. Materials endowed with low Young's modulus values exhibit a propensity to experience significant strain even at relatively low levels of applied stress. Consequently, such materials have reduced thresholds for maximum allowable stress.

Conversely, materials boasting higher Young's modulus values manifest enhanced stiffness characteristics. These materials can endure greater stress levels before undergoing substantial deformation, thus conferring a heightened capacity to maintain their structural integrity in the face of external forces.

These diagrams reveal distinct regions that characterize the material's response to external forces, shedding light on its elastic and plastic properties. In the initial segment of the stress-strain diagram, characterized by low strain values, a linear relationship between strain and stress becomes evident.

This region signifies a domain where deformations incurred by the material are fully reversible upon the removal of the applied load. This phenomenon is termed elasticity and is rigorously described by Hooke's law, which defines the linear relationship between stress as follows:

$$\sigma = E\varepsilon. \tag{3.14}$$

This equation encapsulates the essence of elasticity, with E representing Young's modulus, a material-specific constant denoting its resistance to deformation. It is important to note that Hooke's law is typically applicable within the context of small strains.

However, as strains increase beyond this initial region, the linear correlation between stress and strain begins to break down. In this regime, deformations are no longer entirely reversible when the applied load is removed. This signifies the onset of permanent plastic deformation within the material, a characteristic feature of ductile materials when subjected to significant stress levels. In essence, the material undergoes structural changes that persist even after the load is relieved, fundamentally altering its shape and properties.

3.4.2 Material properties - strength, ductility and toughness

For materials, strength signifies the capacity to withstand applied stress. This ability to withstand stress is typically characterized by two fundamental parameters: ultimate strength and yield strength. These attributes are discerned through an examination of the stress-strain relationship, as depicted in Figure 3.4, obtained from a tensile test.

The ultimate tensile strength is a parameter that denotes the highest stress level that a material can endure during a tensile test. It represents the peak of the stress-strain curve, signifying the point at which the material fails under extreme stress conditions.

Conversely, the yield strength marks the threshold at which a material embarks on plastic deformation. Beyond this point, applying additional stress will lead to permanent, non-recoverable deformation. Yield strength is a critical criterion for characterizing material failure, and defining the boundary between elastic and plastic behavior. It is essential to note that material failure can occur at stress levels below the yield strength when subjected to varying or cyclic loads over time.

For ductile materials such as mild steel, the yield and ultimate strengths exhibit remarkable similarity in both tensile and compressive directions. Consequently, tensile tests are often preferred over compression tests due to their practicality and ease of execution for these materials. On the

other hand, brittle materials like concrete and ceramics demonstrate significantly higher strength in compression compared to tension, rendering compression tests more relevant for assessing their material properties.

In our project, the macroscopic bodies we are interested in are composed of ice. Ice has been reported to have a strength dependency on the temperature, strain rate, and other factors, being able to have ductile and brittle behavior. The ductile behavior happens at low rates of deformation when the cracks are not able to develop. For higher rates, the material behaves as brittle, and the cracks start to form. For intermediate strain rates, the material is ductile under compression and brittle under tension. The transition between the states occurs for lower strain rates under tension when the cracks open directly for applied stress [Fish, 1991].

Figure 3.5 shows some examples of strength values for a few different materials. Tensile yield strengths are shown for ductile materials and ultimate compressive strengths are shown for brittle materials.

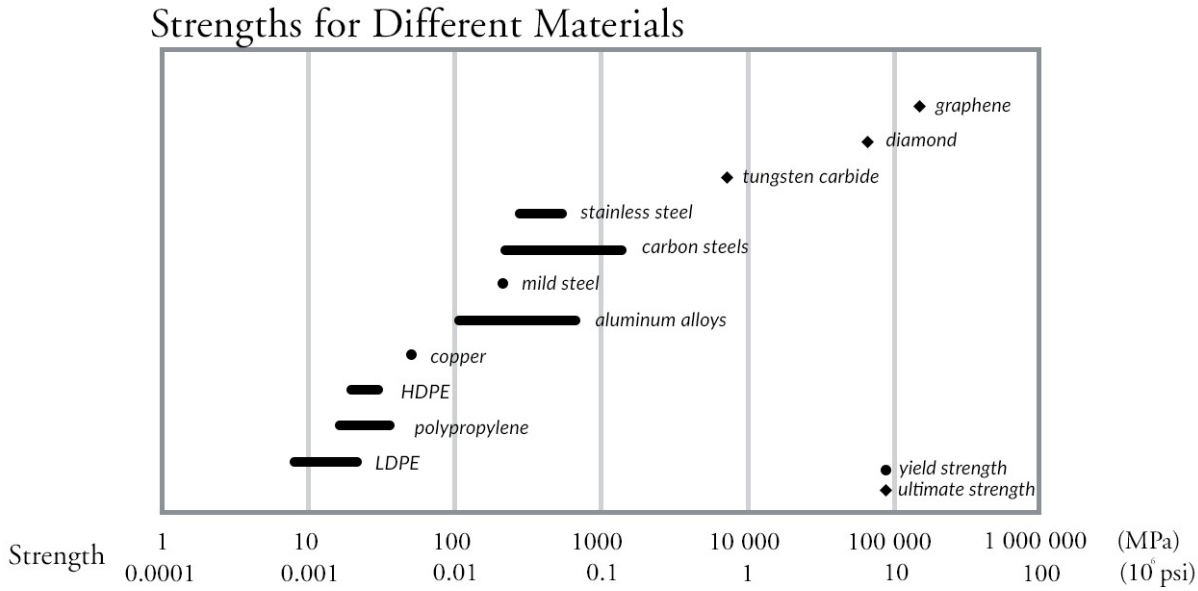


Figure 3.5: Strengths for different materials. Tensile yield strengths are shown for ductile materials and ultimate compressive strengths are shown for brittle materials. Adapted from TheEfficientEngineer.

Ductility, an essential concept in continuum mechanics, serves as a fundamental measure of a material's capacity to undergo plastic deformation before succumbing to fracture. Materials that exhibit substantial plastic deformation before failure, such as mild steel and gold, are categorized as

ductile materials. These materials display fracture at high strains, as visualized in the stress-strain curve depicted in Figure 3.6.

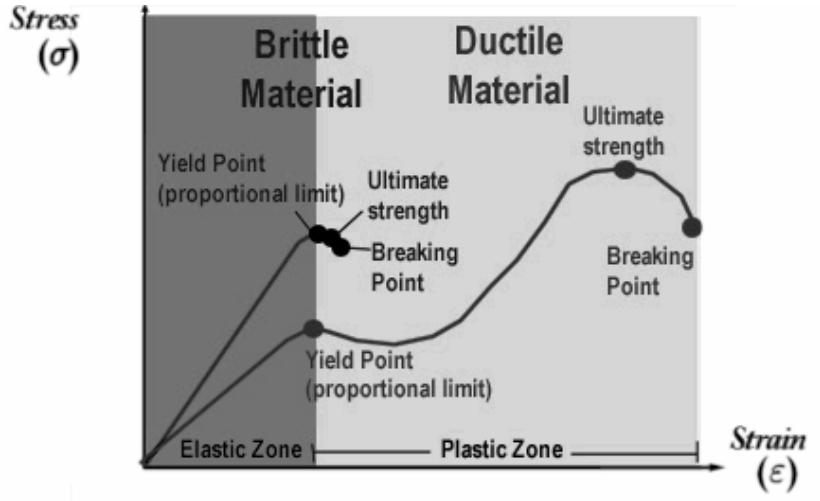


Figure 3.6: Strengths for different materials representing the strain at fracture for brittle and ductile material. Adapted from TheEfficientEngineer

In contrast, materials like glass and ceramics, including porcelain, demonstrate a brittle behavior, characterized by fracture occurring at low strains with minimal plastic deformation. For these materials, the concept of yield strength becomes irrelevant due to their absence of plastic deformation. The demarcation between ductile and brittle behavior is not precisely defined, but materials with a fracture strain of less than 5% are typically considered brittle.

Brittle materials exhibit a notable discrepancy between their behavior in compression and tension. In tension, they are considerably weaker, as tensile loads tend to foster crack propagation and formation. Conversely, compressive loads do not have the same effect. For brittle materials, minimal plastic deformation takes place to redistribute stresses around existing flaws, leading to the accumulation of significant stress concentrations at crack tips, ultimately culminating in fracture. In contrast, ductile materials experience plastic deformation, which mitigates these localized stresses.

It is worth noting that the ductility of a material may be temperature-dependent. Certain steels, for instance, may exhibit ductile behavior at room temperature but transition to a brittle state as the temperature drops below a critical transition temperature. This transition temperature assumes significance as ductile failure is generally preferred over brittle failure in engineering applications.

Toughness represents a material's capacity to absorb energy until it reaches the point of fracture. This can be quantified as the area beneath the stress-strain curve. Materials characterized by a large

area under the curve possess high toughness, indicating their ability to absorb a substantial amount of energy before failing. Achieving high toughness necessitates a balanced combination of ductility and strength. Conversely, materials with low strength or brittle characteristics tend to exhibit lower toughness.

Resilience, another material property, pertains to the ability to absorb energy during elastic deformation, encompassing the area under the stress-strain curve within the elastic region. Materials with high resilience are well-suited for applications where plastic deformation should be minimized to ensure structural integrity.

Figure 3.7 offers a comprehensive representation of material properties, which are of important when analyzing the behavior of materials within the SPH framework. In summary, yield strength denotes the stress at which plastic deformation commences, ultimate tensile strength signifies the maximum stress a material can withstand before rupturing, while ductility measures a material's plastic deformation capacity. Toughness quantifies a material's energy absorption capability until fracture, and resilience assesses its ability to absorb energy during elastic deformation. These material properties are essential when simulating material responses within SPH, aiding in the accurate modeling of various loading conditions and deformations.

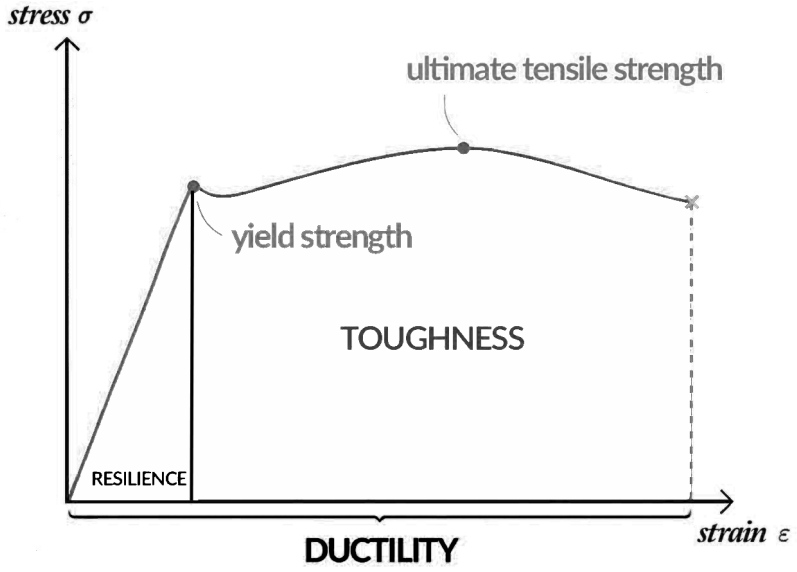


Figure 3.7: Summarize the material properties. Adapted from TheEfficientEngineer

3.4.3 Damage model for Brittle Materials

Fracture can be understood as the consequence of the rupture of atomic or molecular bonds within a material. When an external force is exerted upon a material, exceeding the threshold necessary to disrupt these atomic bonds, the material undergoes fracture, typically giving rise to the formation of cracks.

The theoretical strength of a material can be theoretically determined by analyzing the strength of the atomic bonds holding it together. Nevertheless, it is noteworthy that the theoretical strength, as derived from these atomic bonds, often surpasses the actual material strength observed in experimental settings. This disparity arises due to the inherent imperfections within the crystal lattice of a material, which are commonly referred to as flaws. These flaws represent minor defects within the lattice structure that serve to intensify the applied stress in their immediate vicinity.

It is important to note that the material's failure stress initially manifests at the location of these flaws, even while the remainder of the material is subjected to lower stress levels. Consequently, the initiation of a crack is most likely to occur precisely at the point where the lattice contains such a flaw.

Grady and Kipp [1980] introduced a continuum model for analyzing fragmentation, which was subsequently integrated into SPH simulations by Benz and Asphaug [1995]. This model delves into the behavior of brittle materials, postulating the existence of inherent flaws within them. These flaws play a pivotal role in the initiation and propagation of cracks when subjected to tensile loading. Furthermore, it assumes that the dynamic fracture behavior is intricately linked to the rate at which the material experiences tensile loading.

To elaborate, when a brittle material is subjected to a slow tensile loading, it tends to develop fewer cracks. This happens because at lower strain rates, a single crack is less effective at relieving the relatively modest tensile stress, resulting in a limited activation of flaws and consequently fewer cracks. Contrariwise, when the material experiences higher strain rates, a single crack cannot efficiently mitigate the elevated tensile stress. This leads to the activation of more flaws, giving rise to an increased number of cracks and, in turn, greater overall damage.

To quantify this phenomenon, the model introduced a scalar parameter termed "damage", which is denoted as D, characterizing the extent of damage within a given volume. The permissible range for this parameter is defined as:

$$0 \leq D \leq 1 \tag{3.15}$$

at the lower end of this spectrum, when $D = 0$, it signifies that the material remains unscathed and fully intact, retaining its original structural integrity. In contrast, at the upper limit where $D = 1$, it symbolizes that the material has undergone complete and irreparable damage. In this state, the material becomes impervious to stresses and tensile forces, effectively rendering it akin to a fluid due to its complete fragmentation.

For intermediate values of D, such as $D = 0.5$, the material experiences a degree of damage that corresponds to half of its potential damage under the same tensile strain. In essence, a material with $D = 0.5$ exhibits a reduced capacity to withstand external stresses compared to its undamaged counterpart under equivalent tensile loading conditions. This reduction in strength due to the presence of damage is reflected in the alteration of the elastic stress tensor, $\sigma^{\alpha\beta}$. Specifically, the elastic stress tensor is diminished by a factor of $(1 - D)$, encapsulating the material's compromised structural integrity resulting from the incurred damage or detailed

$$\sigma_d^{\alpha\beta} = -\hat{p}\delta^{\alpha\beta} + (1 - D)S^{\alpha\beta} \tag{3.16}$$

with

$$\hat{p} = \begin{cases} p & \text{for} \quad p \geq 0 \\ (1 - d)p & \text{for} \quad p < 0 \end{cases} \tag{3.17}$$

Grady and Kipp [1980] introduced a damage model considering the presence of structural flaws within a material. This model employs a probability distribution to describe the expected number of flaws per unit volume, denoted as n which possess activation thresholds or failure strains lower than a specified value, ϵ. The foundation for this probability distribution stems from the work of Weibull [1939], who formulated it as a simple power law:

$$n(\epsilon) = k\epsilon^m \tag{3.18}$$

where k and m are the material parameters. The parameter k is measured in units of 1/volume and represents the density of flaws per unit volume.

To establish the cumulative probability distribution of the number of flaws per unit volume, which have activation thresholds lower than ϵ, one can use the following equation:

$$k\epsilon_i^m V = i \tag{3.19}$$

where i represents an integer value (1, 2, ...), signifying the number of flaws with thresholds below ϵ within the entire considered volume V.

By solving for ϵ in terms of i, the equation transforms into:

$$\epsilon_i = \left(\frac{i}{kV}\right)^{1/m}. \tag{3.20}$$

Now, one can progressively compute higher threshold strains, ϵ_i, for i =1,2,... and assign them randomly to SPH particles. This process continues until each SPH particle has been allocated at least one flaw. This allocation strategy aims to prevent the formation of regions within the material where particles are considered indestructible, ensuring a more realistic representation of fracture behavior.

The Grady-Kipp model presents a potential limitation that warrants consideration in the context of SPH simulations, particularly concerning its sensitivity to resolution, defined here as the number of SPH particles utilized in the simulation. It is important to note that the Grady-Kipp model exhibits a non-agnostic behavior concerning resolution. Specifically, as the number of SPH particles increases, a greater number of material flaws are distributed throughout the simulation domain. These flaws are associated with higher threshold strains, and in conjunction with the maximum damage parameter, they collectively contribute to enhancing the material's apparent strength. This effect results in a non-linear relationship between resolution and material strength, wherein higher resolutions tend to yield stronger material responses due to the increased presence of flaws and associated threshold strains.

Furthermore, when comparing different combinations of material parameters represented by (k, m) tuples within the Grady-Kipp model, it is essential to consider the influence of the resolution on the observed material strength. Figure 3.8 illustrates this phenomenon. Notably, the compared

strength values can exhibit variations depending on the position within the Weibull distribution from which the distribution of flaws is sampled. In simpler terms, the choice of (k, m) tuples can lead to varying results in terms of material strength, primarily because the number of required flaws in the distribution influences the overall outcome.

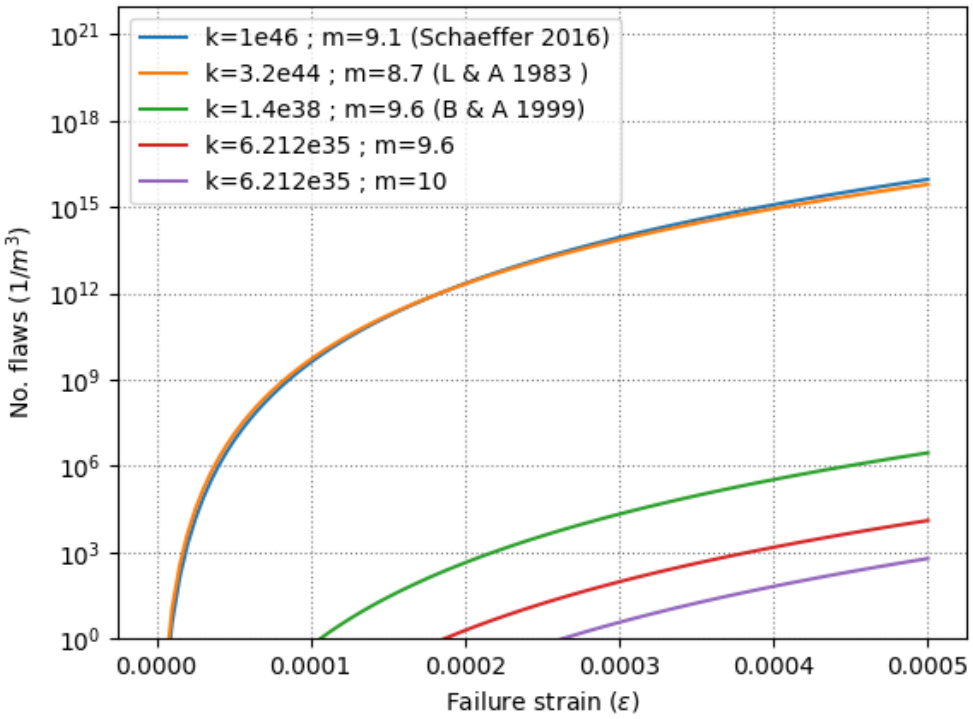


Figure 3.8: Weibull distributions (Eq. 3.18) for the same ice material from different sources varying the values of k and m. Where L&A indicates Lange et al. [1984] and B&A is Benz and Asphaug [1999].

The Weibull parameters k and m can pose substantial challenges, rendering them frequently elusive or imprecisely derived. As a consequence, their values may exhibit disparities not only across diverse materials but also within different variants of the same material.

It is important to emphasize that even when disparate pairs of Weibull parameters (k, m) are employed, they can potentially yield material strength distributions that bear a semblance to one another, albeit in a broad sense. This suggests that there exists a certain degree of variability and versatility in the fracture behavior of materials, with the Weibull parameters serving as influential factors.

It is crucial to recognize that although varying (k, m) combinations for the same material may produce dissimilar probability distributions, they still denote materials with significantly higher strength characteristics when compared to, for instance, water ice as illustrated in Figure 3.8 (adapted from Schäfer et al. [2016]). It should be noted, however, that making generalized conclusions about material strength based solely on lower activation strains can be a complex endeavor. This complexity arises because the resultant material strength is contingent not only upon the Weibull parameters but also on intrinsic elastic properties, notably Young's modulus, which plays a role in the fracture mechanics of materials.

Furthermore, it is crucial to consider the influence of parameter m on material homogeneity and activation thresholds. A higher value of m signifies a material with greater homogeneity, characterized by relatively uniform activation thresholds throughout. Conversely, a lower value of m leads to a broader distribution of activation thresholds within the material.

Benz and Asphaug [1994]have also emphasized the significance of a dimensionless parameter, denoted as ϕ, which is expressed as:

$$\phi = \frac{ln(kV)}{m} \tag{3.21}$$

This parameter ϕ serves as a quantification of low-strain-rate strength, particularly relevant in the context of laboratory rock samples. For typical laboratory rock samples, ϕ tends to converge around the value of 8. As the size parameter, represented by V, increases (indicating larger and potentially weaker rocks), the value of ϕ also increases correspondingly.

It is noteworthy that this trend in ϕ values holds true for various materials. For instance, in the case of basalt, ϕ remains approximately 8, while for water ice, it tends to be around 10. These observations underscore the relevance of ϕ in characterizing the low-strain-rate strength of materials and its potential variations across different substance types.

Material damage initiates when a spherical volume, denoted as $V = \frac{4}{3}\pi R_s^3$ experiences a strain surpassing its minimum activation threshold strain, as described by the following equation:

$$\frac{d}{dt}d^{1/3} = \frac{c_g}{R_s} \tag{3.22}$$

here, c_g represents the constant velocity of crack growth, and its selection is based on a specific criterion. In particular, it is chosen to be 40% of the velocity of a longitudinal elastic wave within

the damaged material, as referenced in Schäfer et al. [2020]:

$$c_g = 0.4\frac{1}{\rho}\sqrt{K_0 + \frac{4}{3}(1-d)\mu} \tag{3.23}$$

When an individual particle experiences a strain exceeding its minimum activation threshold, the damage initiation process is triggered, following the equation 3.22. To incorporate the accumulation of cracks within the particle, the equation is adapted by introducing the number of activated flaws for that particle, denoted as

$$\frac{d}{dt}d^{1/3} = n_{act}\frac{c_g}{R_s} \tag{3.24}$$

each particle within the system exhibits multiple activation thresholds. This inherent characteristic implies that a particle's response to tensile loading will be dictated by the flaw with the lowest activation threshold among the various flaws present. To mitigate the aforementioned scenario wherein a particle's behavior is solely influenced by the flaw with the lowest activation threshold, a critical parameter comes into play: the ratio of activated flaws, denoted as N_{act} to the total number of flaws, represented as N_{tot} within that particular particle. This ratio serves as a fundamental metric that effectively constrains the extent of damage experienced by the particle under the applied load. This relationship can be mathematically expressed as:

$$d_{max} = \frac{N_{act}}{N_{tot}} \tag{3.25}$$

In essence, d_{max} signifies the fraction of activated flaws relative to the total number of flaws within the particle. By monitoring and controlling this ratio, it becomes possible to modulate and limit the extent of damage incurred by the particle during the tensile loading process.

To establish whether a particle exceeds or not its threshold strains in the context of SPH simulations, it is necessary to compute the local scalar strain based on the three-dimensional stress field. This concept, as elucidated in prior work Benz and Asphaug [1995], involves evaluating the local scalar strain (ϵ) by considering the maximum tensile stress (σ_{max}), which is defined as the highest among the principal stresses (σ_γ) obtained through a principal axis transformation of the stress tensor ($\sigma^{\alpha\beta}$). These principal stresses are adjusted to account for the material's yield strength and damage

considerations. Mathematically, this relationship can be expressed as:

$$\epsilon = \frac{\sigma_{max}}{(1-d)E}. \tag{3.26}$$

In this equation, E represents the Young's modulus of the material in an undamaged state, which can be calculated using the shear modulus (μ) and bulk modulus (K) as follows:

$$E = \frac{9K\mu}{3K+\mu}. \tag{3.27}$$

To incorporate the fracture model into our simulation, a preliminary step is essential for distributing activation threshold strains throughout the brittle body. This process entails distributing flaws or activation threshold strains among the SPH particles. To accomplish this, our project adopts the algorithm initially implemented by Benz and Asphaug [1994] and subsequently implemented in the MILUPHCUDA software package. This algorithm randomly assigns flaws to the particles until every particle has been linked to at minimum one activation threshold. It is noteworthy that a particle will only experience complete damage if all of its assigned flaws are triggered.

3.4.4 Porosity

Incorporating porosity into an SPH simulation necessitates the introduction of macroscopic voids at a scale comparable to the particle volume within the initial particle distribution. However, addressing porosity at this sub-resolution level poses significant challenges.

To tackle the modeling of porosity within the SPH framework, two primary approaches are commonly employed to capture micro-porosity phenomena. The first approach involves representing porosity through the characterization of the p - α plane, where 'p' signifies pressure and 'α' represents the degree of porosity. In this approach, the level of porosity is determined based on the applied pressure. Alternatively, the second approach focuses on the α - ε plane, where 'α' denotes porosity, and 'ε' denotes the strain or deformation. In this case, porosity is quantified in correlation with the density of the material.

It is important to note that the crush-curve, which corresponds to the relationship between pressure and porosity, is just one component of a comprehensive porosity model. A fully general porosity model encompasses three key aspects. Firstly, it includes the crush-curve, as mentioned earlier.

Additionally, it accounts for the behavior during unloading from crushed states, which involves understanding how the material responds as it transitions from a crushed to an uncompressed state. Moreover, a comprehensive porosity model considers the material's behavior under tensile stresses after unloading, which involves phenomena such as crack opening. These three components collectively form the basis of a thorough porosity model, as illustrated in Figure 3.9.

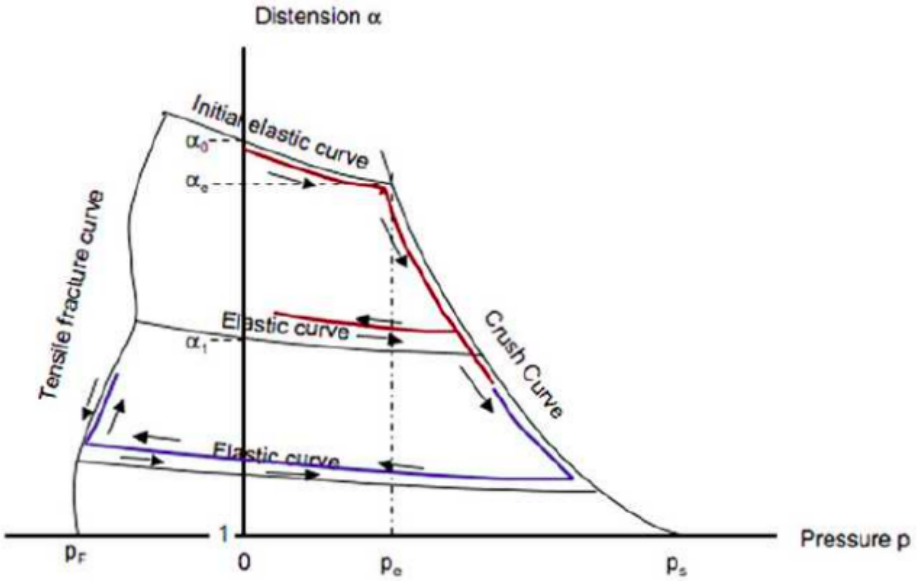


Figure 3.9: Illustration of the p - α plane. Curves for typical porous material at constant temperature of loading and unloading curves. The plot shows the compressing pressure required to crush the material, the elastic unloading curves from the crush curve, and where voids are reintroduced into the material during expansions for the tensile fracture curve. From: [Holsapple, 2009].

P - α model

The p - α-model was originally conceived as a valuable tool for investigating impacts on metallic shielding and subsequently adapted for the analysis of porous structures found in rocky celestial bodies like comets and asteroids. This model serves to establish a connection between the porous pressure, denoted as p, and two critical factors: the solid pressure, denoted as p_s, and the parameter known as distention, represented by α.

Central to this model is the explicit separation of changes in the porous material's volume arising from pore compaction or crushing, and changes in the matrix material's density. The distention parameter α is instrumental in this regard, and it is mathematically defined as follows:

$$\alpha = \frac{\rho_s}{\rho} = \frac{1}{1-\phi} \tag{3.28}$$

ρ_s represents the solid density, ρ stands for the porous density, and ϕ signifies the porosity of the material under consideration.

To compute the porous pressure, an empirically derived equation based on the distention parameter α and the solid material's pressure, denoted as p_s, is employed, as originally documented by [Carroll and Holt, 1972]. This computation can be expressed as:

$$p = \frac{1}{\alpha} p_s(\rho_s, u_s) = \frac{1}{\alpha} p_s(\alpha\rho, u) \tag{3.29}$$

ρ_s and u_s represent the density and energy of the solid material, while ρ and u pertain to the corresponding properties of the porous material under investigation.

One key aspect of the model is that the variation in distention is primarily a function of pressure, delineated into elastic and plastic regimes, depending on whether the changes from parameter α are reversible or irreversible.

Within the plastic regime, alterations in distention due to variations in pressure are often negligible and are typically treated as negligible. Consequently, these changes can be adequately approximated using a simple quadratic form, as characterized by the crush-curve equation:

$$\alpha = 1 + (\alpha_e - 1)\frac{(p_s - p)^2}{(p_s - p_e)^2} \tag{3.30}$$

For a more realistic representation of the plastic regime, especially when comprehensive material data is available, one can turn to static compression data. This data reveals a more intricate relationship and can be described by the following expression:

$$\alpha(p) = \begin{cases} (\alpha_e - \alpha_t)\frac{(p_t - p)^{n1}}{(p_t - p_e)^{n1}} + (\alpha_t - 1)\frac{(p_t - p)^{n2}}{(p_t - p_e)^{n2}} + 1 & \text{if} \quad p_e < p < p_t \\ \frac{(p_t - p)^{n2}}{(p_t - p_e)^{n2}} + 1 & \text{if} \quad p_t \leq p < p_s \\ 1 & \text{if} \quad p \geq p_s \end{cases} \tag{3.31}$$

where p_e signifies the pressure at which the transition occurs from the elastic regime to the plastic regime; p_s corresponds to the pressure at which the porous material becomes fully compacted, resulting in a density equal to the matrix density (i.e., $\alpha = 1$); p_t represents the pressure threshold marking the transition between these two regimes, characterized by different slopes denoted as $n1$ and $n2$ [Jutzi et al., 2009].

The time evolution of compaction/crushing of a porous material can be computed via the distention α. Its rate of change over time (denoted as $\dot{\alpha}$) is governed by the following equation:

$$\dot{\alpha} = \frac{d\alpha}{dp}\frac{dp}{dt} \tag{3.32}$$

Here, the rate of change of porosity ($\dot{\alpha}$) is governed by the derivative of α with respect to pressure (p), multiplied by the rate of pressure change over time ($\frac{dp}{dt}$).

The relationship between the rate of change of porosity and pressure derivative ($\frac{d\alpha}{dp}$) is contingent on the material's behavior in different pressure regimes:

$$d\alpha/dp = \begin{cases} (d\alpha/dp)_{\text{elastic}} & \text{with} \quad p < p_e \\ (d\alpha/dp)_{\text{plastic}} & \text{with} \quad p > p_e \end{cases} \tag{3.33}$$

In the elastic regime (when pressure p is less than p_e), the rate of porosity change is determined by $(d\alpha/dp)_{\text{elastic}}$, while in the plastic regime (when pressure p exceeds p_e), it is governed by $(d\alpha/dp)_{\text{plastic}}$. This demarcation allows for a realistic representation of the material's response to varying pressures.

The integration of Equation 3.32 holds paramount importance as it enables a precise temporal resolution of the compaction process through adaptive timestepping. This approach ensures that the distention follows the prescribed crush curve, while simultaneously regulating and constraining changes in pressure and distention on a per-timestep basis. This control mechanism is critical for maintaining accuracy throughout the simulation.

One aspect of the p-α-model implementation is the verification of timestep validity. If the integrated distention leads to a pressure exceeding the maximum allowable pressure corresponding to the current distention value, it signifies that the timestep was too coarse. In such cases, the crush curve is not accurately replicated, necessitating a reduction in timestep size. To enforce this critical boundary condition, our integrators are equipped with either a distention check or a pressure check function. These functions evaluate the change between the previous and current values of distention

or pressure, and if this change surpasses predefined thresholds, the timestep is automatically reduced. Subsequently, the current step is recalculated using the adjusted timestep, ensuring the fidelity of the simulation results.

In Continuum Mechanics, the incorporation of porosity into models, particularly when addressing micro-porosity, involves the utilization of two primary methodologies. The first method involves the depiction of a crush curve in the p - α plane, as elaborated upon in this context. The second approach revolves around the $\epsilon - \alpha$ plane, where the degree of crushing is defined relative to either the pressure or density. Both these techniques for introducing porosity into a material's behavior have been implemented within the computational framework of MILUPHCUDA.

For our specific application, we have chosen to employ the simpler p - α approach. This decision is grounded in the inherent complexity associated with determining the precise composition of materials within planetary rings. Consequently, the p - α method proves to be more practical, as it demands less detailed knowledge of material composition. This decision is underscored by the ambiguity surrounding the true composition of bodies within planetary rings, hence our focus on a single illustrative case.

However, the crush curve represents just one facet of a comprehensive porosity model consisting of three integral components. In addition to the crush curve, this model necessitates the inclusion of opening cracks, which correspond to unloading curves from crushed states, as well as the material's response to tensile stresses after undergoing unloading. A holistic understanding of porosity demands the consideration of these components, as depicted in Figure 3.9.

3.4.5 Strength models

When subjecting an object to increasing magnitudes of external forces, there exists a critical point at which the material will undergo failure. The question that arises is how to anticipate the precise moment at which static failure will manifest itself. To address this, one must ascertain the threshold at which the internal stresses within the object precipitate its failure. Consequently, our initial task is to establish a clear and comprehensive definition of the concept of failure.

Strength models seek to elucidate the critical points at which materials exhibit structural failure. This occurrence differs substantially for ductile and brittle materials, where the distinction is drawn along the lines of plastic deformation and fracture, respectively. For ductile materials, the point of failure is typically characterized as the initiation of plastic deformation, whereas in the case of brittle materials, it manifests as fracture. These failure criteria are readily defined in scenarios featuring

uniaxial stress states, such as those encountered in tensile testing. Specifically, they manifest when the normal stress within the material attains a magnitude equal to or exceeding the yield strength for ductile materials and the ultimate strength for brittle materials.

Notably, the prediction of these failure points is far from straightforward, primarily due to the inherent complexity of material behavior under various conditions. Consequently, a universal method for failure prediction remains elusive. Instead, practitioners in this field are compelled to rely on a selection process, wherein they choose the most appropriate among a range of distinct failure theories. These theories have been developed through empirical investigation and have proven effective within specific contexts and under particular circumstances.

A failure theory enables us to anticipate when a material might fail. To do this, we examine the stress conditions within the object and compare them to fundamental material properties, like the yield or ultimate strengths of the material, that can be determined through uniaxial tests, as illustrated in Figure 3.10.

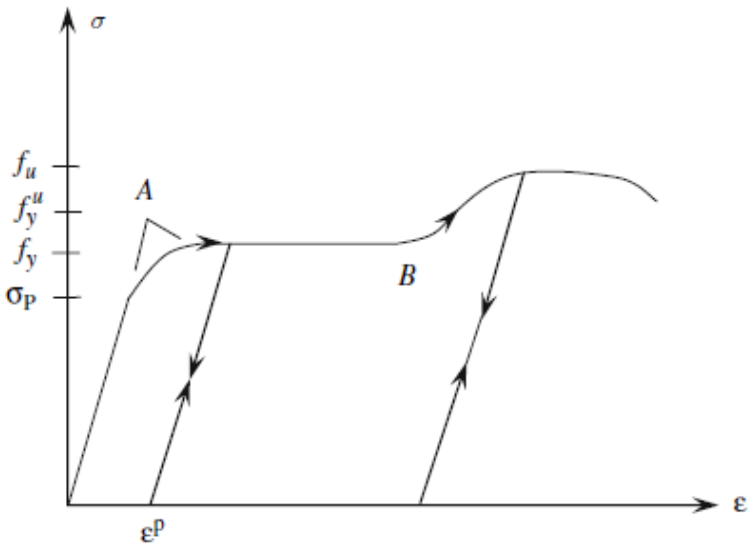


Figure 3.10: Representation of the stress-strain behavior of mild steel under uniaxial tension, illustrating the proportional limit (σ_p), elastic limit (σ_e), yield stress (f_y), upper yield stress (f_y^u), tensile strength (f_u), and plastic strain (ε^p). The sensitivity of f_y^u and the curve between points A and B to loading conditions, particularly loading time, is evident. Adapted from [Irgens, 2008].

Mild steel is characterized by a well-defined yield stress, denoted as its yield strength (f_y). This value marks the point at which the material initiates plastic deformation without a simultaneous increase in stress. Beyond this juncture, identified as point B on the $\sigma\varepsilon$-curve, the material undergoes

a process known as hardening, which necessitates a further increase in stress to induce additional deformation. Ultimately, fracture occurs at the tensile strength (f_u).

Experimental observations have shown that subjecting an elastic stress state to isotropic stress often does not trigger plastic deformation. For instance, experiments have demonstrated that the application of isotropic pressure at a magnitude similar to the yield stress (f_y) does not have a significant impact on the initiation of plastic deformation. These experiments have also revealed that high isotropic pressures can enhance the ductility or yielding capacity of the material [Irgens, 2008].

Two primary objectives are encompassed by the theory of plasticity:

- **Yield Criterion Development:** The primary aim is to create a yield criterion defining stress states marking the shift from pure elasticity to elastic-plastic behavior.
- **Flow Rule Establishment:** The second objective involves establishing a flow rule that elucidates the relationship between stresses and plastic strains.

It is crucial to acknowledge that the theory of plasticity remains a dynamic field of study, with continuous advancements and refinements. This exposition serves as an introductory overview of a segment of the theory that has gained acceptance and practical application.

Within the realm of material behavior, various failure modes exist, each linked to distinct failure mechanisms. For the purposes of this discussion, our focus will be primarily on plastic yielding. When the stress state surpasses the yield limit, a material's response deviates from pure elasticity. Instead, irreversible alterations occur within the material's microstructure, particularly notable in metals where crystallographic slip mechanisms are prevalent. These changes result in permanent deformation, a phenomenon characterized as plastic deformation.

Yield Functions

When stresses surpass the elastic limit of a material, yielding occurs, leading to permanent deformation or even failure. To effectively model this intricate behavior, two primary components come into play:

The first component revolves around the onset of yielding or failure, characterized by the establishment of a yield envelope. This yield envelope serves as a critical reference point, defining the conditions under which yielding or failure initiates. It essentially delineates a limiting stress state beyond which irreversible changes in the material's structure and properties occur. Complementing this is the second component, which deals with how the material behaves once yielding or failure has

been initiated. This entails the formulation of rules governing plastic deformations or crack growth, depending on whether the material exhibits plasticity or brittleness. These rules are instrumental in simulating the post-yielding behavior of materials, providing insights into how they respond to various stress scenarios.

To formulate a yield criterion that effectively distinguishes between purely elastic and yielding material behavior, can be introduced a scalar-valued function denoted as $f[T]$. This function is intricately linked to the stress tensor T and which characterizes material response. The yield criterion for elastic-perfectly plastic materials is expressed by the yield functions ($f[T]$):

$$f[T] = 0 : \text{yield may start} \tag{3.34}$$

$$f[T] < 0 : \text{elastic behavior} \tag{3.35}$$

$$f[T] > 0 : \text{not acceptable} \tag{3.36}$$

which the yield functions is an algebraic combination are presented as of the stress components σ_{ij}. When the material behaves elastically, the yield function is negative, implying that it resides within a three-dimensional stress space. The transition to yielding and plastic behavior is marked by the surface where $f[T] = 0$. Various criteria are frequently employed to characterize yield behavior, among these criteria are the von Mises and Mohr-Coulomb criteria Nadreau and Michel [1986].

The identification of a material's failure point is crucial, which is often defined based on specific stress conditions within the material. Specifically, the octahedral shear stress is often utilized as a characteristic parameter for predicting material failure, or alternatively, the distortion energy can serve as a criterion for failure. A widely recognized yield function that encapsulates these concepts is von Mises' yield function Backhaus [1973]:

$$f[T] = f(\sigma) = \frac{1}{2}[(\sigma_x - \sigma_y)^2 + (\sigma_y - \sigma_z)^2 + (\sigma_z - \sigma_x)^2] + [\tau_{yz}^2 + \tau_{xz}^2 + \tau_{xy}^2] - \sigma_r^2. \tag{3.37}$$

this equation can be rewritten in terms of stress tensor invariants for simplification, leading to:

$$f[T] = f(J_2, J_3) = (I, II, III) \tag{3.38}$$

where J_2 and J_3 are the second and third invariants of the deviatoric stress tensor, respectively, given by the expressions:

$$J_2 \equiv -II' = \frac{1}{2}T' : T' = \frac{1}{2}T'_{ij}T'_{ij} = \frac{1}{2}\left[T : T - \frac{1}{3}(trT)^2\right] \tag{3.39}$$

$$J_3 \equiv III' = detT' \tag{3.40}$$

where only the T' is a deviatoric part of the stress tensor T appears in the yield function $f[T]$:

$$f[T] = f[T'] \tag{3.41}$$

Yield functions's concept is delineated in 3.36 and employing the yield function detailed in 3.38, is visually represented through the yield surface (Fig. 3.11) within of principal stress space. Inside this yield surface reside points denoting purely elastic states. When the stress point remains within this boundary, the material exhibits purely elastic behavior. However, yielding initiates when the stress point reaches and touches the yield surface. Points existing outside this surface are inaccessible under the given conditions. For materials exhibiting hardening behavior, the yield surface is dynamic and capable of shifting and expanding due to the yielding process.

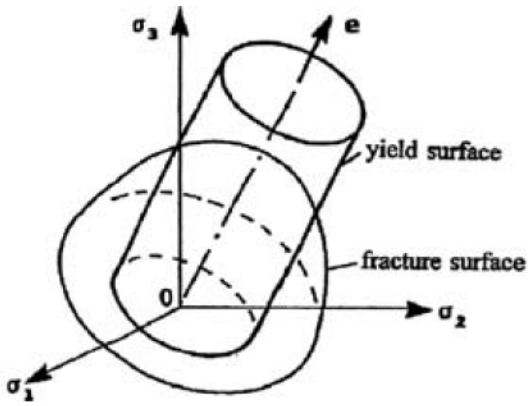


Figure 3.11: Surface indicating yield and fracture within the principal stress space. From: [Irgens, 2008].

The configuration of the yield surface must exhibit a cylindrical form, with its axis aligned parallel to a unit vector. This alignment stems from the property that augmenting an isotropic stress state to a point residing inside the yield surface leads to the stress point's trajectory along a linear path

congruent with a directional vector denoted as $\mathbf{e}$. However, it is important to note that this trajectory will never intersect with the yield surface, as delineated in 3.41.

$$\mathbf{e} = [1, 1, 1] = \frac{1}{\sqrt{3}} \tag{3.42}$$

Additionally, boundaries of the cylindrical yield surface are defined by a fracture surface. Fracture emerges when an inherently non-fracturing stress state experiences the addition of a significantly large isotropic tensile stress. This fracture surface is designed to prevent fracture from compressive isotropic stress. The relationship between the fracture surface and the yield surface is influenced by material properties, temperature, and other factors.

The yield envelope, a fundamental concept in the study of material behavior, is typically expressed by the stress deviator space, denoted as p, and the second invariant of the deviatoric stress tensor, represented as $\sqrt{J_2}$, as depicted in Figure 3.12.

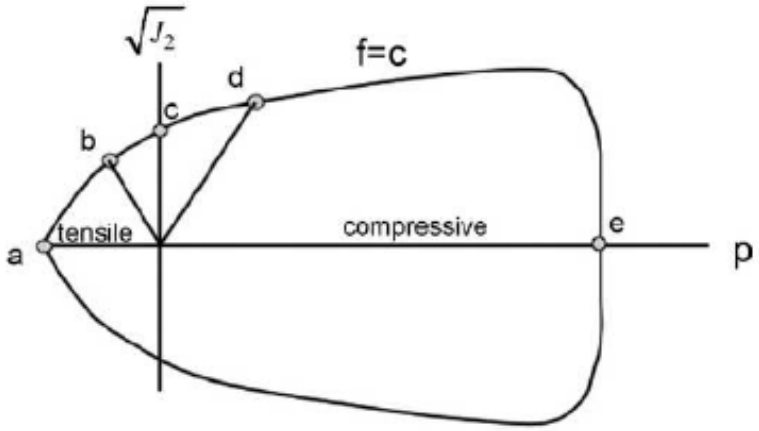


Figure 3.12: Example yield envelope in the $p - \sqrt{J_2}$ space. From: [Holsapple, 2009].

The behavior of materials within this yield envelope varies significantly depending on their nature. Metals, for instance, tend to exhibit plastic deformations once yielding initiates. In such cases, the yield limit typically displays minimal or no sensitivity to confining pressure, although brittle behavior may also manifest, especially at low temperatures. In contrast, geological materials, including rocks, concrete, soil, and granular substances, often exhibit brittle behavior without the presence of significant confining pressures. However, under substantial confining pressures, their behavior can undergo

a dramatic shift towards ductile flow.

Notably, granular materials such as sand and rubble pile asteroids can possess minimal or even zero cohesion (shear strength at zero pressure) while maintaining solid-like characteristics when subjected to confining pressure. This pronounced pressure dependence arises from the internal structure of these materials, leading to increased resistance against particle sliding under compression.

Several basic strength models are commonly employed in the study of material behavior. The von Mises and Tresca models, originally developed to describe the ductile behavior of metals, exhibit no pressure dependence. Extensions of these models, such as the Drucker-Prager and Mohr-Coulomb models, incorporate dependence on confining pressure. These models are primarily based on static yield envelopes.

However, it is important to note that in scenarios involving high loading rates, such as high-velocity collisions and impacts, strain-rate effects can become significant. These effects are naturally considered in crack-growth models for failure, like the Grady-Kipp model, owing to the inherent limitation on crack growth speed.

In the following sections, a comprehensive examination of distinct yield models will be conducted, offering an understanding of their unique attributes and practical utility. Given the inherent diversity of materials and their responses to stress, there is no universally applicable method for predicting failure. Instead, the determination of failure necessitates a selection of a suitable failure theory from a spectrum of distinct theories, each tailored to address specific failure modes, which are fundamentally distinct.

Failure theories, tailored to accommodate the behavior of ductile materials Von Mises, Hill, Gurnson, Hosford, Tresca), often prove unsuitable for the analysis of brittle materials (Rankine, Mohr-Coulomb, Modified Mohr), and conversely, theories devised for brittle materials are typically unsuitable for the study of ductile materials. This distinction arises from the fundamentally different nature of failure mechanisms in these two material categories. Consequently, it becomes imperative to choose a failure theory that aligns with the specific characteristics of the material under investigation, ensuring the accuracy and relevance of the failure prediction process.

von Mises strength model

The von Mises yield criterion was primarily developed to elucidate the behavior of ductile metals. An indispensable requirement for any competent failure theory lies in its harmony with empirical observations regarding the behavior of materials during failure. In the case of ductile materials, the experiments had shown an absence of any yielding due to hydrostatic stresses.

Yield functions originate from categorizing a tri-axial stress state into two groups: those causing alterations in volume (hydrostatic stresses) and those leading to shape distortion. The hydrostatic stresses resemble forces acting on an object immersed in a fluid, with equal values for all three principal stresses and no shear stresses involved. The hydrostatic part in tri-axial stress states is calculated as the mean of these principal stresses. Shear deformation predominantly initiates yielding in ductile materials. In scenarios where shear stresses are lacking, as in situations of hydrostatic stress, the hydrostatic element can be significant yet not contribute to the onset of yielding.

The criterion for failure known as the von Mises criterion, also referred to as the maximum distortion energy theory, was originally formulated by Austrian scientist Richard von Mises. It underwent multiple refinements and could alternatively be named the Maxwell-Huber-Hencky-von Mises theory, owing to contributions from various scientists. This criterion suggests that yielding occurs when the maximum distortion energy within a material matches the distortion energy observed at the point of yielding in a uniaxial tensile test. The equation for computing the distortion energy per unit volume can be derived from the principal stresses in the following manner:

$$u_d = u_{d,y} \tag{3.43}$$

$$u_d = \frac{1+\nu}{6E}\left[(\sigma_1-\sigma_2)^2+(\sigma_2-\sigma_3)^2+(\sigma_3-\sigma_1)^2\right] \tag{3.44}$$

At the point of yielding in a tensile test, the yield strength of the material equals the maximum principal stress, while the remaining two principal stresses both equal to zero:

$$\sigma_1 = \sigma_y \tag{3.45}$$

$$\sigma_2 = \sigma_3 = 0 \tag{3.46}$$

this way the distortion energy is reduced to:

$$u_d = \frac{1+\nu}{6E}\sigma_y^2 \tag{3.47}$$

defining the von Mises failure.

Once again, it is evident that this theory accounts for the disparity in principal stresses, rendering it independent of hydrostatic stress. The formula presented below characterizes this concept:

$$\sqrt{\frac{1}{2}\left[(\sigma_1-\sigma_2)^2+(\sigma_2-\sigma_3)^2+(\sigma_3-\sigma_1)^2\right]} = \sigma_y \tag{3.48}$$

The equivalent von Mises stress, typically situated on the left-hand side of this equation, serves as a common reference in stress assessment. Its surpassing of the material's yield strength means the onset of yielding. Therefore, in finite element method stress analyses, the equivalent von Mises stress stands as a conventional output.

A different method for interpreting the Mises yield criterion involves establishing the Mises stress (σ_M) or the equivalent stress (σ_e), defined as:

$$\sigma_M \equiv \sigma_e = \sqrt{3J_2} \tag{3.49}$$

This stress is also referred to in the literature as the effective stress. using it, the yield criterion can be reformulated as:

$$\sigma_M \equiv \sigma_e = f_y \Leftrightarrow \text{yielding may start} \tag{3.50}$$

Alternatively, the Mises stress σ_M can be interchanged with the octahedral shear stress:

$$\sigma_{oct} = \sqrt{\frac{2}{3}J_2} = \frac{\sqrt{2}}{3}\sigma_M \tag{3.51}$$

This allows us to express the Mises yield criterion differently, as the maximum octahedral shear stress criterion:

$$\sigma_{oct} = \frac{\sqrt{2}}{3} f_y \Leftrightarrow \text{yielding may start} \tag{3.52}$$

For plane stress ($\sigma_3 = 0$), the yield curve is an ellipse in the $\sigma_1\sigma_2$-plane, see Fig. 3.13. The length of the principal axes of the ellipse is $\sqrt{2\sigma_y}$ and $\sqrt{\frac{1}{3}\sigma_y}$.

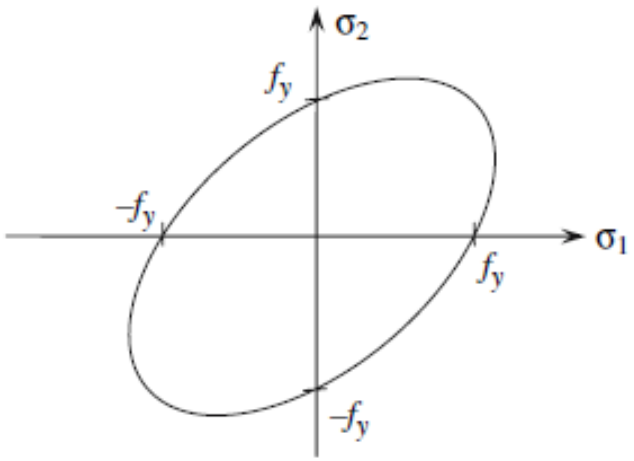


Figure 3.13: Von Mises yield curve in two-dimensional principal stress space. From: [Irgens, 2008].

In three-dimensional principal stress space, the Von Mises yield criterion takes the form of a cylindrical surface. Yielding remains indifferent to hydrostatic stress, resulting in the cylinder aligning with the hydrostatic axis where $\sigma_1 = \sigma_2 = \sigma_3$. Within the π-plane, this criterion forms a circular shape, characterized by a radius of $\sqrt{\frac{2}{3}\sigma_y}$.

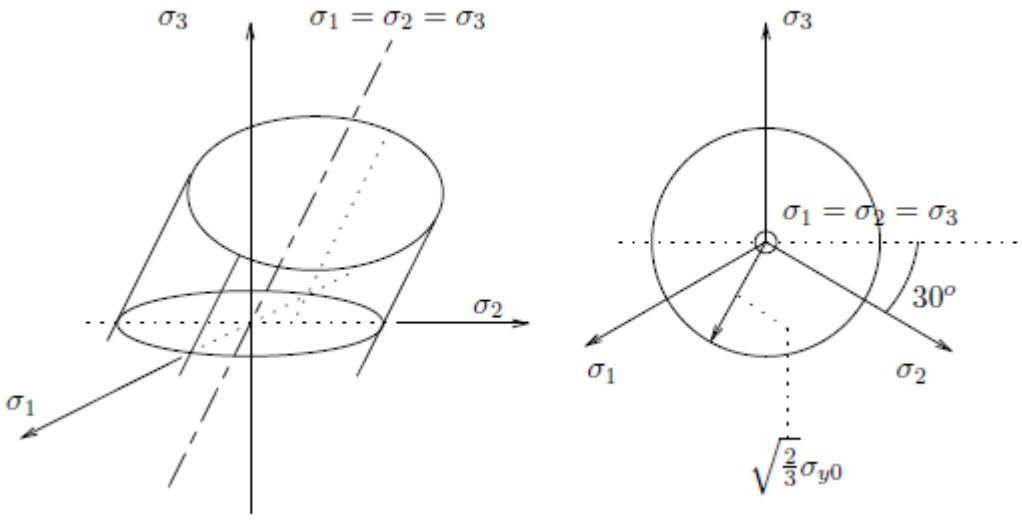


Figure 3.14: Von Mises yield surface in three-dimensional principal stress space and the *pi*-plane. From: [Schreurs, 2014].

Mohr-Coulomb model

The distinction between failure in brittle and ductile materials is significant. Unlike ductile materials that yield, brittle materials predominantly fail through fracture. Additionally, in contrast to ductile materials, brittle ones often exhibit compressive strengths far exceeding their tensile strengths (Fig. 3.15). Any failure theory for brittle materials must encompass these critical differences.

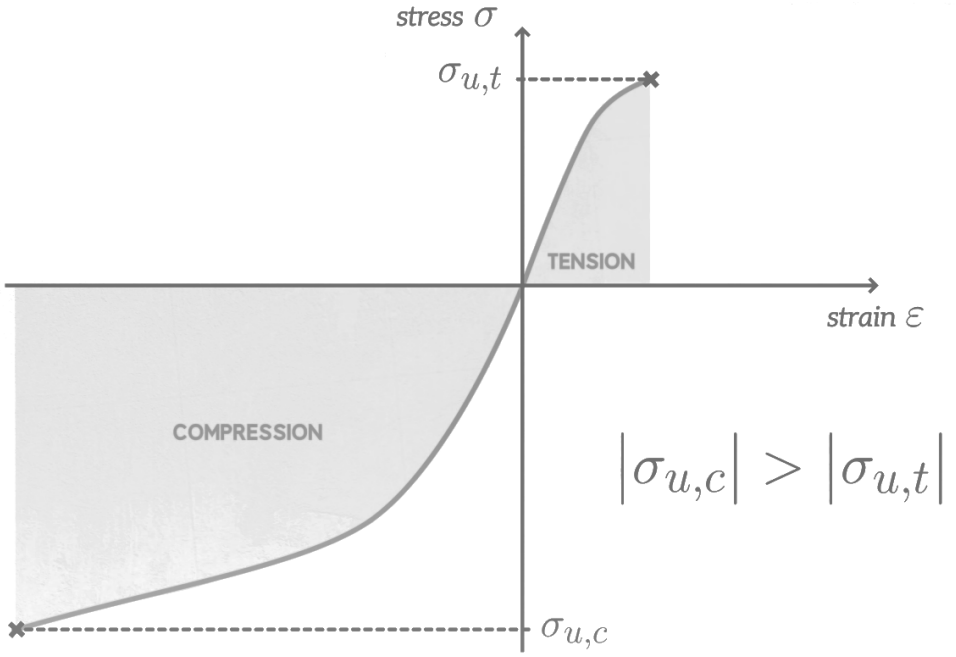


Figure 3.15: Stress and strain curve for brittle materials. From: [Schreurs, 2014].

It also means that to assess failure of brittle materials we need to know two separate ultimate strengths, for tension and for compression. Unlike the theories we have seen for ductile materials, it considers failure to be sensitive to hydrostatic stresses, and captures the difference between tensile and compressive ultimate strengths.

Coulomb-Mohr theory is a failure theory often used for brittle materials. Unlike the theories we have seen for ductile materials, it considers failure to be sensitive to hydrostatic stresses, and captures the difference between tensile and compressive ultimate strengths.

The Mohr theory outlines the initiation of yielding on a material plane, occurring when the combined shear stress and normal stress on that plane reach a critical level. This critical combination is expressed through the Mohr-Coulomb criterion, a fundamental representation of the simplest relationship between the shear stress (τ) and the normal stress (σ):

$$\tau = c - \mu\sigma \Leftrightarrow \text{yielding may start} \tag{3.53}$$

Here, the parameters c (cohesion) and μ (coefficient of internal friction) characterize the material's behavior. The coefficient of friction, μ, can also be described in terms of the friction angle ϕ:

$$\tan\phi = \mu \tag{3.54}$$

However, for materials exhibiting low tensile strength, it becomes crucial to set a limit on the maximum tensile stress, ensuring it does not exceed the material's tensile strength (f_u):

$$\sigma_{\max} \leq f_u \equiv \text{the tensile strength} \tag{3.55}$$

This condition is known as the tension cutoff condition, necessary to account for materials weaker in tension.

In a plane stress scenario where $\sigma_3 = 0$, the construction of the yield contour within the $\sigma_1\sigma_2$-plane follows a methodology akin to the process employed for the Von Mises criterion (Fig. 3.16).

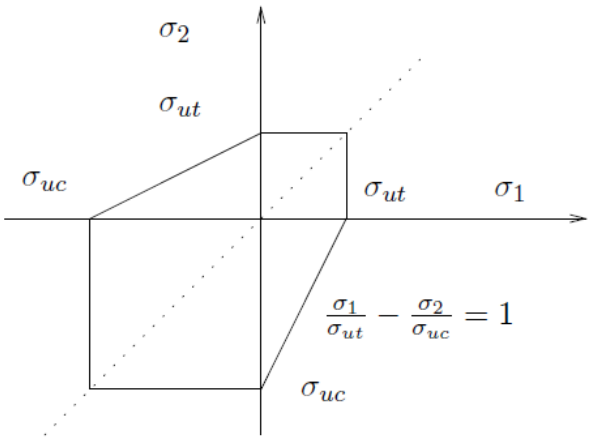


Figure 3.16: The yield curve within two-dimensional principal stress space adheres to the Mohr-Coulomb criterion. From: [Schreurs, 2014].

The yield surface in the three-dimensional principal stress space is a cone with axis along the hydrostatic axis (Fig. 3.17). The intersection with the plane $\sigma_3 = 0$ gives the yield contour for plane stress.

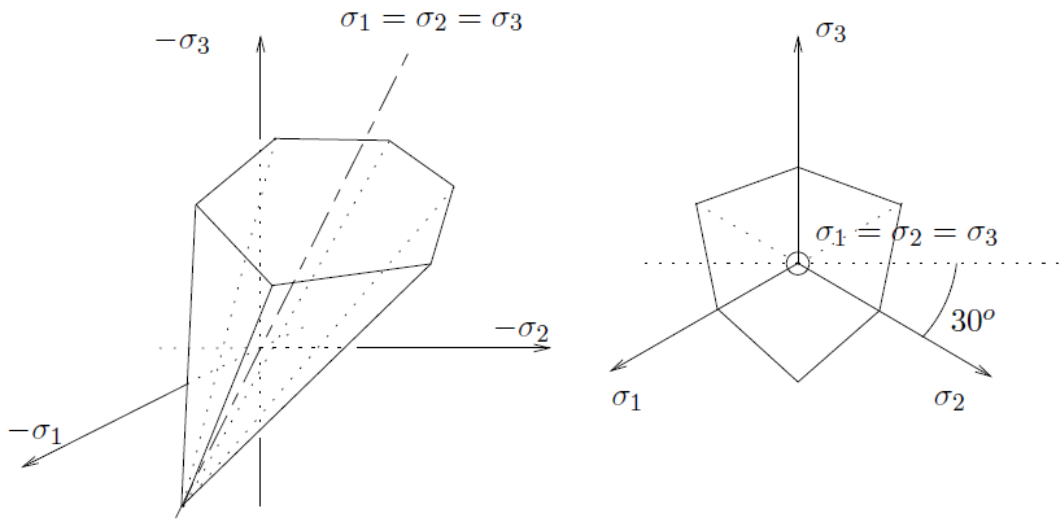


Figure 3.17: The three-dimensional principal stress space and the π-plane depict the Mohr-Coulomb yield surface.From: [Schreurs, 2014].

Drucker-Prager models

The Drucker-Prager yield criterion characterizes yielding in materials possessing internal friction and maximum adhesion. Similar to the relationship between the Von Mises criterion and the Tresca criterion, the Drucker-Prager criterion is related to the Mohr-Coulomb criterion.

In 1952, Drucker and Prager proposed an analogous extension of the Mises yield criterion, expressed through the Drucker-Prager yield criterion by the following condition:

$$\sigma_{oct} = \sqrt{\frac{2}{3}\tau_y - \mu\sigma_m} \Leftrightarrow \text{yielding may start} \tag{3.56}$$

The yield shear stress parameter, τ_y, represents the stress reached during yielding in pure shear conditions, denoted by μ as the friction coefficient and σ_m as the mean normal. This specific yield stress condition can be expressed as:

$$\sigma_{\max} = -\sigma_{\min} = tau_y, \sigma_m = 0 \tag{3.57}$$

In the $\sigma_1\sigma_2$-plane, the Drucker-Prager yield contour forms a displaced ellipse when considering a plane stress state where $\sigma_3 = 0$ (refer to Fig. 3.18).

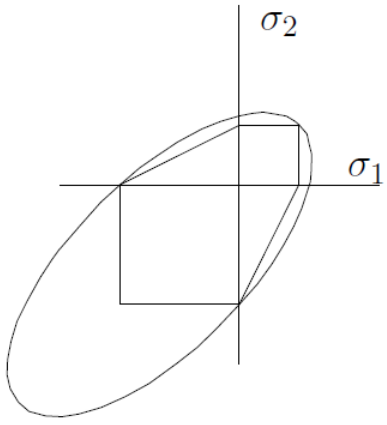


Figure 3.18: The two-dimensional principal stress space demonstrates the Drucker-Prager yield curve. From: [Schreurs, 2014].

The Drucker-Prager yield surface within three-dimensional principal stress space takes the form of a cone with a circular cross-section (refer to Fig. 3.19).

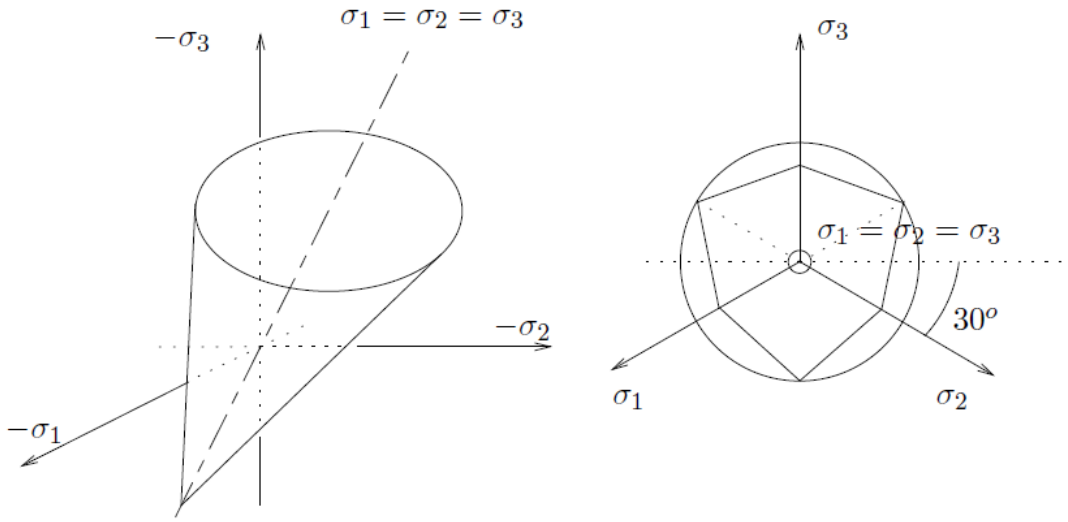


Figure 3.19: In the three-dimensional principal stress space and the π-plane, the Drucker-Prager yield surface. From: [Schreurs, 2014]

Collins strength model

An advanced approach to estimating the shear strength of geological materials has been developed by researchers such as Collins et al. [2004]. This model involves the utilization of pressure-dependent yield strength for intact rock and applies a Coulomb dry-friction law for fully fragmented materials. It incorporates a pressure-dependent yield strength for both undamaged and partly or fully damaged materials, diverging from the conventional treatment of damaged materials as a strengthless fluid. Instead, these materials are now characterized by pressure-dependent yield strengths and can even possess cohesion. This methodology is founded on the integration of a damage accumulation method, such as the Grady-Kipp model, as outlined primarily by Collins et al. [2004], and supported by related studies like Jutzi [2015] and Emsenhuber et al. [2018].

The Collins strength model defines the yield strength for intact material, providing a yield limit specifically for undamaged material. This yield limit, approximating experimental data from Lundborg (1968) and commonly representative of geological materials, is expressed as:

$$\tau_i = c - \frac{\mu_i p}{1 + \frac{\mu_i p}{(Y_M - c)}} \Leftrightarrow \text{yielding may start} \tag{3.58}$$

where, y_i signifies the pressure-dependent yield strength for intact rock, $p = I_1/3$ represents the hydrostatic pressure derived from I_1, the first invariant of the stress tensor. Additionally, c denotes the shear strength at zero pressure, known as cohesion, while Y_M stands for the von Mises plastic limit (representing the asymptotic yield strength for $p \to \infty$). Lastly, μ_i represents the coefficient of internal friction.

The combination with some models for damage accumulation (like Grady-Kipp) means that the model also accounts (at least implicitly) for strain-rate and size effects (via the underlying Weibull flaw distribution). The optional combination with some (constant) melt energy/temperature adds a rudimentary treatment of thermal effects. An additional dependence on some (constant) melt energy can be included via

$$\tau_i \to \tau_i \left(1 - \frac{e}{e_{\text{melt}}}\right) \tag{3.59}$$

or alternatively via the temperature [Collins et al., 2004].

This model was developed specially for simulations of mid-sized impact into a granitic terrestrial

crust. Using it the results show that the stresses and strains are lower in radial distances and increase near the impact site.

In Fig. 3.20, essential insights into the relationship between the strength of rock material and pressure are depicted. The plot illustrates that for fragmented rock materials, the shear strength showcases a linear relationship with the confining pressure, with the constant of proportionality termed as the coefficient of friction (illustrated by the dashed line in Fig. 3.20a).

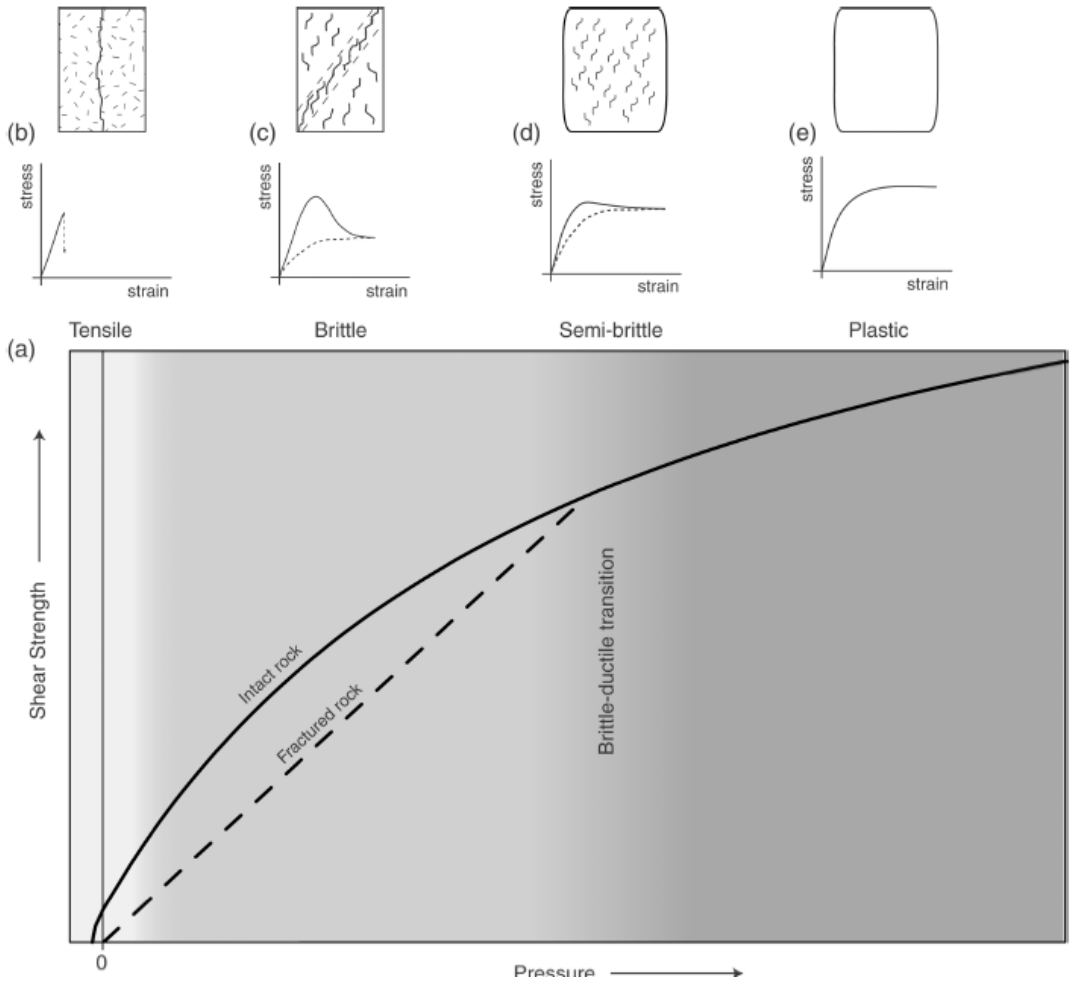


Figure 3.20: Panel (a) illustrates rock strength under pressure, depicting intact (solid line) and fractured (dashed line) rock behavior. Panels (b–e) show typical fracture patterns in lab-scale experiments, displaying stress-strain curves for intact (solid lines) and pre-fractured rock (dashed lines). From: [Collins et al., 2004].

Fish ice strength model

The precision of laws governing ice behavior and its failure criteria significantly impacts how is understand ice disruption. There are two distinct ways of describing how ice deforms and breaks under different stress conditions.

Tests (Fish [1991]) reveal that at lower stress levels or strain rates, ice strength seems unaffected by confining pressure. Ice demonstrates traits of an ideally cohesive material as its internal friction angle tends toward zero. Consequently, ice's yield criterion aligns with either the von Mises or Tresca rupture models.

Conversely, studies (Jones [1982]) from triaxial tests conducted at elevated stresses, strain rates, and/or confining pressures reveal nonlinear patterns in ice strength concerning confining pressure. These investigations indicate an angle of internal friction in ice, distinct from zero. Interestingly, at a specific confining pressure threshold, ice strength achieves its peak value (Jones [1982]), aligning with the pressure at which ice melts.

The ice's yield function can be defined using either the extended von Mises or Mohr-Coulomb rupture models. Assuming positive compressive stresses, the ice's strength under multiaxial stress conditions adheres to a parabolic yield criterion. This criterion is applicable when the applied strain rate matches the instantaneous strain rate and accounts for the ice's strength variation with hydrostatic pressure [Fish, 1991]:

$$\tau_{io}(p) = c + bp - \frac{b}{2\sigma_{max}}p^2 \tag{3.60}$$

or

$$\tau_i^* = (c + bp) - (c + bp^*)\left(\frac{p}{p*}\right)^2 \Leftrightarrow \text{yielding may start} \tag{3.61}$$

in the context of the ice's properties on the octahedral plane, the variables are defined as follows: c represents the ice cohesion, while b equals $\tan\phi$, with ϕ being the angle of internal friction. The equation $\sigma_{max} = p^2/2(\frac{c}{b} + p^)$ defines the magnitude of the hydrostatic pressure at which ice's shear strength attains its maximum. Here, p^* symbolizes the ice melting pressure, where the shear strength of ice becomes zero (refer to Fig. 3.21).

Laboratory tests have indicated that under triaxial compression, the ice's melting temperature

and, correspondingly, its strength decrease with an applied hydrostatic pressure. The mathematical model considers temperature-dependent parameters that significantly influence ice strength, primarily the ice melting pressure, cohesion, and friction angle. These parameters are presumed to exhibit proportionality with temperature.

The equation 3.61 represents an extended form of the Von Mises-Drucker-Prager yield criterion. Notably, for low-stress levels ($p << \sigma_{max}$), the third term within the equation tends toward zero, transforming it into the Drucker and Prager [1952] criterion, which is an extension of the Von Mises yield criterion.

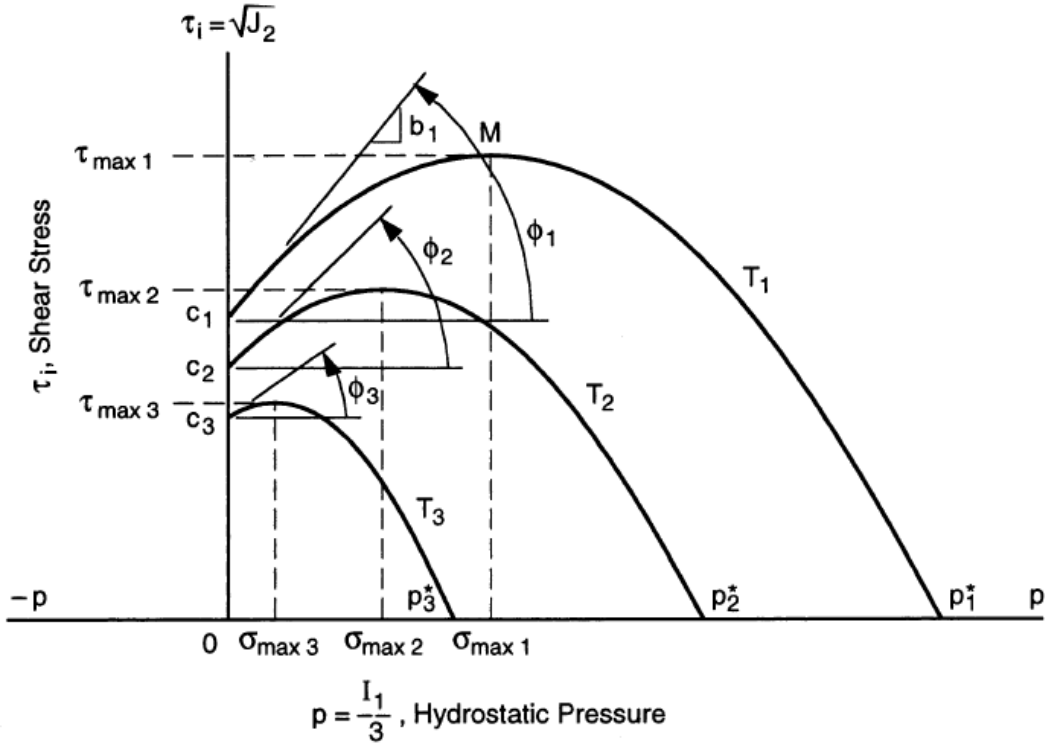


Figure 3.21: Strength envelopes of ice at various temperatures. From: [Fish and M., 1997].

Temperature effect

Test data showed that the ice parameter p^*, c, and b are functions of temperature. Consequently, the strength characteristics and the shear strength of ice are also functions of temperature.

For crystalline materials like ice, the melting temperature is influenced by the hydrostatic pressure. When the pressure (p) equals zero, the ice's melting temperature (T_m) stands at 273.1K. Additionally, for ice at a temperature of $\theta = 0°C$, the parameter A holds the value of:

$$A = 0.074 \text{ K/MPa} \tag{3.62}$$

At the critical hydrostatic pressure p^*, the shear resistance of ice becomes zero,

$$p^* = \frac{-\theta}{A} \tag{3.63}$$

Ice cohesion

Ice strength is inherently a stochastic outcome, arising from crack propagation and the rupture of intermolecular bonds. Upon freezing water at 0°C, a specific quantity of these bonds forms within each unit volume of ice. Further reduction in temperature results in additional bond formation due to the solidification of the liquid phase along grain boundaries. This process leads to a substantial increase in ice strength and, subsequently, its cohesion. Under a hydrostatic pressure of $p = 0$, ice strength is characterized by ice cohesion, which is temperature-dependent and comprises:

$$c(T) = c_0[1 + \alpha(1 - T)/T_m] \tag{3.64}$$

At moderate temperatures, this association deviates from linearity and is more accurately depicted by a nonlinear relationship

$$c(T) = c_0 e^{\alpha(1-T/T_m)^\mu} \tag{3.65}$$

or

$$c(\theta) = c_0 e^{\alpha|\theta|/T_m} \tag{3.66}$$

with $|\theta| = (T_m - T)$ is ice temperature (°C), when $\mu = 1$.

Angle of internal friction

The internal friction of ice $b(T)$ of ice can also be presented as:

θ°C	c (MPa)	b	Φ°	$\sigma_{\max}$ (MPa)	$\tau_{\max}$ (MPa)	p^* (MPa)
-40	12.93†	0.241	14	245.87	43.52	540.54
-16	9.43	0.125	7	80.15	14.44	216.22
-11.8	8.14	0.106	6	53.81	10.99	159.46
-11	7.91	0.103	6	49.0	10.43	148.65
-6	6.63	0.08	430	20.05	7.43	81.08
-1	5.56	0.053	3	4.79	5.69	36.85
0	5.37	0.04	2	-	-	-

* Data in this table for strain rate $\dot{\varepsilon} \approx 5 \times 10^{-3}$ s^{-1}

Table 3.1: Strength parameters of ice at various temperatures. From: [Fish and M., 1997]

$$b(T) = b_0 e^{\beta(1-T/T_m)^\nu} \tag{3.67}$$

or

$$b(\theta) = b_0 e^{\beta_1 |\theta|^\nu} \tag{3.68}$$

at the time of ice formation at 0°C, ϕ_0 represents the angle of internal friction of ice, and $b_0 = \tan\phi_0$. Here, $\beta_1 = \beta/T_m^\nu$ where $\nu = 1/2$, which aligns with the test data.

Parameter evaluation

The temperature-induced variations of ice strength in a multiaxial stress state are outlined by the temperature-dependent parameters $p(T)$, $c(T)$, and $b(T)$. This dependency is assessed for low hydrostatic pressures ($p << \sigma_{max}$), based on pressure tests from Gagnon and Gammon [1995] and Jones [1982], particularly focusing on Labrador iceberg ice:

$$c_0 = 5.37MPa; \qquad b_0 = 0.04; \tag{3.69}$$

$$\alpha = 9.61; \qquad \beta = 4.69. \tag{3.70}$$

The ice cohesion $c(\theta)$, friction parameter $b(\theta)$, and friction angle $\phi(\theta)$ were calculated using equations 3.68 and 3.66 from table 3.1, based on these parameters.

Chapter 4

Simulations to define the initial conditions.

4.1 Initial conditions

This chapter is focused on conducting simulations to establish initial parameters that are crucial for subsequent analyses. The primary objective of these simulations is to optimize numerical performance, minimize inherent errors, and facilitate a comparative study of methods that closely emulate physical conditions relevant to macroscopic bodies. However, some challenges arise due to the disparity between the scale of the bodies under examination and the substantial numerical errors encountered as a result of their non-gravitational conditions. The methodologies employed were originally devised for high-velocity scenarios and planet formation, necessitating adjustments to align with the characteristics of these smaller celestial entities. Addressing these discrepancies is essential to achieving accurate simulations and extracting meaningful insights from the results.

4.2 Initial particle arrangement

In SPH the solid body's representation involves discretization into mass units known as particles. These particles serve as the sampling points within the numerical framework and encapsulate essential physical attributes such as mass, momentum, and energy, representing distinct portions of the fluid. The initial state of each particle—comprising parameters like position, velocity, and other pertinent characteristics—constitutes the input for the SPH simulation program. Given that the simulation's

ultimate results hinge upon these initial conditions, meticulous consideration of these parameters becomes crucial to ensure the generation of substantive and accurate outcomes.

Selecting an appropriate initial spatial distribution for SPH particles is pivotal in reducing symmetry effects and minimizing particle noise. There are several methods proposed for this purpose, each having its benefits and limitations. The initial geometric arrangement of SPH particles can have a considerable impact on the outcomes of simulations. Various techniques have been used to set up initial conditions in multiple dimensions. This section provides a compilation of various particle setup methods, highlighting the challenges arising from the physical properties of the ice bodies relevant to this project. Additionally, we explore to identify the most suitable method that aligns with the nature of our problem to generate meaningful simulation outcomes.

The specifications for the geometric configuration used to create the initial SPH particle arrangements must agree with the following criteria:

- **Isotropy** The simulation domain's design should lack inherent directional biases across all locations.
- **Low particle noise** Uniformity within the setup is essential to reduce noise interference in density interpolation.
- **Resemble reality** To accurately model their internal structure (e.g. density, pressure and internal energy) before the start of the actual simulation run.
- **Versatility and ease to implement** The initial particle configuration algorithm must be easy to implement and generate quickly with minimal computing time.

The most common and straightforward method for simulating a specific volume with SPH is by using a regular lattice configuration. There are two significant possibilities, namely the *Cubic Lattice* or Simple Cubic (SC) lattice and either one of the two optimal packing schemes for equal spheres - the *Cubic Close Packing* (CCP) and *Hexagonally Close Packing* (HCP) lattice - that are important in this context and observed in the first row of figure 4.1.

Although the SC lattice is easy to set up, it has some significant drawbacks. Firstly, it doesn't represent a stable equilibrium distribution of particles. Secondly, it shows a strong anisotropy, meaning it has preferred directions (locally and globally), particularly along the three major axes.

Beyond the basic regular lattice formations illustrated in Figure 4.1, diverse alternative configurations exist. Notably, a subset of techniques enables the creation of spatially adaptable particle

distributions, including the Random Configuration, Stretched Lattice, Stretched Glass, and Concentric Shells methods. These approaches have primarily been utilized in generating spherically symmetric arrangements.

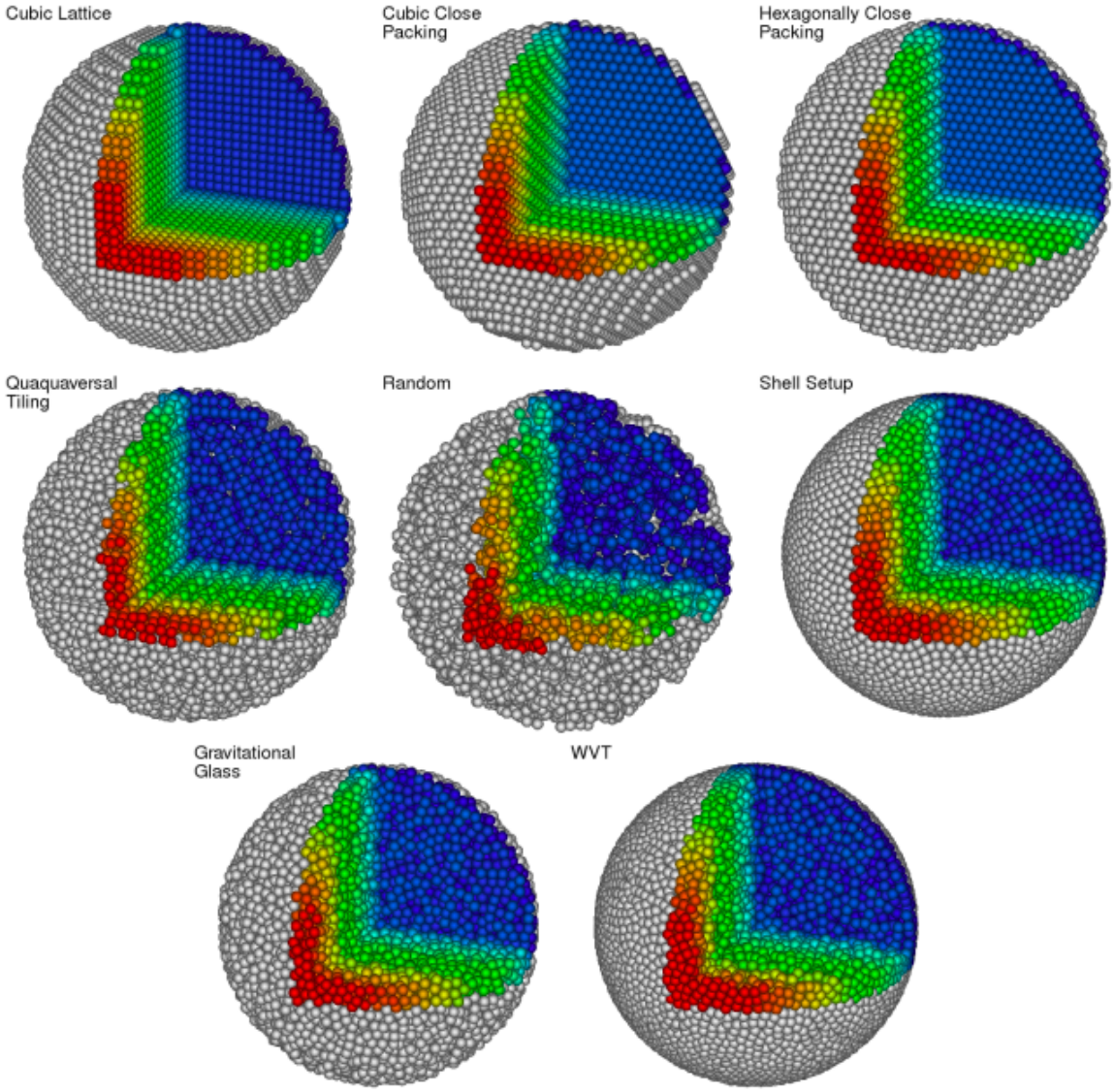


Figure 4.1: Popular configurations for setting up spatially uniform SPH initial conditions (Diehl et al. [2012]).

In order to determine the right arrangement of particles for our project, which involves studying the collision of small ice bodies, we considered a spherical target with a 20-meter-sized and a 5-meter-sized projectile with an impact velocity of 20 m/s. To model the materials, we used the constants

listed in table A.1 and the Tillotson equation of state with the material parameters presented at Benz and Asphaug [1995] and in SI values at table A.2. The damage model was implemented using Weibull parameters, and for water ice, we adopted the values specified in table A.3 in the publication by Lange et al. [1984].

We employed the simple cubic lattice arrangement to distribute the SPH particles. To achieve this, we arranged the particles in two parallel cubes and removed spheres from them. Although this is the most straightforward and quickest method to implement, it does have certain drawbacks.

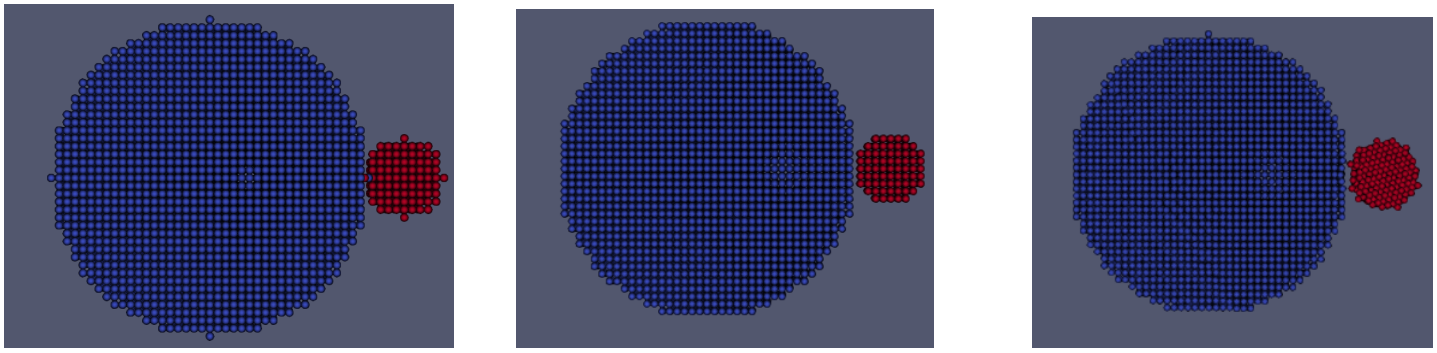
As present at Diehl et al. [2012], the cubic lattice distribution shows a non-equilibrium configuration when the particles are perturbed. While this might seem advantageous initially, it can lead to artificial grid-like structures in the simulation domain. In many natural scenarios, such as turbulent flows or multiphase systems, fluid behavior is highly non-uniform and exhibits intricate patterns that a regular lattice structure cannot replicate. The regular spacing between particles in a cubic lattice can impede the efficient exchange of momentum, energy, and mass between neighboring particles, leading to inaccuracies in the simulation of mixing processes.

The regular and symmetrical arrangements of the simple cubic lattice can cause numerical instabilities and insufficient mixing and interaction. These phenomena were studied by Burger [2015], who investigated the effects of symmetry in simulated environments. He discovered that collisions between bodies made using the SC lattice resulted in differences in the remaining debris disk around the central bodies. The strongly preferred directions of the SC lattice caused lines of dense material to form along the main symmetry axes, while other directions were much less populated.

Besides the well-known problems from SC lattice distribution of particles, it is simple to implement and for this reason, widely used. However, during our simulation, we discovered another systematic numerical error. This error occurred when we distributed the SPH particles to the last layer of the body shell. As a result, the outermost particles were left as only six particles located at the poles of the body. So when we performed a front collision between bodies using this arrangement, the face impact happened first between the outermost particles of each body, resulting in a perfectly elastic collision, which is not representative of this system.

In order to solve this issue, we removed the outermost particles from the bodies. This was done to prevent the bodies from bouncing during the first collision contact made between them due to particle-to-particle contact. The removal of these particles is illustrated in Figure 4.2a (before) and Figure 4.2b (after). On top of that, to avoid the symmetry problems we previously discussed and studied by Burger [2015], we implemented the rotation of the bodies (Figure 4.2c). We conducted numerous simulations to study the behavior of two bodies colliding. Both bodies and/or just the

target or the projectile were rotated at various angles around all axes to analyze the outcomes. After analysis, we found the best result was achieved when only one body was rotated in all axes by a different random angle. This rotation produced a collision distribution of particles without any preferential direction.



(a) Outermost particles generating problem

(b) Removing outermost particles from the poles.

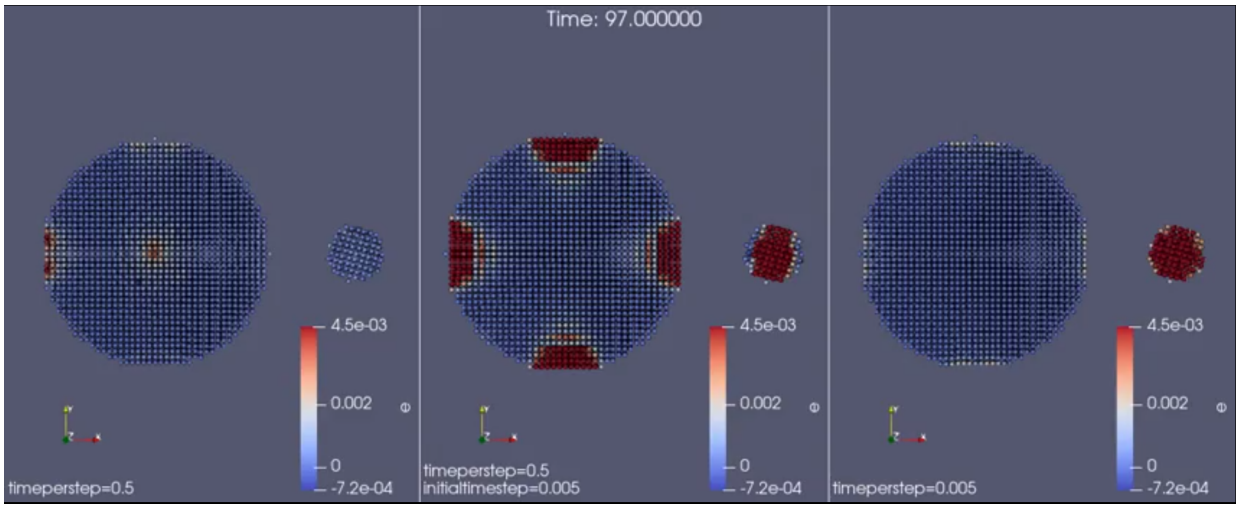
(c) Rotating projectile.

Figure 4.2: Different particle arrangements using the simplest cubic lattice. The left panel a) shows the bodies with a single particle on each surface border. Middle panel b) the outermost particles were removed from a) arrangement. The last right panel c) also has the outermost particles removed and the projectile was rotated.

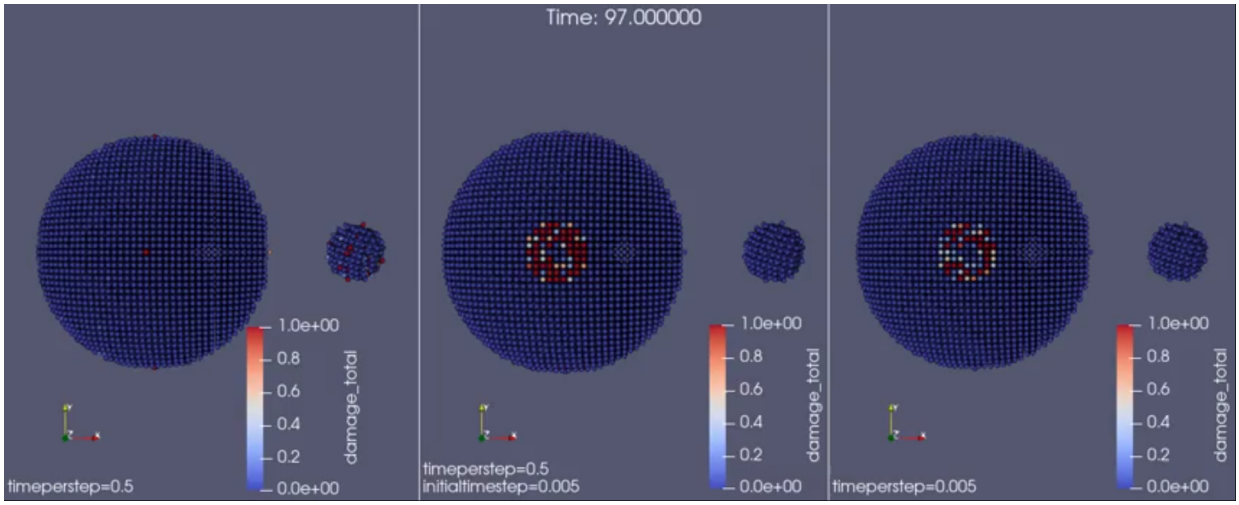
While using the SC lattice, we also encountered another issue when we incorporated self-gravity into our simulation. Self-gravity is important because we want to study the collision between bodies ranging from centimeters to meters in size and observe the resulting agglutination or fragments after the collision. However, when self-gravity is added to the simulation, it comes with a computational cost and increases the chances of numerical errors related to the tree used to build the self-gravity.

To study the effect of self-gravity in the simulation, we removed the target velocity from the same configuration used in the previous simulation (Fig. 4.2c)(c)). This left both bodies initially stationary. We expected that nothing would happen when these bodies were integrated. However, the simulation showed that the bodies eventually broke suddenly at the poles, as shown in Figure 4.3b)). After this event, the damage continued to grow slowly, and the internal energy kept increasing (Figure 4.3a)).

One plausible explanation for this issue could stem from the lack of gravitational equilibrium among the bodies, potentially leading to discrepancies in the system due to a divergence between the tree builder and the integrator. Consequently, this discrepancy might manifest as significant numerical errors.



(a) Simulation video



(b) Simulation video

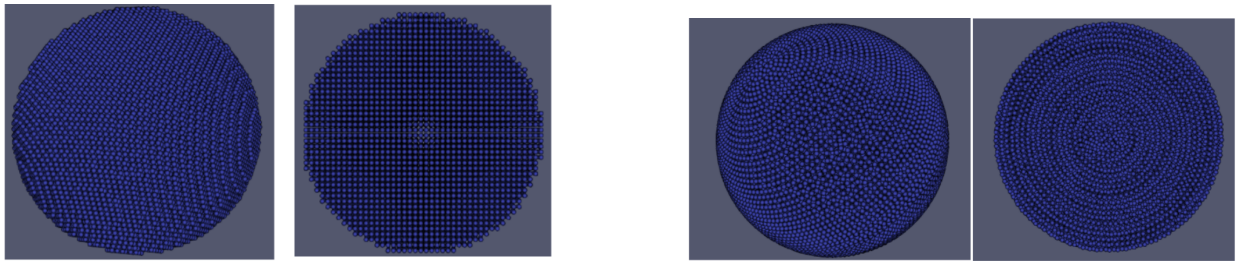
Figure 4.3: Snapshot from different simulations exampling when there is a numerical error. In upper panel (a) the body is sliced in half to show the variation of energy. Lower panel (b) shows the unexpected damaged particles on the poles of the bodies.

To mitigate computational load, the Barnes-Hut algorithm partitions particles into groups, reducing the number of force calculations. Its efficacy relies on the relationship between group size, particle distance, and point group proximity. The criterion for Barnes-Hut, denoted as θ, determines the ratio of these distances, typically set at a default value of 0.5. Smaller θ values signify a more precise approximation.

However, as θ decreases beyond a certain threshold, the quality of approximation diminishes,

yielding larger errors. Attempts were made to address this issue by adjusting this criterion. Despite experimenting with different values, particularly adopting $\theta = 0.3$, minimal improvements were observed in mitigating the problem.

The current method of particle distribution in SPH simulations involves using a cubic lattice. Although it is the simplest implementation, it poses some issues, especially when dealing with meter-sized objects, as numerical errors tend to escalate quickly. Therefore, to achieve the highest level of simulation accuracy possible, we aim to perform more precise simulations. So we decided to change the distribution of particles from the bodies using a more optimal initial condition. Then we ran the simulations using Concentric Shells from SEAGen[1] script generation of particle arrangement, in which the initial conditions are set using shell templates. This technique is advantageous because places the particles randomly to not have preferred directions.



(a) Cubic lattice

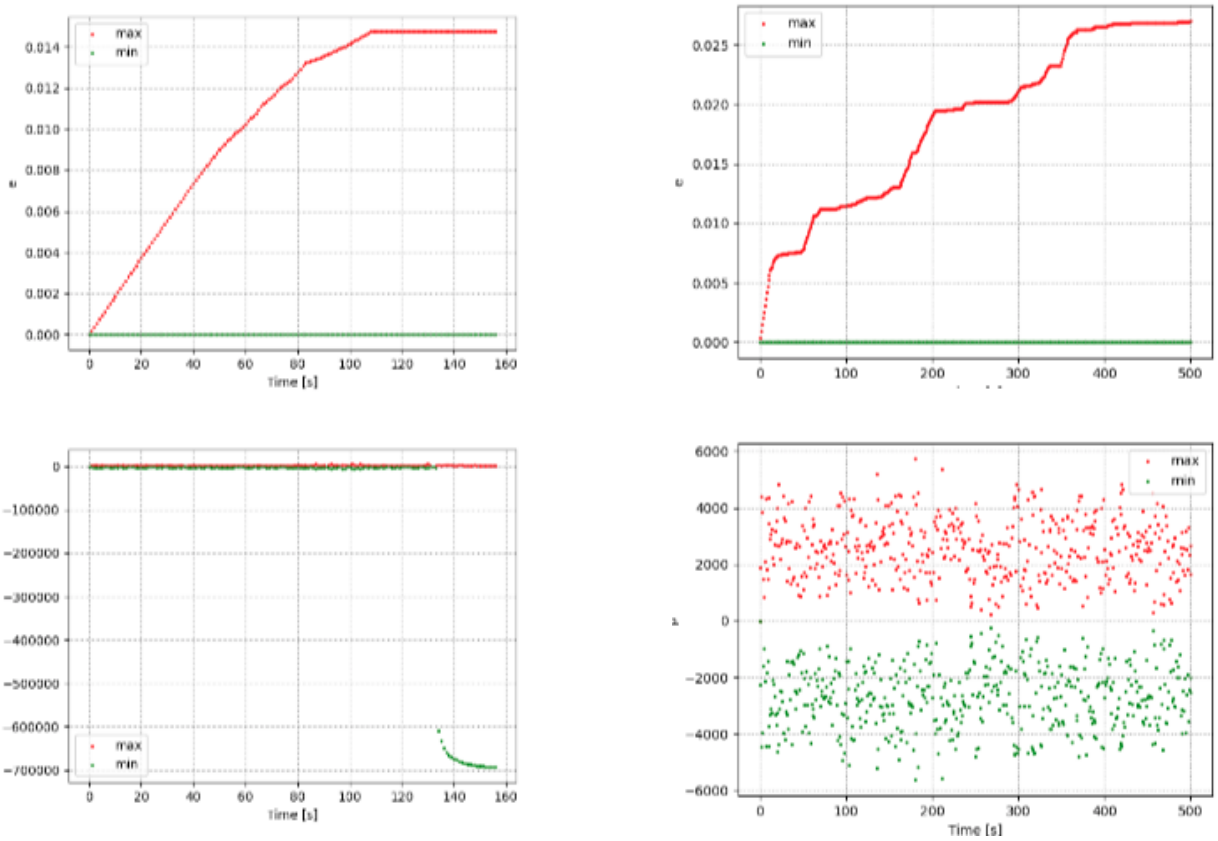
(b) Concentric Shells

Figure 4.4: Difference between the initial distribution of particles using two methods.

Using SEAGen distribution the early damage problem was solved. However, there persists a slight energy growth and pressure variance, but it is much less than using cubic distribution. Figure 4.5 shows the minimum (green) and maximum (red) variation of energy and pressure, considering SC lattice and SEAGen. The graphics show the variations until the energy gets stabilized, for the cubic lattice (Figure 4.5(a)) the energy stabilizes after unexpected damage happens after a huge pressure variation happens around 140s (seen at the lower panel of fig. 4.5(a)). On the other hand, using the SEAGen concentric shells (Figure 4.5(b)) the energy stabilizes without any damage happening and the variation of pressure keeps almost constant.

The last important parameter in the context of particle geometry is the mass. When performing similar investigations on significantly larger and more massive colliding bodies the differences between the initial configurations are much less discernible, probably because self-gravity is too strong. This means that there are still expected considerable issues but they are not as easily visible anymore

[1] https://github.com/jkeger/seagen



(a) Cubic lattice

(b) Concentric Shells

Figure 4.5: Difference simulations using the cubic lattice and concentric shells arrangement. Upper panels are the variation of pressure and lower panels are the energy variation over running time. The last time for each arrangement is when the energy stabilizes.

when going for more massive bodies. The conclusion is that self-gravity in a small masses scenario has the right magnitude to enhance the strong symmetry effects of the cubic lattice sufficiently. Finally, investigating geometrical particle structure does not just represent some pathological set of parameters leading to these clear symmetry effects, but actually this choice of parameters makes them clearly visible and easy to investigate, while they are, to some extent, present in most other scenarios, including non-spherical particle distributions.

4.3 Different number of neighbors

After reviewing the concepts outlined in sections 3.1 and 3.3, it becomes clear that SPH hinges on accurately estimating density. This estimation is dependent on both the masses m_i and positions x_i of the individual particles (eq. 3.1), as well as the kernel functions used.

In this section we aimed to investigate the efficacy of the B-spline kernel in estimating and preserving the body's density equilibrium without substantial internal energy increments, a significant challenge encountered in addressing early damage problems. To decrease the energy variation, we explored different numbers of neighbors for assessing accuracy, conducting convergence studies, optimizing performance, analyzing stability, and enhancing the generalization of simulation techniques. This systematic exploration helps to make informed decisions regarding simulation parameters and ensures the reliability and effectiveness of SPH simulations in various scenarios.

It's important to explore different numbers of neighbors in SPH simulations for a few reasons. First, having more or fewer neighbors can affect how accurate a simulation is. We can see how it affects the results by trying different neighbor numbers systematically. This helps us understand the balance between being accurate and using less computer power. Also, studying how changing the number of neighbors affects the results helps us figure out the minimum number needed for accurate and steady results. Finally, the number of neighbors can impact how stable the simulation is. If we don't have enough neighbors, it can cause problems like particles clumping together or spreading apart in strange ways. By looking at different neighbor numbers, we can see what range keeps the simulation stable and gives reliable results.

To understand the differences in the number of neighbors, we used the same setup as the target before with a stationary spherical body measuring 20 meters in diameter, along with the constants listed in tables A.1, A.2, and A.3, which were generated using SEAGen. Figure 4.6 shows the results of the simulation using different numbers of neighbors (N_h). We examined two aspects while integrating the body: firstly, whether it would eventually break or sustain damage, and secondly, the variation in

energy. Ideally, since the body is stationary, we would not expect any damage or increase in energy. However, it's normal to see a slight energy increase at the start of the simulation until it stabilizes. It becomes problematic only if the energy continues to increase indefinitely.

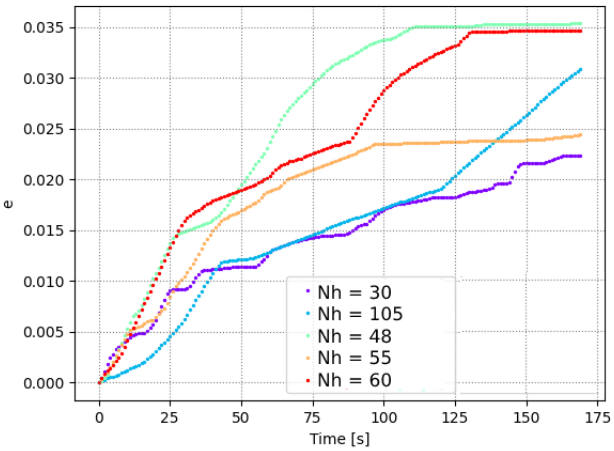


Figure 4.6: Growth of energy considering different numbers of neighbors.

On the figure 4.6 the plot shows the energy variations until its stabilization. Although this graph may suggest that employing 30 neighbors provided the optimal fit, since it had the lowest growth, it resulted in underestimated density and premature damage to the body (fig. 4.7). Conversely, utilizing 55 neighbors emerged as the optimal solution, it had the lowest increment of energy until became stabilized, and also did not break or show any damage. This result aligns with findings reported in Monaghan and Lattanzio [1985].

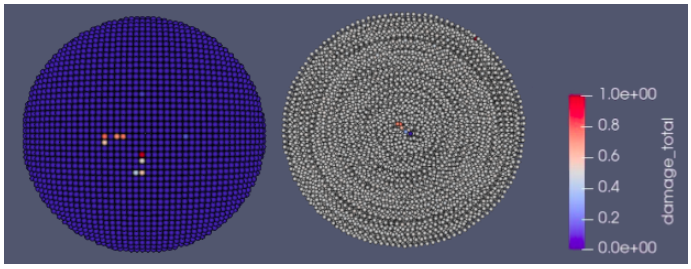


Figure 4.7: View of the shell (right) and the half of the sphere (left), using $N_h = 33$ when the body broke and got damaged.

When examining the issue of density underestimated, like the case of 30 N_h, or even the overestimation, it is imperative to delve into its underlying causes. The arrangement of particles plays a

critical role in this context. In scenarios where particles are positioned randomly rather than following a semi-regular distribution pattern, the calculated density for vacant positions remains unbiased. However, when a position is occupied by a particle with neighbors nearby, the self-contribution term, denoted as $m_i W(0, h_i)$, significantly inflates the density estimate, leading to overestimation.

Despite implementing the SEAGen particle distribution method, which aims to mitigate random placement, a residual bias persists particularly under conditions characterized by a low number of neighboring particles (N_H). This bias manifests as systematic overestimations across all kernel functions utilized in such scenarios.

Studying the number of neighboring, resolution, and arrangement of particles in SPH simulations is important for achieving convergence, ensuring that SPH simulations produce stable and accurate results. The number of neighboring particles directly influences the accuracy of the simulation, with an optimal number needed to capture underlying physics without introducing numerical artifacts. The particle arrangement impacts the simulation's accuracy and stability by affecting interpolation and smoothing kernels. By optimizing these parameters it is possible to enhance the reliability and applicability of SPH simulations.

4.4 Plasticity models

In section 3.4.5, we discussed how strength models define the deformation and failure of a material. Therefore, it is important to study how different plasticity models could affect the collision results. When a material is subjected to stress, it responds elastically until a certain point beyond which plastic deformation or failure occurs. This point is called the yield limit, and it marks the transition from elastic to elastic-plastic behavior. At MILUPHCUDA, different models are available to describe this limit and the point of failure, as shown in figure 4.8. In this section, we will summarize the available yield functions and compare collision results using different models. We aim to understand how these models influence macroscopic ice bodies relevant to our project.

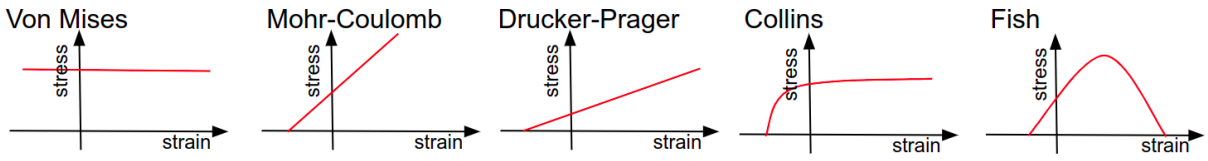


Figure 4.8: Sketch of Stress-Strain Diagram for different plasticity models implemented at MILUPHCUDA.

- **Von Mises**
  $Y = Y_0^2/3$
  Yielding becomes evident when the elastic energy linked to specific shape alterations exceeds a critical threshold.

- **Mohr-Coulomb**
  $Y = c_0 + \mu_i P$
  Yielding is described by the shear strength of materials by considering both cohesive forces and frictional resistance along a failure envelope in stress space.

- **Drucker-Prager**
  $Y = A + B(-I_1/3)$
  For materials characterized by internal friction and maximum adhesion, the Drucker-Prager yield criterion describes yielding, correlating with the Mohr-Coulomb criterion.

- **Collins pressure dependent yield strength**
  $Y = (1 - D)Y_i + DY_d$,
  $Y_i = Y_0 + \frac{\mu_i P}{1+\mu_i p/(Y_M - Y_0)}$; $\quad Y_d = \mu_d P$
  At significantly high confining pressures, the shear strength stabilizes at a constant value commonly known as the von Mises plastic limit.

- **Fish**
  $Y = (c_0 + \mu_i P) - (c_0 + \mu_i P^*) \left(\frac{P}{P^*}\right)^2$
  Extended Drucker-Prager yield criterion, the yielding is temperature dependent and follows a parabolic curve.

In order to understand how the yield function can change the output from a collision involving small ice bodies, we simulated the impact of a 5-meter-sized projectile on a 20-meter-sized spherical target at 20 m/s. To model the materials, we used the Tillotson equation of state presented at Benz and Asphaug [1995] and in SI values at table A.2. The Weibull parameters were used to implement the damage model, and for water ice, the values from table A.3. The material constants are present in figure 4.9, we used the shear modulus from A.1, but the yields stress and melting energy it was calculated from Fish and M. [1997] for a body at a temperature of $-17.5°C$.

Figure 4.9 shows the varied strength envelopes of ice are presented. At lower stress and strains, ice exhibits independence from confining pressure, essentially behaving as a material with virtually

zero angle of internal friction, akin to an ideally cohesive substance. Models such as von Mises or the Tresca rupture can be applied to describe its yield criterion during these conditions.

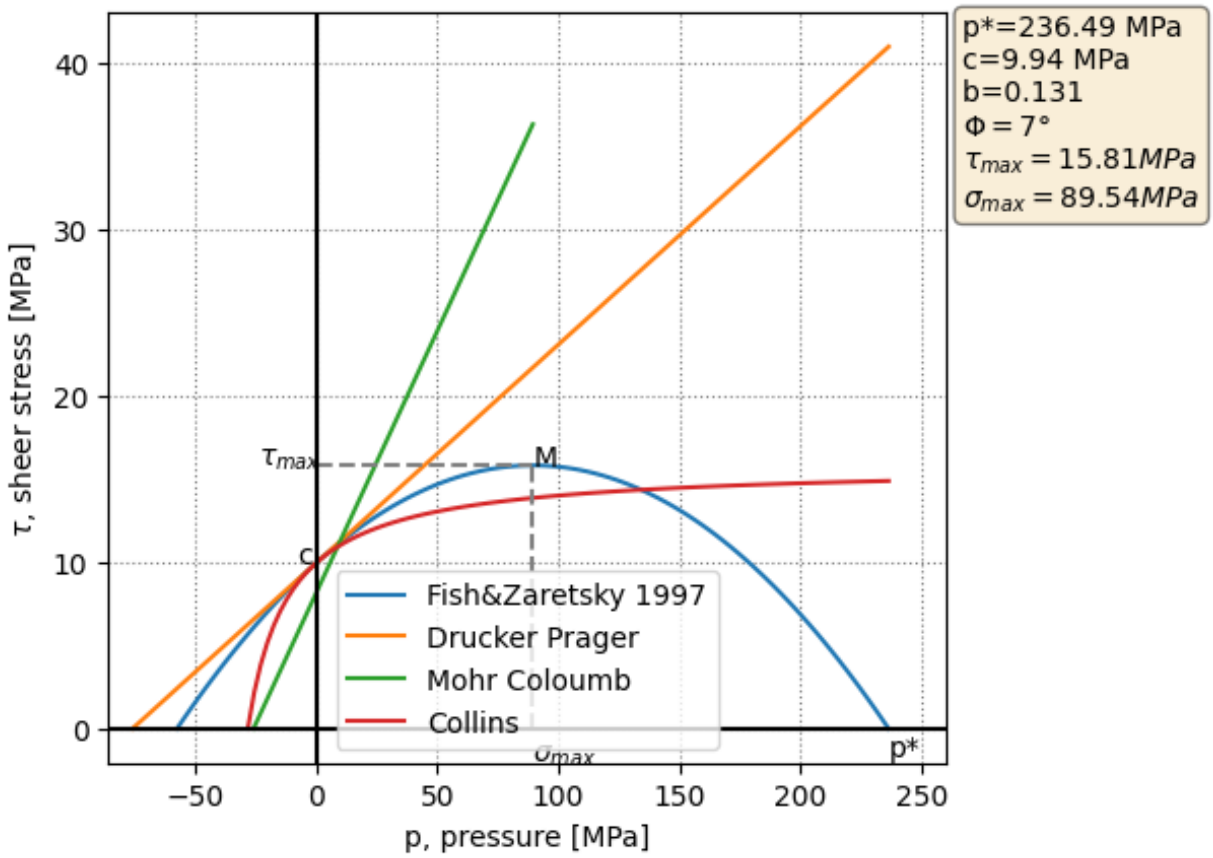


Figure 4.9: Comparing the stress-strain for different plasticity models for a body at a temperature of $-17.5°C$. Where $p*$ is the melting pressure, c is the cohesion, Φ is the friction angle, $\tau_{\max}$ is hydrostatic pressure at which the shear strength of ice reaches a maximum value, $\sigma_{\max}$ is the maximum shear stress and M is the maximum value from the parable of Fish model.

The results shown in Figure 4.10 are from an SPH simulation. The top left panel shows the outcome when the Fish and M. [1997] plasticity model was used. In this case, the projectile broke entirely, and the target's face impact broke into fragments and generated dust. When the Drucker Prager model was used, the target had a similar result, but the broken face impact was larger. In contrast, the Mohr-Coulomb model caused the target to break into two pieces. This can be attributed to the fact that this model allows higher pressures than Fish's model and Drucker Prager, as can be seen in Figure 4.9. The Collins model, unlike the other models, caused the target to deform more before starting to break.

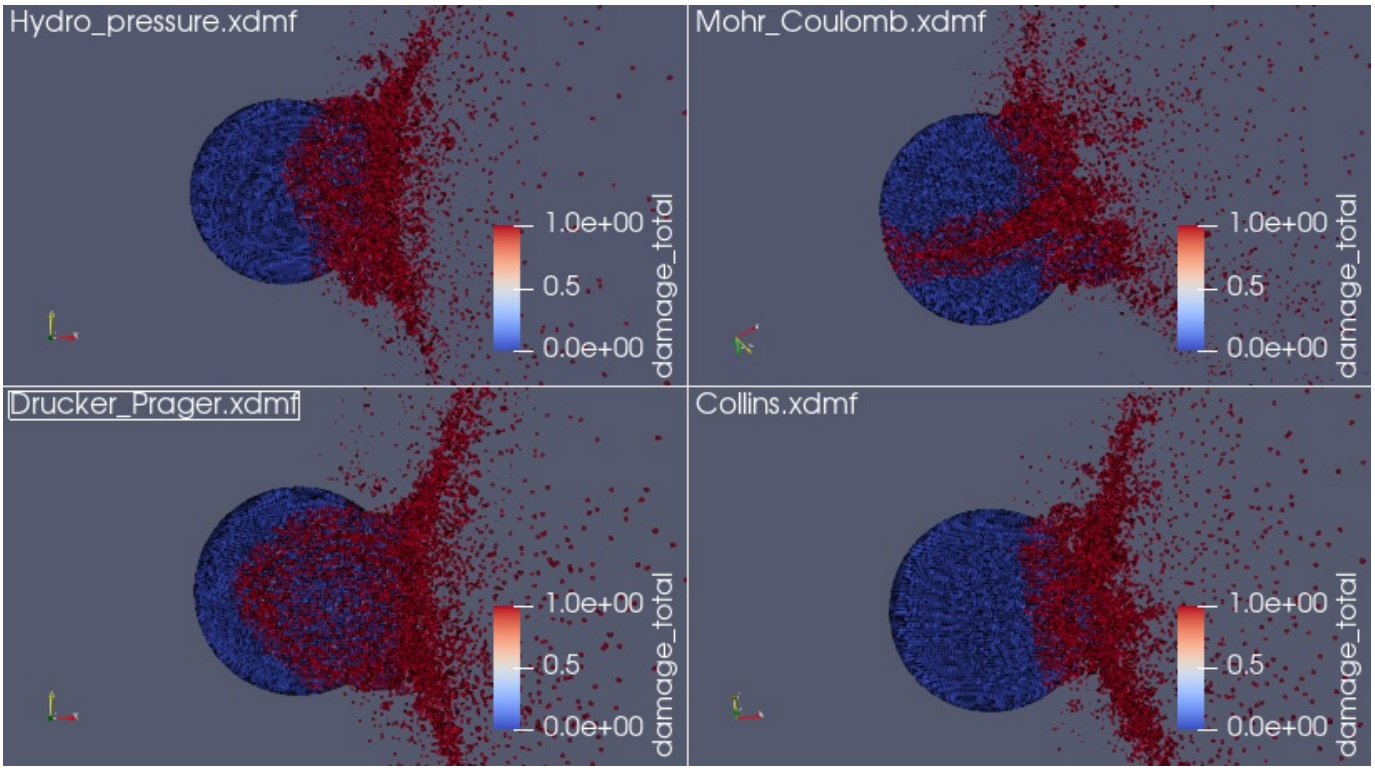


Figure 4.10: Simulations with a 20m radius target and 5m radius projectile, 20m/s velocity of impact and strength parameters calculated for ice body at -16°C temperature.

However, under conditions involving heightened stresses, strain rates, and confining pressures in triaxial tests, the relationship between ice strength and confining pressure becomes nonlinear. These tests unveiled that the angle of internal friction in ice deviates from zero. Notably, there exists a specific threshold of confining pressure wherein the strength of ice peaks, correlating with the pressure at which ice melts (blue curve from fig. 4.9).

Among the studied models, only the one proposed by Fish and M. [1997] intricately captures the behavior of ice while accounting for temperature variations. Given its alignment with the nuanced behavior of ice, this model stands as a more suitable choice for simulating ice bodies in our study.

4.5 Comparison with laboratory experiments

In the comparison between catastrophic disruption (Q^*) results obtained in laboratory experiments by Leliwa-Kopystyński et al. and simulations conducted using the hydrocode approach as presented by Benz and Asphaug, employing the Von Mises yield criterion, an overall overestimation of Q^* was

observed within the model proposed by Benz and Asphaug. This section delves into an analysis of the influence of different placidity models on these outcomes. Furthermore, a more appropriate model proposed by Fish and M., specifically designed for ice bodies, is applied to enhance the accuracy of the results. If the conclusions drawn by Benz and Asphaug are indeed accurate, then it is necessary to reevaluate the vulnerability of the weakest ice bodies in the Solar System. This is particularly important for those that fall within the radius range of 100-200 meters and are subjected to impact velocities ranging from 0.5 to 3 km s^{-1}.

Leliwa-Kopystyński et al. [2008] conducted an extensive investigation into the impact craters found on small celestial bodies, particularly emphasizing the disruption caused by impacts. This examination of catastrophic disruption represents the outermost boundary of cratering studies. Recent advancements in experimental analysis of impact cratering primarily focus on rocky celestial bodies. These studies aim to draw parallels between observed data and laboratory outcomes, particularly in simulating high-velocity impact disruptions on icy targets.

The challenge arises when attempting to apply laboratory findings from targets of decimetre-scale to larger bodies in the Solar System. Such a task demands intricate modeling and scaling adaptations. Several models have been proposed to address the challenge, but their success is dependent on specific criteria:

- Establishing a fitting scaling law to bridge the scale gap effectively.
- Incorporating the gravitational characteristics of the target body within the model.
- Providing reasonable estimations for a set of crucial material parameters.

The way small and large objects collide is different because of the forces that govern them. When smaller objects collide, their strength characteristics are the primary factor that determines the outcome. For instance, when observing laboratory-scale collisions, it is possible to see that the target material's strength plays a significant role in how the collision occurs. This is known as the strength regime. However, when larger objects collide, their gravitational forces are the most significant factor determining what happens. This is known as the gravity regime. It is essential to note that the distinction between these two regimes often overlooks the possibility of small objects being composed of rubble piles. Also, laboratory experiments do not account for porosity, which means they assume that objects are pristine, homogeneous, and rigid.

In exploring the dynamics of those regimes, figure 4.11 presents outcomes obtained from simulations conducted by Benz and Asphaug [1999]. Figure 4.11 showcases a comparative analysis between

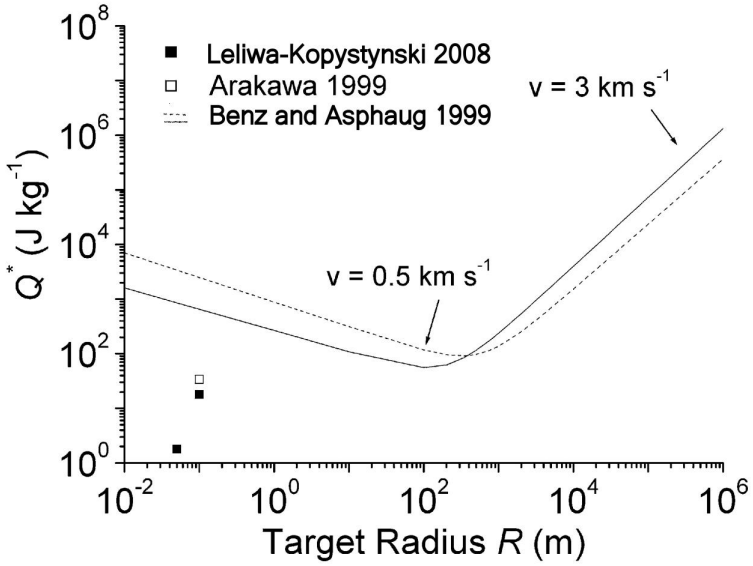


Figure 4.11: Comparison of Q^* for icy bodies in the laboratory Leliwa-Kopystyński et al. [2008] with the hydrocode model Benz and Asphaug [1999].

the critical energy density for disruption (Q^*) and the corresponding target radius (R). For a more detailed examination of collision scenarios involving ice bodies, specific values of Q* have been provided in Table 2 for collisions featuring a 10 cm target at an impact speed of 500 m/s.

	Target radius [cm]	**Projectile radius [cm]**	**Impact speeds [km/s]**	**Catastrophic Disruption Q^* [J/kg]**
Leliwa-Kopystynski 2008	10	0.247712	0.5	1.9
Benz and Asphaug 1999	10	0.247712	0.5	2.4837×10^3

Table 4.1: Case of 10 cm target for 500 m/s impact speed.

The laboratory-derived values of Q^* consistently exhibit significantly lower magnitudes compared to the predictions outlined by Benz and Asphaug [1999]. Benz and Asphaug projected Q^* values around 400 J kg^{-1} for impacts on ice spheres with a diameter of 10 cm. However, empirical data from laboratory experiments at these scales has yielded values notably below this predicted threshold. This discrepancy underscores the imperative for additional modeling efforts, as highlighted by the observations in the work of Leliwa-Kopystyński et al. [2008].

Here we considered simulation with the same parameters from Benz and Asphaug (table A.1, A.2 and A.3). For the case of a 10 cm target and 500 m/s speed velocity, we were able the reproduce their

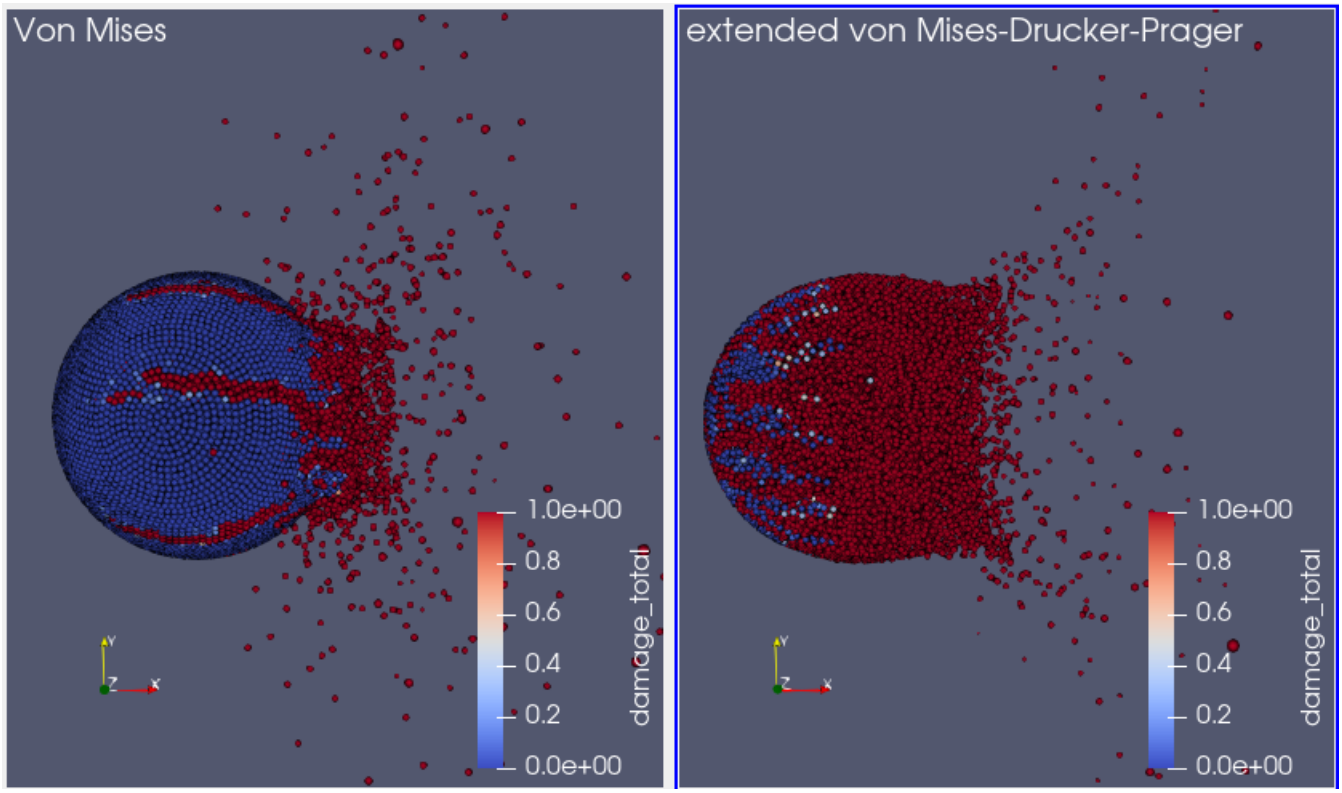


Figure 4.12: Simulation comparing the simulations of Benz and Asphaug [1999] and the laboratory from Leliwa-Kopystyński et al. [2008]

results using MILUPHCUDA (left panel of figure 4.12). We found that the percentage of the mass of the largest fragment using Von Mises is **46.28%**. However, when it is changed the plasticity model for the extended Von Mises-Drucker-Prager (Fish and M. [1997]), the percentage of the mass of the largest fragment became **9.23 %** (right panel of figure 4.12). Indicating that the Q^* should be times lower than predicted by Benz and Asphaug

Benz and Asphaug highlighted the ongoing necessity for comprehensive investigations to refine material properties governing the behavior of icy bodies subjected to high strain rates. A concerted focus on advancing plasticity models and meticulously adjusting parameters like friction angle and cohesion enhances the simulations' predictive capability significantly. Aligning these parameters with empirical laboratory data holds the promise of establishing a more accurate framework for comprehending the intricate response of icy bodies under diverse environmental conditions.

Chapter 5

General rings and arcs simulations

5.1 Simulation Comparison with Analytical Collision Models

This section presents the outcomes derived from SPH simulations exploring collisions between bodies with a density of 0.9 g/cm^3 and porous objects with 0.5 g/cm^3. We aim to analyze the dust production and the possibility of agglutination of the bodies' post-impact. In addition, compare our results with Leinhardt and Stewart [2011] predicts of collisional output, then check the validity of the model for such small bodies.

The study of collisions between bodies within planetary rings often involves N-body simulations coupled with analytical methods to predict collision outcomes. However, the computational demands rise significantly with the number of bodies, leading to a trade-off between accuracy and simulation time. Typically, collisions are simplified as perfectly inelastic to speed up computations, yet this over-simplification ignores the production of debris and fragments post-collision. Consequently, it tends to overestimate collision efficiency, impacting the estimation of formation times and the resultant body masses.

Another factor that can impact the running time of the simulations is the integration of fragments into simulations, it plays a pivotal role in planetary formation and dynamic studies, however, it remains a complex challenge. The sheer volume of fragments resulting from collisions makes direct integration via N-body simulations impractical. To address this, researchers have explored different strategies. Some opt to include only a select few impact-generated bodies (Chambers [2013], Clement et al. [2019]). Alternatively, others have employed collision catalogs to categorize collision types and

post-impact fragments (e.g., Leinhardt and Stewart [2011]). These approaches aim to bypass the computational hurdles posed by incorporating numerous fragments into simulations, allowing for a more feasible exploration of collision dynamics.

The paper Leinhardt and Stewart [2011] identifies several distinct "outcome regimes" based on the relative masses and velocities of the colliding bodies. These regimes include accretion, erosion, hit-and-run, merging, and disruptive collisions. They develop scaling laws for gravity-dominated bodies to predict the outcomes of these collisions based on parameters such as impact velocity, mass ratio, and impact angle. However, this model may not be suitable for collisions involving strength-dominated bodies.

The model's limitations for strength-dominated bodies arise because it does not adequately account for the effects of material strength, such as fragmentation, deformation, and structural integrity, which can play crucial roles in determining collision outcomes. In strength-dominated collisions, factors like internal cohesion, fracture mechanics, and material properties become important, which are not explicitly addressed in the gravity-dominated model.

To accurately model collisions involving strength-dominated bodies, a more comprehensive approach that incorporates material strength and fracture mechanics would be necessary. This might involve numerical simulations or experimental studies that take into account the specific properties of the materials involved and how they respond to impact forces. To delve into these physical properties, we utilized SPH, a method more adept at modeling such intricacies. This methodology enables a more nuanced representation of body properties, allowing adjustments in resolution concerning variables like density, thereby facilitating exploration across diverse material responses within pressure and temperature regimes.

Supposing a common collision between macroscopic bodies, we simulated a collision between two same-size bodies. Figure 5.1 illustrates the geometry of N-body and SPH simulations. The target (red) is hit by the projectile (blue) with velocity V_i. θ is the angle of impact, defined at the first contact between the bodies and comprised between the line joining the center of each body and the ray that passes through the velocity projectile impact. R and r are the target and projectile radii, respectively. The impact parameter is given by $b = \sin\theta = B/(R+r)$. The length l is the projectile's overlap with the target.

Also at SPH, the bodies are placed at a mutual distance of $r_{ini} = R + r + 2.5_{\mathrm{sml}}$. It is added to the distance this 2.5_{sml}, where *sml* means the smoothing length, which is the space used to determine the region of influence of the neighboring particles. So the bodies can be distinguished at the start of the simulation.

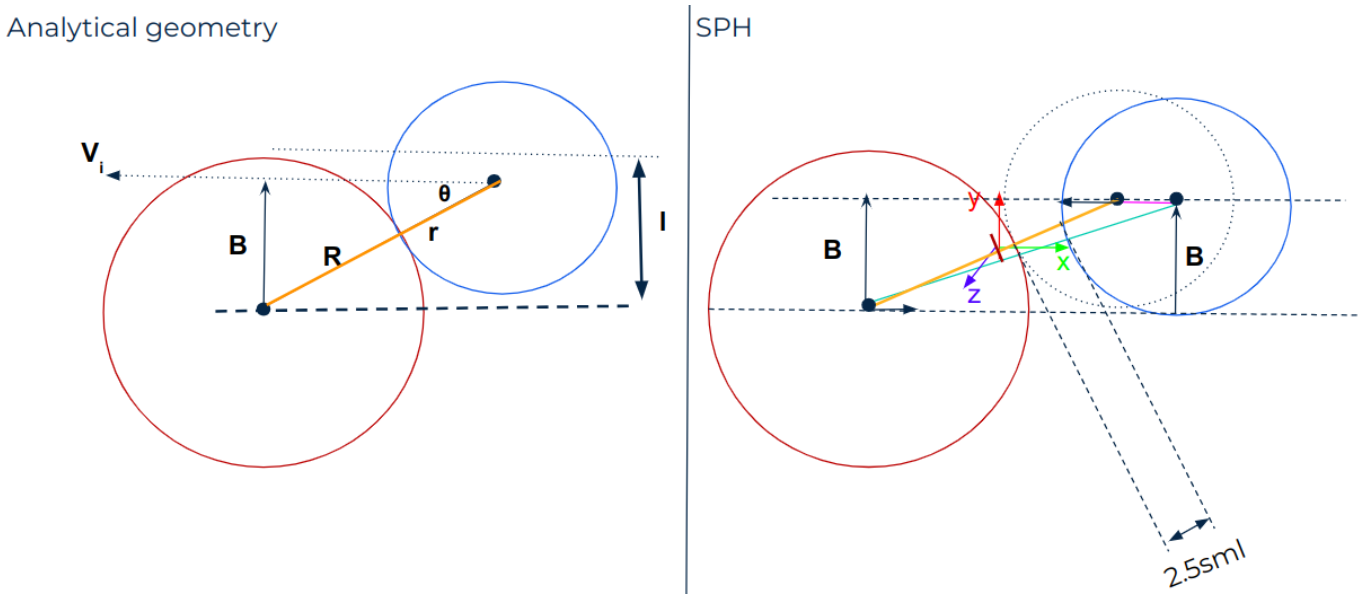


Figure 5.1: Representation of the geometry of a collision.

The projectile and target are both modeled as solid ice bodies. The Tillotson equation of state was used as the input parameters ice Schäfer et al. [2016] to determine the pressure (table A.2). It also included the material strength where the Fish model limits the shear strength Fish and M. [1997]. To model tensile fractures, it follows Benz and Asphaug [1994] (table A.3) and the Grady-Kipp fragmentation model and the standard artificial viscosity by Monaghan and Lattanzio [1985]. The Barnes-Hut tree was used to calculate the gravitational forces between the particles.

The post-collision analysis is needed for the identification of fragments, including their dynamics and composition, and the study of dust production is made of two main steps. Initially, a friends-of-friends algorithm identifies all spatially directly connected clumps of SPH particles, considering them as "fragments". This process takes place before the identification of gravitationally bound "aggregates" of those fragments, which is part of the second step. Starting from a seed aggregate consisting of the most massive fragment and all those mutually gravitationally bound to it, an iterative algorithm adds or removes fragments from this seed aggregate (its centroid) until convergence. After identification of the largest aggregate, the process is repeated to find the second-largest one, starting from the most massive fragment not yet incorporated into the largest aggregate [Burger et al., 2017]

All SPH simulations use 150 000 particles for each body, target and projectile. This ensures a reasonable resolution even for scenarios involving similar-sized collisions. The runtime depends mainly on particle number and impact velocity (which determines the overall simulated time), where

a single SPH simulation presented here, including all pre-and post-processing, takes on the order of one to three weeks to complete.

In the simulations with a density of 0.9 g/cm^3 was captured in Figure 5.2. Both spherical bodies in the simulations had a radius of 20 meters and an impact velocity of 19.518 m/s at an impact angle of 62.81°. The figures show that the target body is colored red while the projectile is colored blue, making it easy to differentiate between the two.

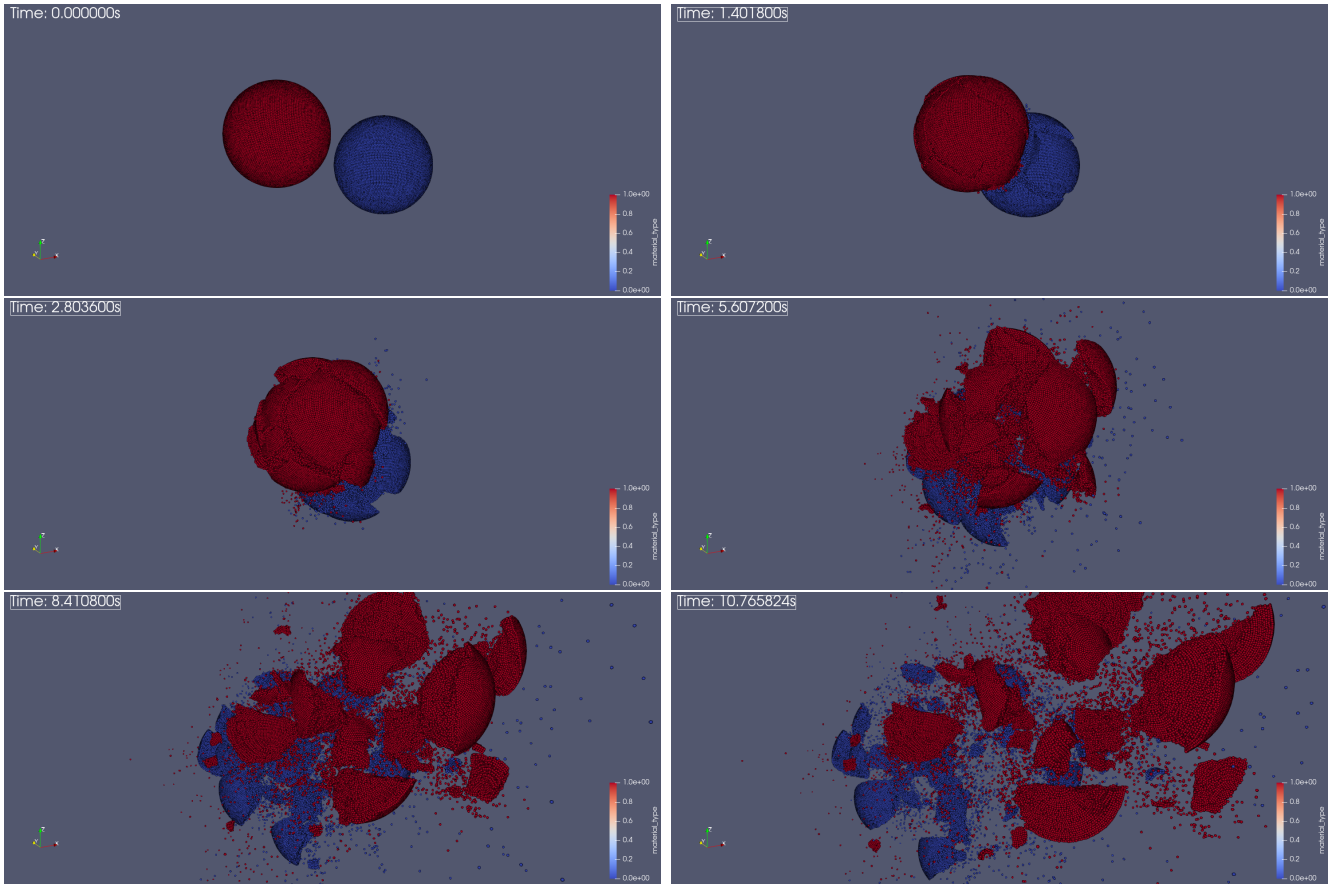
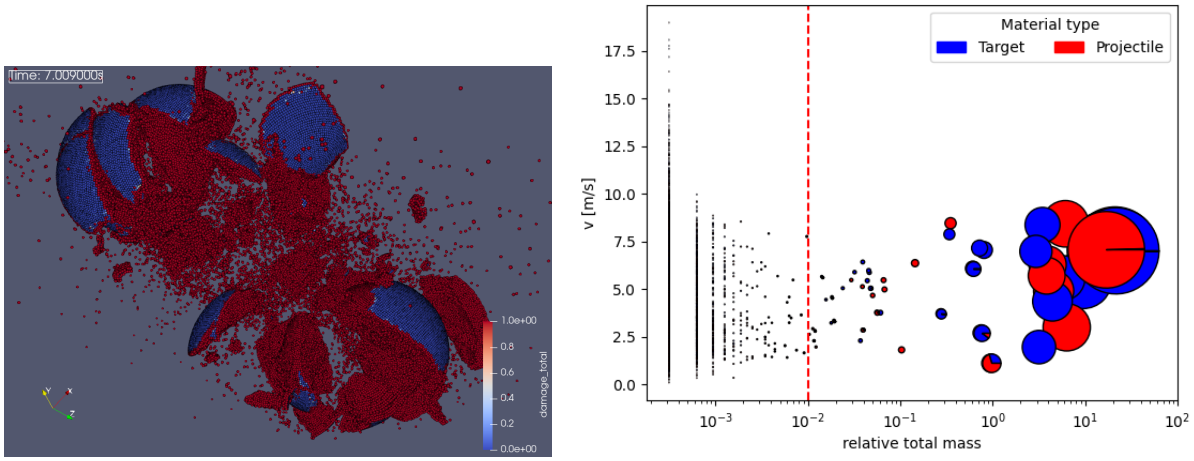


Figure 5.2: Snapshots from the highest impact velocity from 0.9 g/cm^3 density simulation. The time indicates the seconds since the simulation started, and red and blue represent the target and projectile, respectively.

Additionally, figure 5.3 illustrates the damage caused by the bodies after the collision. On the left panel (a) is a snapshot from the simulation and now the colors represent the damage. It is possible to observe the fragments formed and the generated dust. Also, their velocities and relative masses can be seen on the right panel (b).



(a) Snapshot from the damaged particles and graphic of the relative mass of fragments and its velocity.

(b) Plot of the velocity and the relative total mass illustrate the fragments after an SPH collision.

Figure 5.3: Fragments and dust from the highest impact velocity from 0.9 g/cm^3 density simulation.

Identifying the dust production depends on the SPH particle resolution used in the simulation. In our case, it converges to be mostly fragments with less than 0.01% of total mass formed of single fully damaged particles. Figure 5.4 shows the outcome result collision from different simulations, comparing this case with different resolutions of SPH particles. For this reason, we consider any fragment with a mass lower than this percentage to be dust. Summing all those cases is possible to calculate the dust production after the collision.

The comparison between SPH simulation outcomes and the collisional model detailed by Leinhardt and Stewart [2011] reveals a notable divergence. One potential explanation for this disparity lies in the fact that the model by Leinhardt predominantly considers bodies within the gravitational regime, while the dimensions of the macroscopic bodies within the planetary rings exist at the boundary of this regime.

In the scenario featuring within the 0.9 g/cm^3 density simulation (see Figure 5.2), the distinctions between these methods are briefly outlined in table 5.1. However, it is important to note that a direct comparison between these two methods is challenging due to the inherent constraints and nuances within each model. Our aim primarily centers around providing a straightforward comparative analysis with the widely utilized analytical model.

This discrepancy further underscores the necessity of formulating surrogate analytical models

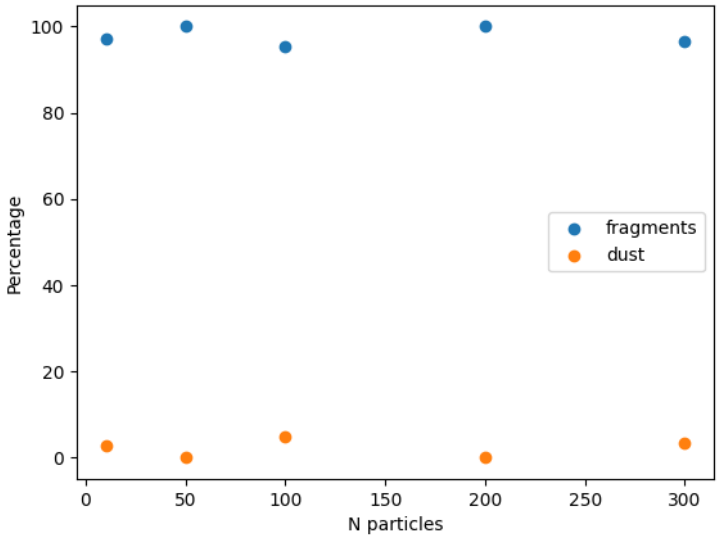


Figure 5.4: Comparing the percentage of dust and fragments generated from different simulations, with the same input parameter, but with different resolutions of SPH particles (N particles).

tailored specifically for macroscopic bodies, shedding light on the imperative need within this domain.

Table 5.1: Comparison between Leinhardt and Stewart [2011] model and SPH simulation using the highest impact velocity from 0.9 g/cm^3 density

	Analytical results:	**SPH results:**
Type collision	$M_{lr} < 0.1M_t$	$0.1M_{tot} < M_{lr} < M_t$
Mlr/Mt	0.000002	28.06%
Mlr	-	1.691805e7 kg
Dust	75.12%	3.27%

To study the effects of changing the density and considering porous bodies, we simulated the same case, now adding porosity. From the highest impact velocity from 0.9 g/cm^3 density simulation, where both bodies have 20m radius, 19.518 m/s impact velocity and 62.81° impact angle. However, adding 55.5% of porosity on the bodies and entering both with the density of 0.5 g/cm^3 and using the P-α model with $\alpha = 1.8$.

Figure 5.5 shows snapshots from the two different simulations with the same input parameter, but one with porosity and the other considering a non-porous body. There is a clear difference between the results, especially in the fragments' outcome and the generation of dust. This happens due to the fact with porous bodies, part of the energy is lost crashing the porous. The bodies suffer more deformation until start to crash, consequently, there is less dust. On top of that, the average of the fragments' velocity is lowered.

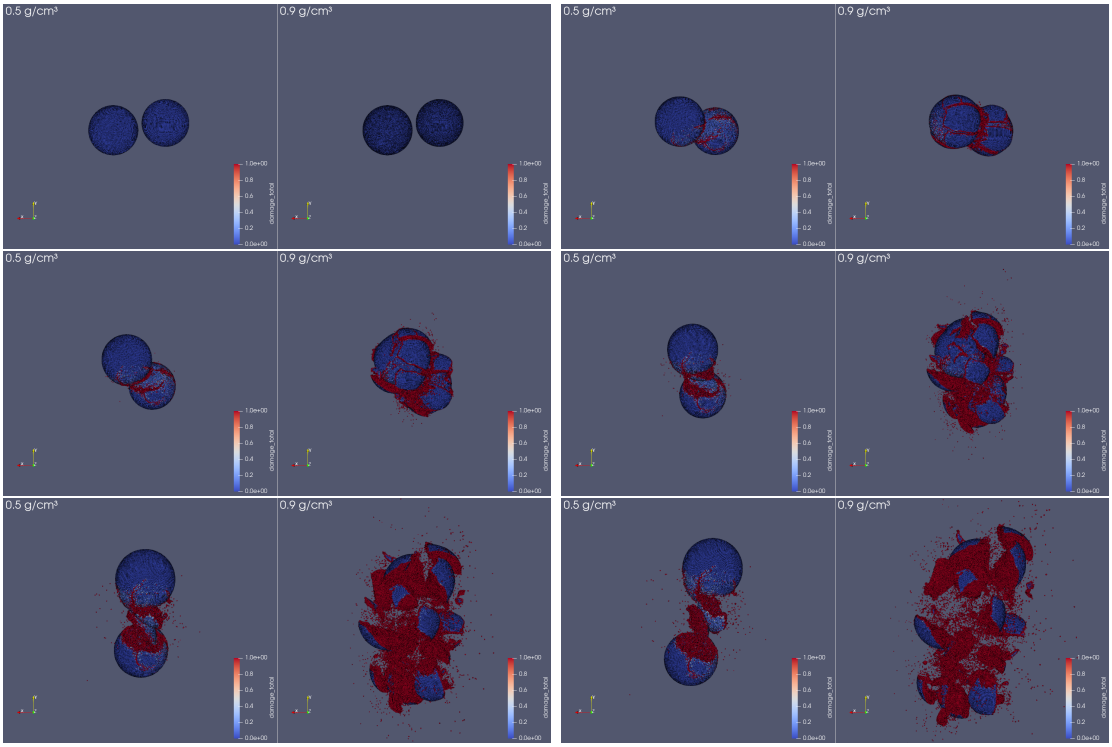


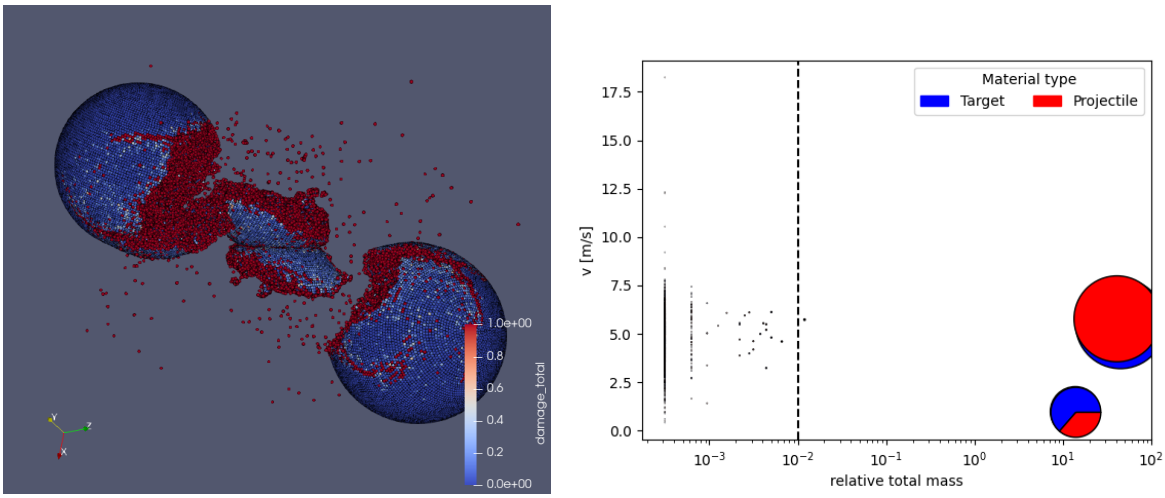
Figure 5.5: Snapshots showing the damage from the highest impact velocity from 0.9 g/cm^3 density simulation. Comparing the cases of porous and non-porous simulation.

Figure 5.6 shows damaging particles in the left panel and the distribution of mass fragments with their velocity. From the damaging visibly distinguish the fragments from the simulation output. Different from figure 5.3, this case has only three fragments formed after the collision. Both target

Table 5.2: Fragments result from highest impact velocity from 0.9 g/cm3 density considering as porous bodies.

	Analytical results:	**SPH results:**
Type collision	$M_{lr} < 0.1M_t$	$0.1M_{tot} < M_{lr} < M_t$
Mlr/Mt	0.000002	44.79%
Mlr	-	7.871318 kg
Dust	75.12%	0.50%

and projectile had fractures and lost part of their masses, in which most turned to compose a new fragment.



(a) Snapshot from the damaged particles and graphic of the relative mass of fragments and its velocity.

(b) Plot of the velocity and the relative total mass illustrate the fragments after an SPH collision. The full colors show the fragments that remained in the arc after the collision.

Figure 5.6: Fragments and dust from the highest impact velocity from 0.9 g/cm^3 density simulation considering porous bodies.

Table 5.2 summarizes the outcome result from SPH simulation and compares it with the prediction from Leinhardt and Stewart [2011]. For the porous case, the difference becomes even more clear. In our SPH simulations, we consider mostly of all bodies physical properties of the bodies and model their strengths, fractures and porous, which cannot be taken into account by the N-bodies simulations.

5.2 Common dynamics and physical properties of rings/arcs

It is well known that giant planets have planetary rings, but understanding the origins, composition and dynamic behavior has always been challenging. Some rings also presented peculiar structures as arcs, like the ones from Saturn and Neptune. The potential formation of those systems is associated with nearby satellites, via the outward dispersal of surface within materials. However, recently unexpected ring structures were found around small bodies such as Chariklo, Chiron and Haumea. These findings show that not only planets have rings, but also other bodies in the Solar System, which are not always generated from satellites.

To explore the origins of those structures is necessary to understand their composition and interactions with the associated material. For that, it is needed to conduct experimental and numerical investigations into the collisional dynamics of aggregates Brisset and Westcott [2021]. In this context, we delineate the shared characteristics among these systems and model potential collisional scenarios, simulating various geometries and impact velocities. In this work, we aim to understand and estimate the production of dust particles in these systems, assuming the presence of macroscopic bodies.

In 2009, the discovery of three faint rings/arcs associated with small moons around Saturn gave new insights into the dynamics within the Saturnian system Hedman et al. [2009b]. These rings found around moons Anthe, Methone, and Pallene were tenuous and previously undetected. They were presumed to be composed of debris ejected from impacts on these tiny moons. Later studies from Miller et al. [2023] on Saturn's rings gave more details about their composition. He demonstrated that the rings are composed mainly of a combination of ice particles, dust, and rocky debris. Also observations from spacecraft, ground telescopes Hubble and Radio occultations at different wavelengths provide data on particle size, ranging from micrometer to meter-size. The balance between gravitational forces, collisions, and interactions between the moons and surrounding material maintains the rings/arcs.

Another system that has arcs is Neptune's Adams ring, investigated by Foryta and Sicardy [1996]. This ring is influenced by gravitational interactions with nearby moons and disturbing forces. The gravitational effects of moonlets trap the ring's material, preventing uniform dispersion and preserving its features, also playing a role in its formation. The resonances with Neptune's moons affect the orbital dynamics of the ring material, they produce patterns within the arcs and contribute to creating their configurations.

Adams ring ranges the size of the particles from dust to more substantial boulders or fragments. The variation in size influences the gravitational interactions among the particles and consequently

the probability of collisions. These encounters potentially lead to alterations in particle distribution, and in some instances, might even facilitate the formation of smaller satellite moons or structures within the ring system. Even if the Adams ring is currently visible, it might not stand indefinitely in astronomical timescales. Ongoing interactions with moons, collisions, and various gravitational influences may cause these arcs to evolve, merge, or dissipate over time, making it a transient ring system.

The discovery of ring systems around two centaurs, Chariklo in 2014 by Braga-Ribas et al. and the potential ring material around Chiron in 2015 by Ortiz et al., changed the perspectives about ring systems. These minor planets, orbiting between Jupiter and Neptune, showed the presence of rings similar to those orbiting gas giants planets. Chariklo's rings were discovered during a star occultation and have been identified as composed primarily of water ice, resembling the composition of Saturn. Likewise, during an occultation event, Chiron showed an unexpected brightness pattern which suggested the possibility of a faint ring system. The existence of rings on relatively small bodies like Chariklo and Chiron implies in complex interactions between gravitational forces, collisions, and potentially the presence of small moons or debris.

These discoveries around centaurs revealed the possibility that other bodies could also present rings. Then a stellar occultation to deduce Haumea's properties, about its size, shape, and density, discovered the presence of a ring Ortiz et al. [2017]. However, different from Chariklo and Chiron, Haumea is much larger and distant from the Sun, having a different dynamic class. Also, it has inclined satellites and a very elongated triaxial shape. The gravitational effects of the oblate body and the inclined satellite on ring stability, reveal intricate interactions. These forces can arise from the body's own gravity, the influence of satellites or moons, and interactions among ring particles themselves. Additionally, irregular shapes or oblate structures of the central body can affect the stability and configuration of the rings.

Recently, another significant discovery was made on a trans-Neptunian asteroid called Quaoar, by Morgado et al. to have a ring system. The fact that these thick rings extend past Quaoar's Roche limit, which is the point at which gravitational forces normally shatter celestial bodies, makes this discovery challenge conventional notions about ring formation, suggesting an unconventional dynamic for such systems. The bodies around Quaoar share similar physical characteristics and behaviors from planetary rings. The ring is made of a mixture of different-sized rock and ice particles. Because of gravitational interactions between different size bodies, the ring might also have gaps or areas of lower density.

The fact that rings can also orbit smaller celestial bodies presents the potential influence of macro-

Table 5.3: Radii and estimated masses for the principal rings/arcs.

System	**ring/arc**	R_{in} **[km]**	R_{out} **[km]**	$\mathbf{v}_m$ **[m/s]**
Saturn	*Methone*	194 660	194 730	2.2352
	Aegaeon	168 010	168 060	2.5091
Neptune	*Adams*	92 873	92 933	2.7696
Chariklo	*Oiapoque*	383.43	397.77	0.7589
	Chuí	401.40	408.20	0.3410
Quaoar	*Q2R 2520*	2 510	2 530	0.7641
	Q1R 4057	4 052	4 062	0.1870
Haumea	*ring*	2 217	2 357	10.463

scopic bodies within these systems. Although collisions and gravitational forces are the main factors that shape these rings, the presence of larger bodies, not only dust, can have a significant impact on their formation and evolution. Besides the contribution to the formation, the macroscopic bodies are also important in stabilizing certain configurations or influencing the distribution of particles within these systems. The presence of such bodies could explain variations in particle sizes, the formation of arcs, and the maintenance of specific ring structures.

When examining the orbital velocities ($\mathbf{v}_m$ in [m/s]) associated with these structures, intriguing similarities emerge (Table: 5.3). For instance, Saturn's moon Methone and Neptune's Adams Ring exhibit velocities of approximately 2.2 to 2.7 meters per second, respectively. Meanwhile, smaller bodies like Chariklo's Oiapoque and Quaoar's Q1R 4057 display significantly lower velocities, around 0.34 to 0.76 meters per second.

This diversity in velocities suggests a potential correlation between the sizes of the bodies and the velocities of their associated rings or arcs. Larger bodies like Saturn and Neptune show relatively higher velocities, whereas smaller bodies like Chariklo and Quaoar exhibit lower velocities. Interestingly, an exception is observed with Haumea, a body with a relatively smaller estimated mass but a high velocity of about 10.46 meters per second. Overall, while there seems to be a general trend linking the sizes of celestial bodies to the velocities of their ring or arc structures, outliers like Haumea suggest that other factors, such as body composition or system dynamics, might play significant roles in determining these velocities since it is also larger them other rings in small bodies.

So we examined the generation of dust resulting from the collision between macroscopic bodies

across various scenarios. To explore the influence on body fragility and the emergence of the meter-size barrier, we systematically altered the bodies' radii, analyzing their effects. Furthermore, we investigated a range of velocities spanning from commonly observed high-impact velocities to lower thresholds where minimal damage occurred, distinguishing between cohesive collisions and mere adhesion.

Supposing a common collision between macroscopic bodies, we distributed the collision setup using a fixed impact angle ($\theta = 30°$) and two same-size bodies. The SPH simulations were conducted using 150,000 particles for each body, target, and projectile, thereby ensuring a sufficiently high resolution even for scenarios involving similar-sized collisions. The runtime of the simulations was primarily dependent on the body's size and the impact velocity, which in turn determined the overall simulated time.

We identify the dust production based on the SPH particle resolution used in the simulation. In our case, it converges to be mostly fragments with less than 0.01% of total mass formed of single fully damaged particles. For this reason, we consider any fragment with a mass lower than this percentage to be dust. Summing all cases, the dust production can be calculated after the collision.

Figure 5.7 shows the final simulation snapshot from Table 5.4, summarizing dust production in same-size body collisions via SPH, considering body radius and collision velocities.

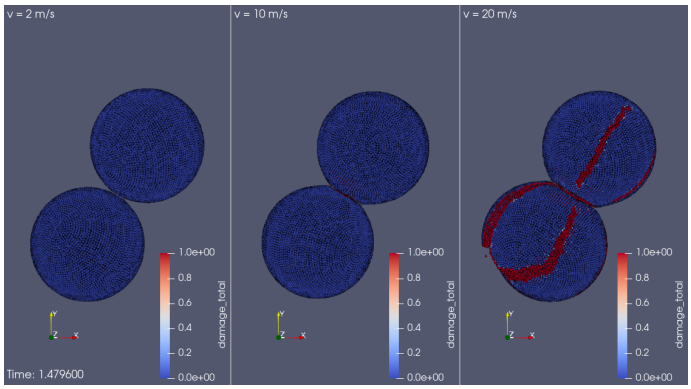
The table 5.4 shows that the dust generation appears to be influenced by both the radius of the bodies and the velocity of collision. At lower velocities (2 m/s), there seems to be no dust generated regardless of the size of the bodies. As velocity increases, the percentage of dust generated escalates, especially with larger bodies. For instance, at 10 m/s, there is a small amount of dust produced for 5m and 10m radius bodies but not for the smaller or larger ones. It appears that there might be a threshold velocity for each body size beyond which dust generation significantly increases.

Table 5.4: Dust generation from different collision setups using a fixed impact angle of 30°.

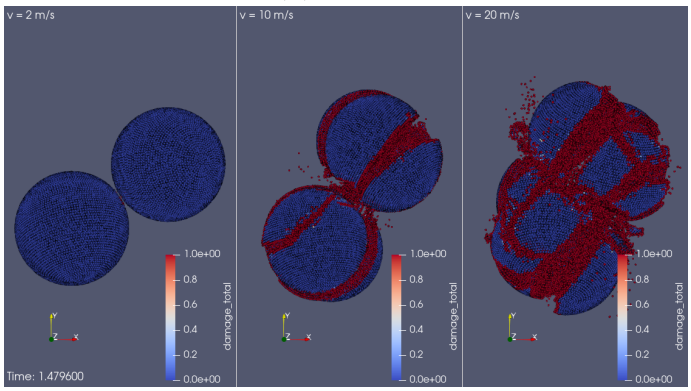
Radius		1 m	5 m	10 m	20 m
	Velocity		Dust produced		
	2 m/s	0.00%	0.00%	0.00%	0.00%
	10 m/s	0.00%	0.14%	0.34%	2.13%
	20 m/s	0.01%	0.62%	0.60%	2.01%

Figure 6.4 provides a visual division between the damaging particles and the resultant distribution of mass fragments along with their corresponding velocities. This representation enables an identification of the fragments produced as an output of the simulation.

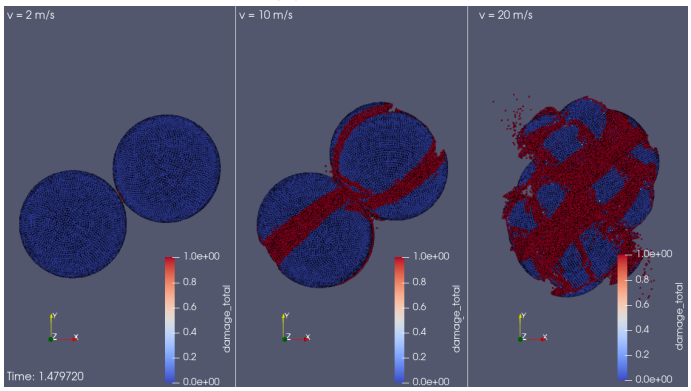
(a) r = 1m



(b) r = 5m



(c) r = 10m



(d) r = 20m

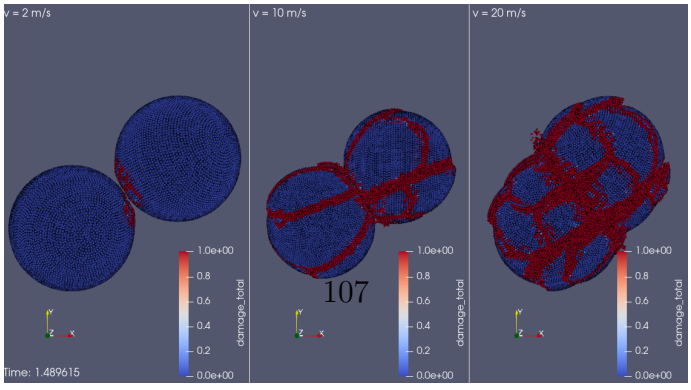
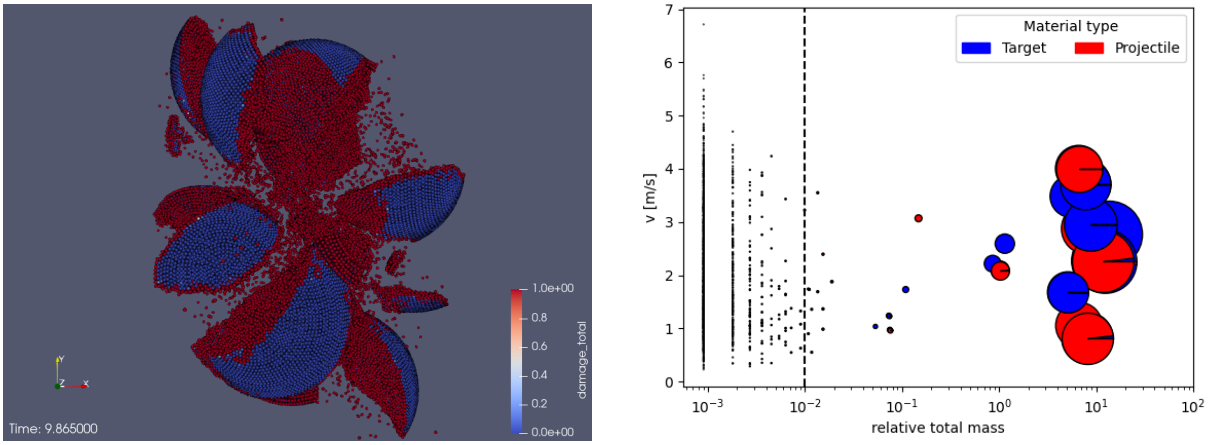


Figure 5.7: Snapshots from different collision setups using a fixed impact angle ($\theta = 30°$).



(a) Snapshot from the damaged particles and (b) Plot of the velocity and the relative total mass graphic of the relative mass of fragments and illustrate the fragments after an SPH collision. its velocity.

Figure 5.8: Fragments and dust from the 10 m/s impact velocity.

Typically, collisions among macroscopic bodies occur at low velocities, with the resultant dust production remaining at consistently low percentages irrespective of the bodies' sizes.

Chapter 6

Formation of small satellite and dust rings at G Arc

The planetary arc formation process is usually related to a satellite presence. The G ring arc existence is associated with the small Aegaeon satellite and the corotation resonance with Mimas confines it Hedman et al. [2007]. This arc is brighter when viewed at higher phase angles, indicating that the particle size distribution that forms these structures is dominated by dust grains (typically from 0.1 to 10 μm). According to Hedman et al. [2007], collisions with Aegaeon would generate the micrometric particles that populate the G ring. However, the dust particles are lost on a scale of a few decades, while the production mechanism requires at least 30,000 years to accumulate enough mass to account for the arc's brilliance.

Lattari [2019] proposed an explanation for the G ring arc formation fitting with the data collected from Cassini. The data indicated the existence of a population of macroscopic bodies immersed in the arc, which would be below the resolution limit of the cameras. They proposed that the collisions from those bodies would generate dust in the arc.

This section aims to validate this hypothesis by taking collision dynamics studies from N-Body simulations as detailed in Lattari [2019] and referenced in V. Lattari and Schaefer [2024]. Then accurately model this collision with specific SPH simulations applied to G arc, alongside data from the preceding chapter.

The SPH method allows for flexible resolution adjustments concerning parameters like density, enabling the exploration of material responses within different pressure and temperature conditions. Our approach involves a hybrid SPH coupled with N-body code, allowing comprehensive simulations encompassing shock propagation, material alteration, and gravitational reformation following the

disruption of small bodies in collisions.

6.1 Numerical Setup

In the field of planetary formation and dynamic studies, accurately simulating collisions in planetary rings poses a significant challenge. The computational expense increases with the number of bodies, especially when also considering the fragments after the collision. To treat this problem often is necessary to simplify the collisions.

The amount of bodies in an N-body simulation makes it more expensive for the integrator, needing more running time, for this reason, collisions are often treated as perfectly inelastic, to be carried out in a reasonable time. However, the bodies after the collision merge entirely and there is no production of debris and fragments. This tends to overestimate the collision efficiency, leading to shorter formation time and more massive bodies.

The inclusion of fragments into simulations is very complicated and it has not been done straightforwardly. This happens because a collision can produce a lot of fragments and the inclusion of those to be handled by N-body integration is impractical. To avoid this issue, many researchers have tried to include only a few of the impact-generated bodies (Chambers [2013], Clement et al. [2019]). Another approach is to use a collision catalog to identify the collision type and the post-impact fragments (i.e., Leinhardt and Stewart [2011]).

Although those approaches have advanced the simulations to be more realistic, they include partially the impact-generated bodies. A comprehensive formation model requires all this material to be included. However, as explained before, it is impractical to include all post-impact fragments as individual objects.

Here, we present a proposal by including the dynamic effect of the post-impact material on resolved bodies in a statistical sense. In this section we present a short-term evolution of the system using N-body simulations, then we use SPH to simulate the collisions obtained at N-body to determine the distributions of the mass, velocity, and orbits of the ejecta, and use the finding to incorporate their effects in the ring to study its stability and formation.

6.1.1 N-Body simulations

Here, we summarize the numerical simulations from V. Lattari and Schaefer [2024], how the collisions were modeled using the N-body integrator REBOUND, and the results of collisions that will be

simulated on SPH.

To determine the initial conditions for the simulations the oblateness parameters for Saturn are available in Hedman et al. [2009a] and the the elements for the satellites from Madeira et al. [2018]. V. Lattari and Schaefer [2024] have made two different sets of simulations, the first including the satellite Aegaeon, while the second without it to understand the effect of the satellite on the particles embedded in the arc.

The total mass of the macroscopic bodies included in the arc 10^{10} kg, which represents the maximum amount of mass that can be distributed into the macroscopic bodies, made of ice with the density of 0.9 g/cm^3 or if they are porous with 0.5 g/cm^3 density. Then it was distributed 20 m size-bodies all over the arc until the sum of the mass of the particles corresponds to the maximum total mass of the arc. The size of these objects was chosen because the Cassini cameras are only able to detect objects with a radius of more than 100 meters (Hedman et al. [2007]). It also takes into account the limit of Leinhard's model.

So now will are outlining the results from V. Lattari and Schaefer [2024] N-body simulations, so that in the sequence we can then demonstrate the collisions carried out at SPH. Figure 6.1 displays velocity heatmaps for collisions between a 20 m radius body and Aegaeon satellite. The left and right graphs depict simulations with densities of 0.5 g/cm^3 and 0.9 g/cm^3 respectively, showcasing collision velocities typically at 5 m/s (ranging from 1 to 15 m/s) and impact angles mostly between 30 and 50 degrees. No significant discrepancy appears between densities, as expected due to density's influence on simulation.

Figure 6.2 illustrates collision heatmaps between two same-sized bodies within a 20 m radius, with upper graphs at 0.5 g/cm^3 density and lower at 0.9 g/cm^3. The left graph considers Aegaeon in the simulation influencing gravitationally, while the right panel is without the small satellite. The result shows a typical relative velocity of around 0.5 m/s, up to 10 m/s depending on positions, and impact angles mainly below 60 degrees, typical at 30 degrees. A significant disparity exists in the distribution of velocities and impact angles when considering collisions between macroscopic bodies (Fig. 6.2) and when they collide with Aegaeon (Fig. 6.1).

The idea of our work is to examine collisions between macroscopic bodies and their impact on Aegaeon. This investigation aims to determine how these collisions might help sustain the dust within the arc against the force of solar radiation pressure. Since this pressure clears small particles within 40 years. In the following sections, we will detail the outcomes of these collisions and estimate the amount of dust produced by different types of collisions.

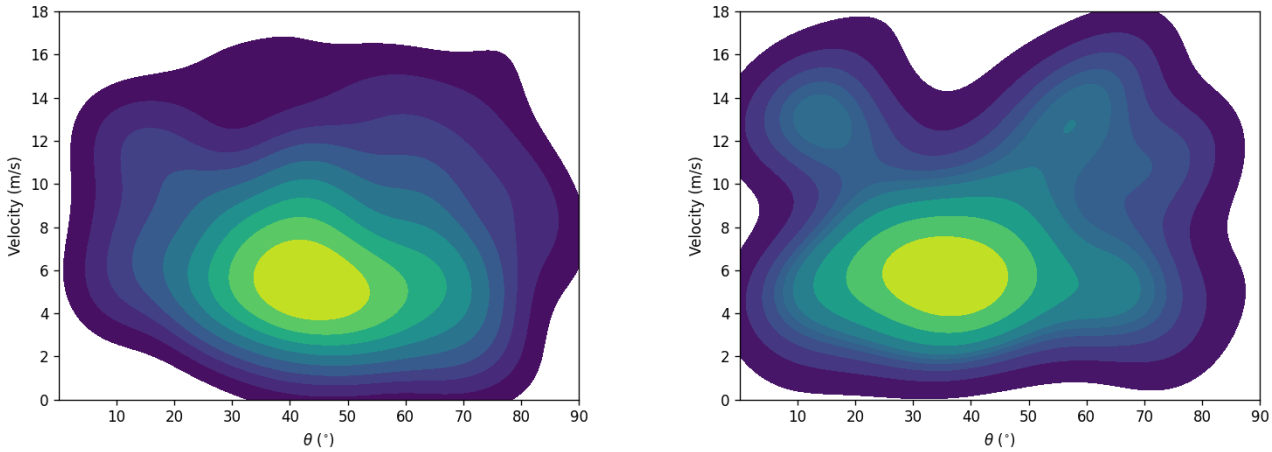


Figure 6.1: The relative velocities in the function of the impact angle (θ) of the collisions between one body within 20 m radius and Aegaeon. In the left graph, we have the simulation using a density equal to 0.5 g/cm^3, while in the right 0.9 g/cm^3. These graphs show that the typical relative velocity of these collisions is 5 m/s and the impact angle mostly happens between 30 and 50 degrees. From V. Lattari and Schaefer [2024].

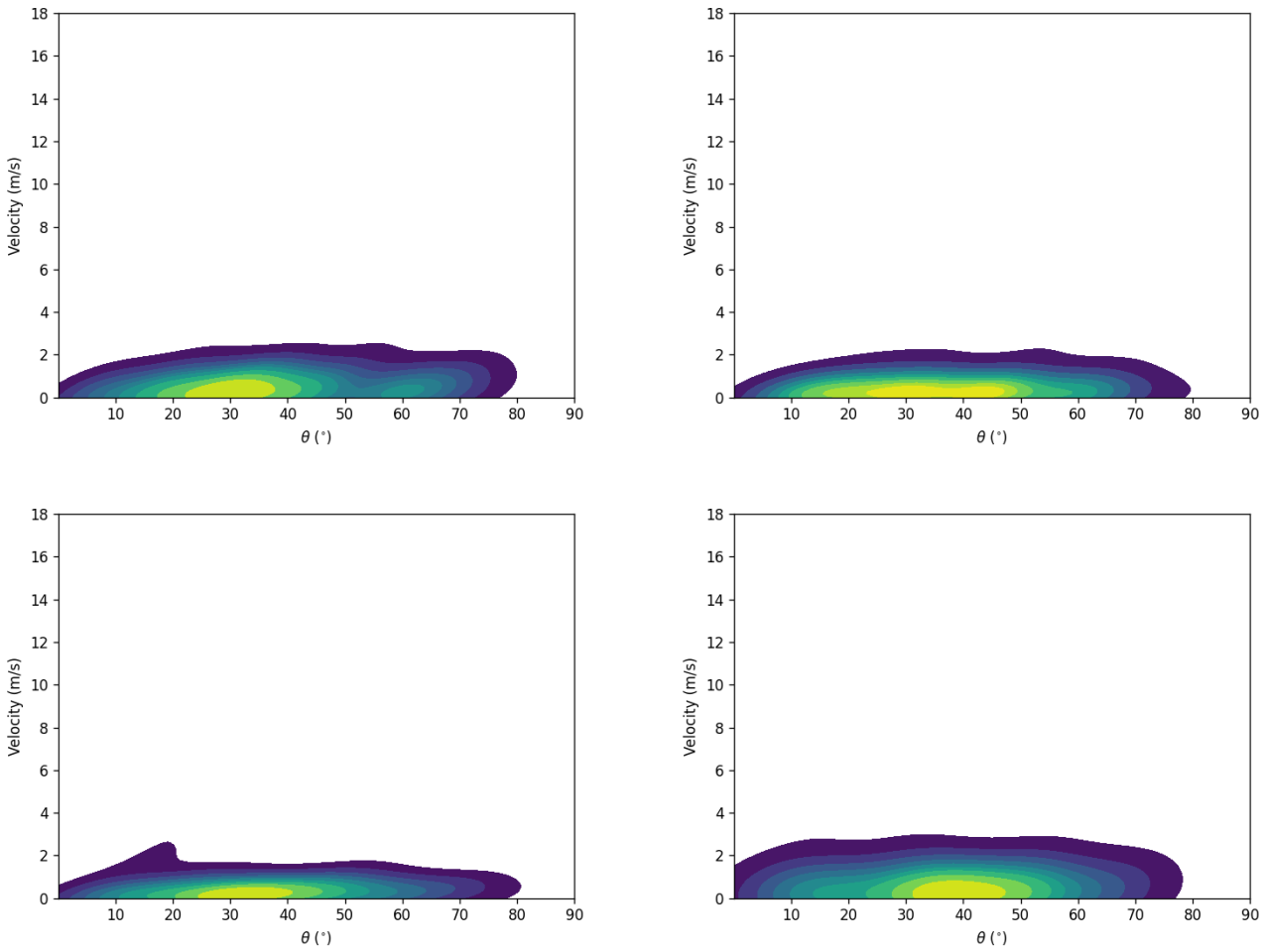


Figure 6.2: The relative velocities in the function of the impact angle (θ) of the collisions between two macroscopic bodies. The upper graphs represent the simulations using a density equal to 0.5 g/cm^3, while the bottom 0.9 g/cm^3. The left graphs represent the simulations including Aegaeon, while the right one's simulations are without the small satellite. These graphs show that Aegaeon affects the distribution of the velocity and impact angle of the collisions between the macroscopic bodies.From V. Lattari and Schaefer [2024].

6.1.2 SPH simulations

With the collision of those macroscopic bodies from the last section, we want to analyze the production of dust and stability from the remaining fragments. Implementing the simulations for this purpose needs to take into account the challenge of including post-impact material without saturating the numerical integrator. A common approach to this problem involves including collision-generated material in a few clusters of bodies with the same mass and uniformly scattering them around the collision point. However, this is an oversimplification of the property of the collision material, since it neglects potentially significant features for the final structure and composition of the system.

So, we developed a computational framework to model collisional dust production by direct combination of N-body computations with dedicated smooth particle hydrodynamics (SPH) collision simulations of differentiated, self-gravitating bodies for each event.

From the results of the N-body simulation displayed in figures 6.2 and 6.1 we started by simulating each collision on SPH. In the N-body simulations, the position, velocity, and dimensions of the bodies are recorded in the next time step after the first contact between them, as shown in the left panel of figure 6.3. Then, it is necessary to remove the overlap from the bodies to be able to establish parameters to analyze each of the collisions.

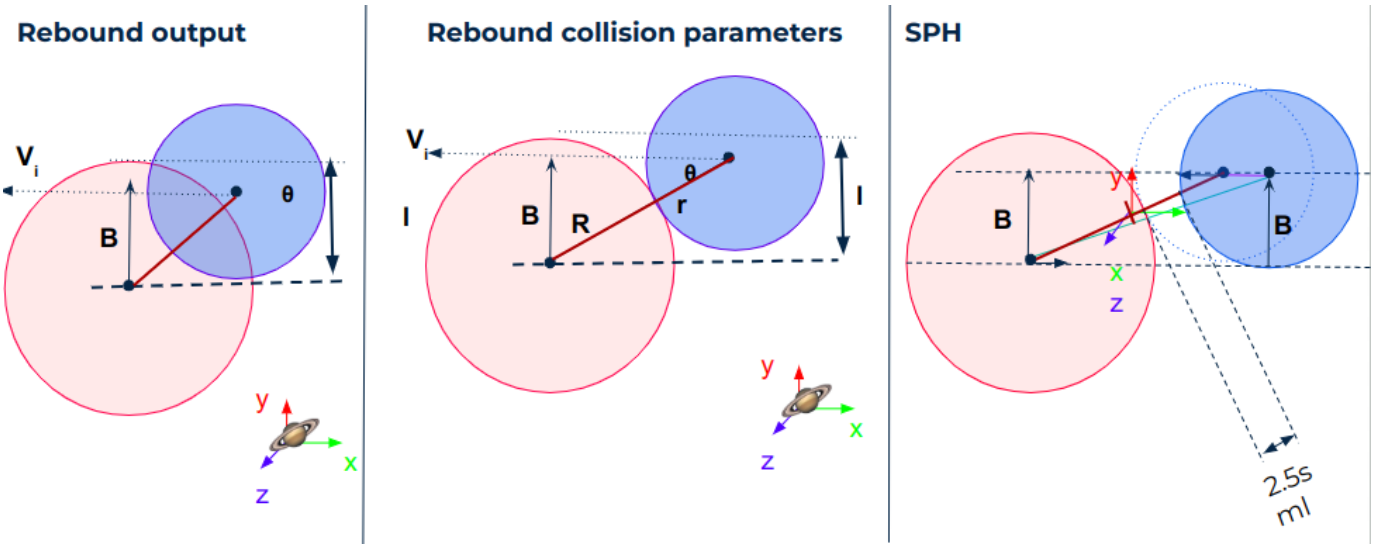


Figure 6.3: Representation of the geometry of a collision on Rebound and SPH.

In the case of the N-body geometry, the target (red) is hit by the projectile (blue) with velocity V_i (Fig. 6.3). θ is the angle of impact, defined at the first contact between the bodies and comprised between the line joining the center of each body and the ray that passes through the velocity projectile

impact. R and r are the target and projectile radii, respectively. The impact parameter is given by $b = \sin\theta = B/(R + r)$. The length l is the projectile's overlap with the target.

The positions and velocities from the N-body simulations are given in relation to the center of the planet. On the other hand, on the SPH those values are numerically large to work on and can generate numerical errors, so instead of using the reference at the planet, we used the centroid of the target and the projectile. So, in the case of SPH simulations, the bodies are placed placed at a mutual distance of $r_{ini} = R + r + 2.5_{\mathrm{sml}}$. It is added to the distance this 2.5_{sml}, where sml means the smoothing length, which is the space and time used to determine the region of influence of the neighboring particles. So the bodies can be distinguished at the start of the simulation.

The projectile and target are both modeled as solid ice bodies. The Tillotson equation of state was used as the input parameters ice Schäfer et al. [2016] to determine the pressure (table A.2). It also included the material strength where the shear strength is limited by the Fish model Fish and M. [1997]. To model tensile fractures, it follows Benz and Asphaug [1994] and the Grady-Kipp fragmentation model and the standard artificial viscosity by Monaghan and Lattanzio [1985] (table A.3). The Barnes-Hut tree was used to calculate the gravitational forces between the particles.

The post-collision analysis needed for the identification of fragments, including their dynamics and composition, and the study of dust production is made of two main steps. Initially, a friends-of-friends algorithm identifies all spacially directly connected clumps of SPH particles, considering them as "fragments". This process takes place before the identification of gravitationally bound "aggregates" of those fragments, which is part of the second step. Starting from a seed aggregate consisting of the most massive fragment and all those mutually gravitationally bound to it, an iterative algorithm adds or removes fragments from this seed aggregate (its centroid) until convergence. After identification of the largest aggregate, the process is repeated to find the second-largest one, starting from the most massive fragment not yet incorporated into the largest aggregate Burger et al. [2017]

In all SPH simulations, we use 150 000 particles for each body, target and projectile. This ensures a reasonable resolution even for scenarios involving similar-sized collisions. The runtime depends mainly on particle number and impact velocity (which determines the overall simulated time), whereas a single SPH simulation presented here, including all pre-and post-processing, takes on the order of one to three weeks to complete.

6.2 Analysis and discussion

In this section, we discuss the outcome of the collisions for the SPH simulations using the density of 0.9 g/cm^3. We aim to analyze the dust production of the bodies' pos-impact. Table 5.4 (sec. 5.2) shows that dust generation appears to be influenced by both the radius of the bodies and the velocity of collision. At lower velocities (2 m/s), there seems to be no dust generated regardless of the size of the bodies. As velocity increases, there's a noticeable increase in the percentage of dust production, especially for larger radius bodies. For instance, at 10 m/s, there's a small amount of dust produced for 5m and 10m radius bodies but not for the smaller or larger ones. It appears that there might be a threshold velocity for each body size beyond which dust generation significantly increases.

After examining the collisions occurring in the G arc between macroscopic bodies, as shown in Figure 6.2, we can use the set of simulations presented for a generic system, with results detailed in table 5.4 from section 5.2, to analyze the generation of dust resulting from collisions between macroscopic bodies. Therefore, now we are taking a further look into the common and efficient collision that happens in the arc for the identification of fragments and dust production. That is the case of two equal 20 m-sized bodies at v = 10 m/s and $\theta = 30°$ angle of impact (Fig. 6.5).

Figure 6.4 the resultant distribution of mass fragments along with their corresponding velocities. From the dash line is possible to visibly distinguish the fragments from dust in the simulation output. This case generated 2.13% of the dust of the total mass, which was the most efficient case for dust generation among different impact velocities.

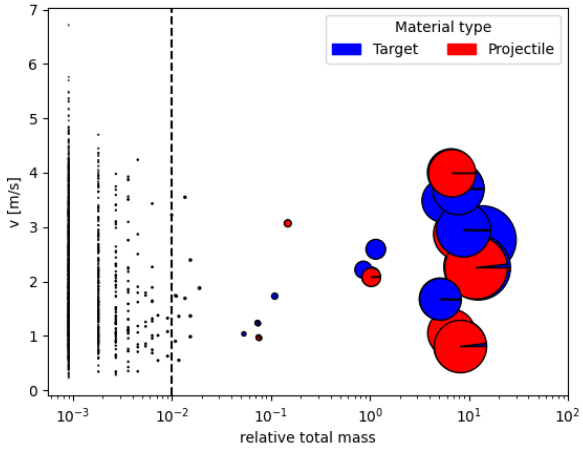


Figure 6.4: Fragments and dust from the 10 m/s impact velocity. The plot of the velocity and the relative total mass illustrate the fragments after an SPH collision.

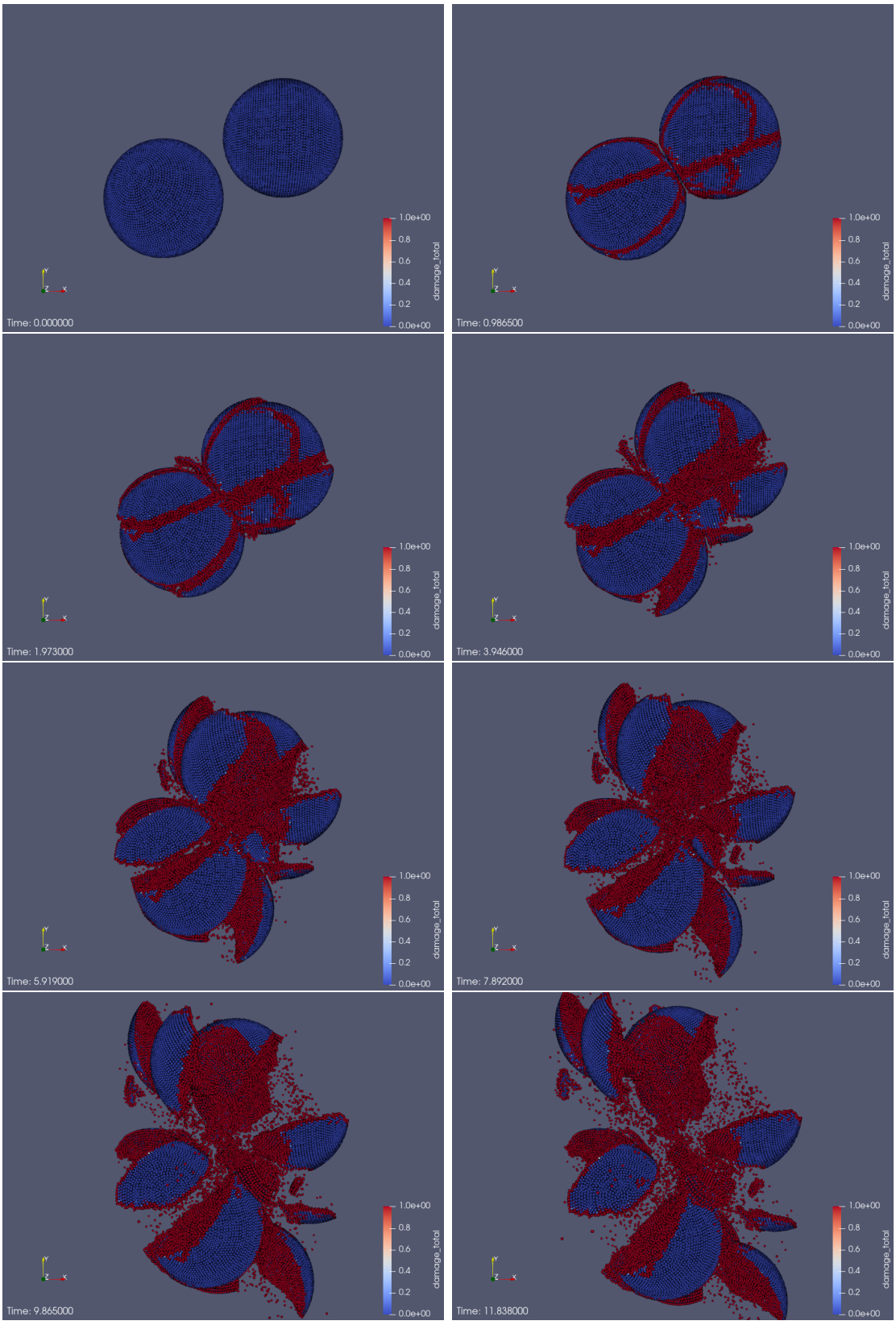


Figure 6.5: Snapshots showing the damage from two equal 20 m-sized bodies at v = 10 m/s and $\theta = 30^\circ$ angle of impact.

Typically, collisions among macroscopic bodies occur at low velocities, with the resultant dust production remaining at consistently low percentages irrespective of the bodies' sizes. To explore alternative mechanisms for dust generation, we investigated the possibility of these macroscopic bodies producing dust when they collide with Aegaeon, which represents approximately 40% of the overall collisions and occurs in the arc.

So based on the 6.1, which showed that the relative velocity of these collisions of the macroscopic bodies with Aegaeon is 5 m/s and the impact angle mostly happens between 30 and 50 degrees, we run another set of SPH simulations to see the dust production. Those simulations consider a 240 m-sized target impacted by a 10 or 20 m-sized projectile at 5 or 10 m/s and an angle of 30° or 45°. The projectile was modeled using 10,000 SPH particles, while Aegaeon, comprised 1,000,000 SPH particles. To maintain adequate resolution and consistent characteristic lengths, only a section of the satellite was simulated.

We used the Tillotson equation of state as described in Benz and Asphaug [1995] and presented in SI units in table A.2 to model the materials. The damage model was implemented using the Weibull parameters, with the values for water ice taken from table A.3. The material constants can be found in figure 4.9. We used the shear modulus from A.1, while the yield stress and melting energy were calculated based on information from Fish and M. [1997]. The determination of the dust production is based on the SPH particle resolution utilized in the simulation. In our case, it primarily consists of fragments, with less than 0.1% of the projectile mass. In this case, we do not consider the sum masses of both bodies because Aegaeon is taken partially and in any case, even if Aegaeon suffers damage, it does not generate dust.

Table 6.1 provides the production of dust resulting from collisions of a projectile on Aegaeon, based on different projectile velocities and impact angles. Considering the data provided in the table, the values fluctuate significantly based on the projectile's velocity and impact radius. However, in typical collisions with Aegaeon, we can consider that for a moderate velocity and impact angle, the average dust production might be around 10%.

Table 6.1: Dust production from a collision with a projectile with Aegaeon.

	Velocity	Dust produced	
Projectile:		r =10 m $\theta = 30°$	r = 20 m $\theta = 45°$
	5 m/s	9.38%	6.63%
	10 m/s	17.37%	23.53%

In the same way, as we have done for collisions involving only macroscopic bodies, let's further examine the most efficient scenario for dust generation in collisions with Aegaeon. In Figure 6.6, the mass fragment distribution and corresponding velocities are depicted from an SPH simulation. Resultant, the projectile experienced disruption, with 76.47% of its total mass transforming into smaller fragments, while the remaining 23.53% contributed to a mass of generated dust particles.

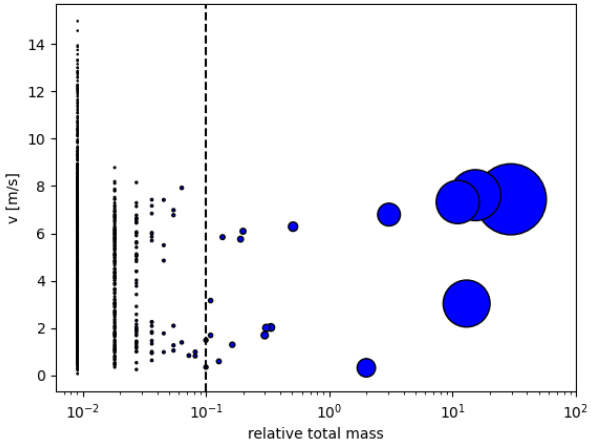


Figure 6.6: Fragments and dust from the 10 m/s impact velocity. The plot of the velocity and the relative total mass illustrate the fragments after an SPH collision.

The dust production of the collision from the macroscopic bodies with themselves and with Aegeaon is highly dependent on the specific parameters of the impact. While the collision with Aegeaon (table 6.1) suggests more substantial dust production, especially at higher velocities, the collision just between the bodies (table 5.4) shows minimal dust generation at lower velocities and smaller projectile sizes, with noticeable increases only under more extreme conditions. The collisions with Aegeaon report higher percentages of dust production, with values ranging from 6.63% to 23.53%. On the other hand, collision between the bodies significantly lower percentages, with most values below 3%, and many scenarios (especially at lower velocities) producing no dust. Also, the snapshot of the simulations makes clear the easier disruption of the bodies when they collide with the small satellite Aegaeon, being almost destroyed and not impacting much of the satellite's surface.

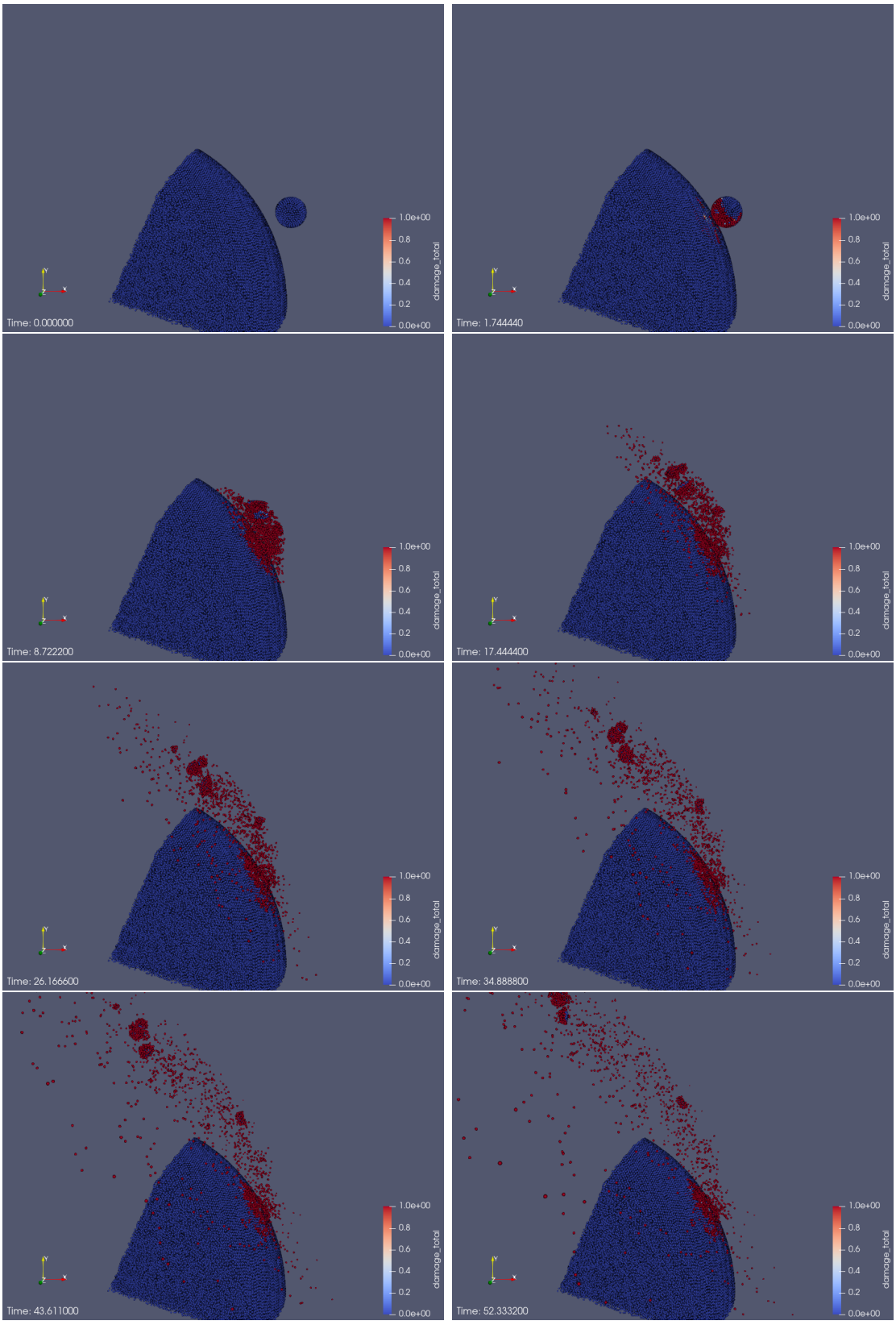


Figure 6.7: Snapshots of Aegeon impacted by a 20 m-sized projectile at 10 m/s and an angle of 45°.

6.2.1 Dynamics and evolution of the post-collisional fragments

We aim to examine what occurs to the fragments within the arc following the collision. To achieve this, we examined the fragments that resulted from the collision, considering their masses and velocities. We then performed a rebound simulation including Saturn, Mimas, and these fragments located in various sections of the arc. The objective was to comprehend their stability, whether they would remain within the arc or gain energy and be lost after the collision, then escape from the system.

So to understand this dynamic, we choose an energetic collision that could occur in the arc. After breaking apart the fragments from the dust, we return the fragments to the N-body simulations to study their stability in the arc. First, the fragments were introduced at the center of the resonance, which is more stable, and their mass and velocity were taken from SPH simulations in the planet's frame of reference.

Figure 6.8 is a flowchart illustrating each step of the process and simulation we conducted to comprehend the hybrid approach in fully studying the dynamics from the arc.

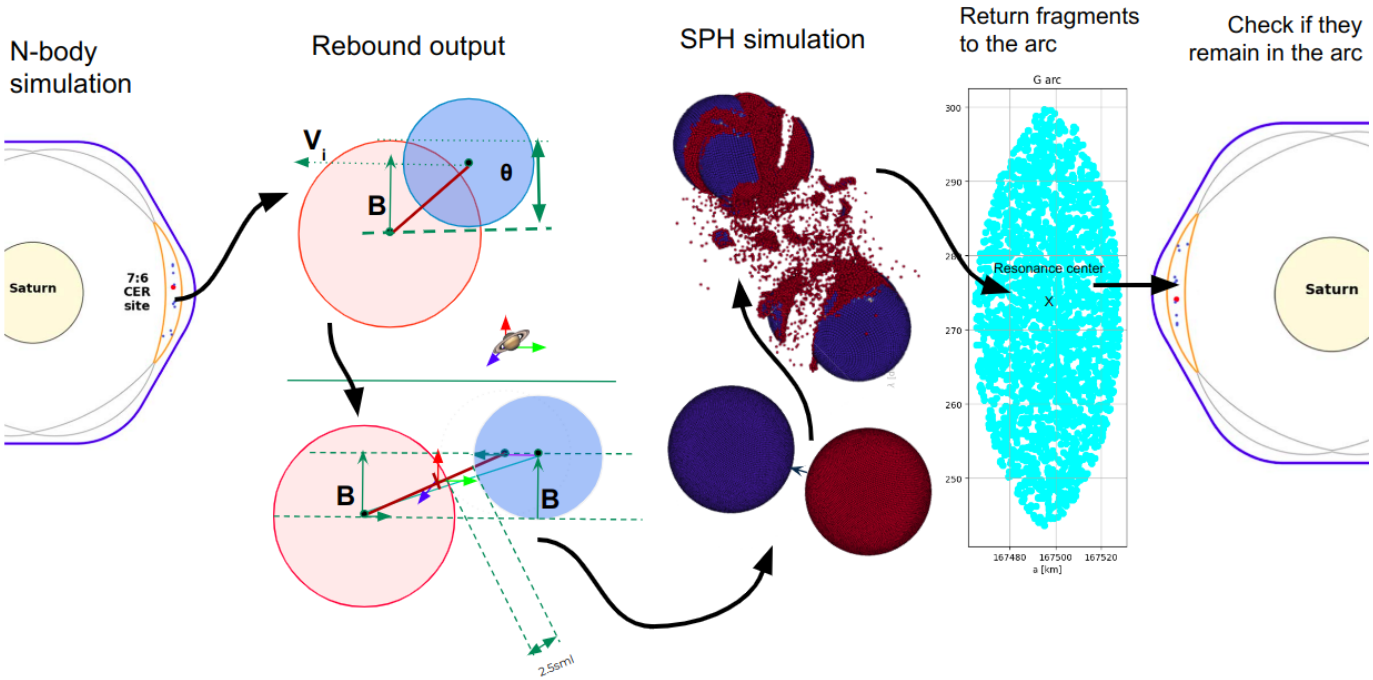


Figure 6.8: Schematic of the hybrid approach, showing each step from the record of collision happened in the N-body simulation, then transformed to be incorporated to the SPH simulation and then finally taking the post-collisional fragment in the center of the arc resonance and integrate again in the N-body simulation.

First was carried out the N-body simulation using Rebound by Lattari et al. [2022] distributing macroscopic bodies of 20m size-radius all over the arc until the sum of the mass of the particles corresponds to the maximum total mass of the arc, then integrating Saturn, Mimas and Aegaeon. Then every collision was recorded in the next time step after the event happened, since the collision cannot be recorded at the exact moment, it shows an overlap between the bodies. So first we remove the overlap and then take the impact parameter that will be used in the SPH simulation. Before simulating the collision in the SPH simulation, a safety distance of 2.5 times the smoothing length (sml) is added between the bodies. This distance ensures that the bodies are recognized separately. Additionally, the center of reference is changed from Saturn to the barycenter of the bodies. Then the SPH simulation is performed taking into account all the solid body mechanics that cannot be considered in an N-body simulation. Once the fragments are distinguishable, a modified script from Burger et al. [2017] is used to calculate the mass and velocities of all post-impact material. Finally, the fragments are integrated again in the N-body simulation with all previous configurations, but without the other macroscopic bodies. They are then placed in the center of the resonance, or in the center of the arc, which is supposed to be the most stable region. Then, their stability in the system is checked to determine whether they would remain in the arc or not.

The verification of the post-collisional fragments remains in the arc system checks if they are confined by the 7:6 corotation resonance within the satellite Mimas, analyzing the resonant angles 7:6 CER (corotation eccentric resonance) and 7:6 CLB (lindblad resonance) Hedman et al. [2007]. Further explanation about those resonances and how to verify if a body is trapped in can be seen at V. Lattari and Schaefer [2024].

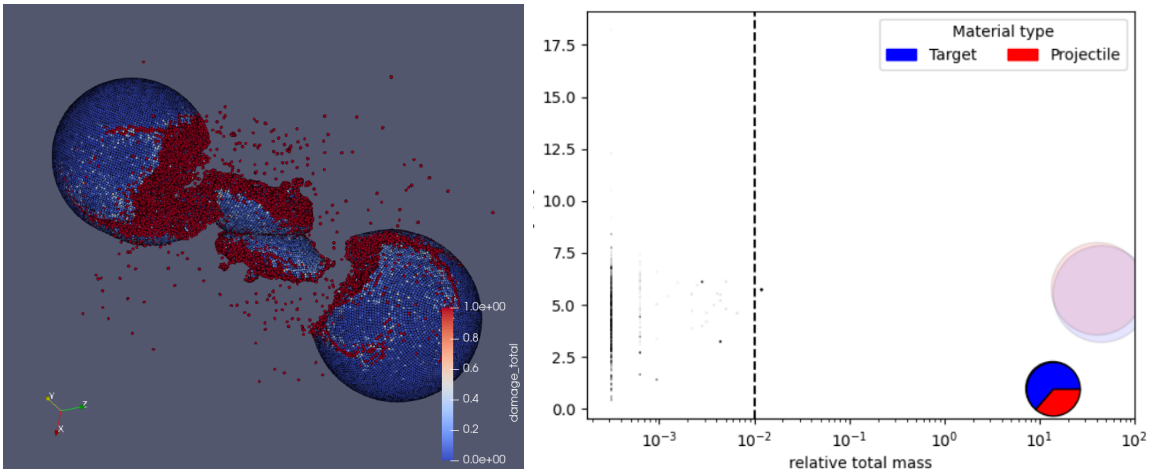
To do this, we are using the same collision scenario mentioned in section 5.1 for both porous and non-porous cases. In this collision, each body has a 20-meter radius, an impact velocity of 19.518 meters per second, and an impact angle of 62.81 degrees.

Analyzing first the porous case, the table 6.2 and figure 6.9 shows the SPH result of this collision, which this case has only three post-collisional fragments. Both target and projectile had fractures and lost part of their masses, in which most turned to compose a new fragment. Figure 6.9 the left panel (a) shows damaging particles from the last snapshot which the fragments can be distinguished and the right panel presents the velocity and mass percentage of those corresponding fragments.

The material resulting from this collision was returned to the N-body simulation and analyzed which one was kept in resonance in the arc. To verify if a material is kept trapped by the resonance and still in the arc is needed to analyze the resonant angles and geometric elements over time, a deep explanation of how this process is done is provided at V. Lattari and Schaefer [2024]. However, figure

6.10 graphically reproduces the behavior of this post-collisional material, showing the time evolution of geometric elements a and resonant angle Φ_{CR} The "CR" in the graphic represents the center of the resonance and "Frag" the post-collisional material, which can be a fragment or dust, ranging from least massive to most massive. Then when this material is librating around the center of the resonance, it remains in the arc, but when they are circulating, they are lost from the arc system.

Correlating the figure 6.10 with 6.9(b), the first three materials are the visible large fragments, the two largest ones are circulating and consequently were lost from the arc. Instead, the third fragment remained in the arc. To represent it in the 6.9(b), the lost ones are presented in transparent color. When analyzing the fully the post-collisional material of this porous collision, the majority escaped from the arc after the collision, which accounted for 86% of the total mass, while the remaining 14% remained in the arc.



(a) Snapshot from the damaged particles and graphic of the relative mass of fragments and its velocity.

(b) Plot of the velocity and the relative total mass illustrate the fragments after an SPH collision. The full colors show the fragments that remained in the arc after the collision.

Figure 6.9: Fragments and dust from the highest impact velocity from 0.9 g/cm^3 density simulation considering porous bodies.

Table 6.2: Fragments result from highest impact velocity from 0.9 g/cm^3 density

SPH results	**Mass percentage**
Escaped mass	86%
Remaining mass	14%

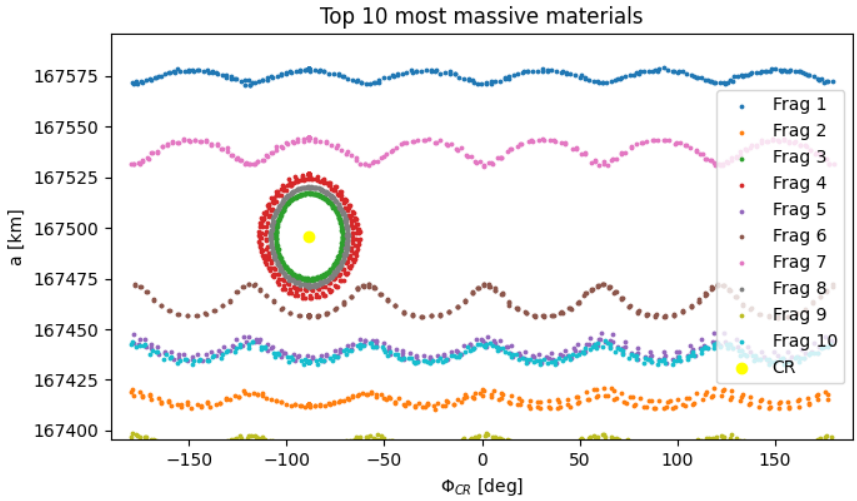
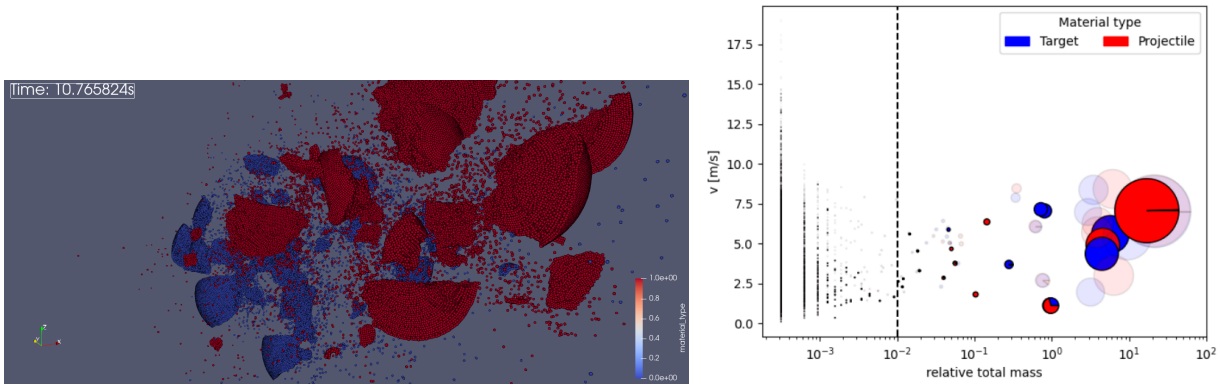


Figure 6.10: Stability in the G arc of the post-collisional material of porous bodies.

In the previous collision case, we considered solid ice bodies without porosity. Figure 6.11 shows the remaining fragments in the arc. Compared to the porous case, the bodies were more damaged and fractured, resulting in more fragments. However, this result does not affect whether the post-collisional material would remain in the arc. Tables 6.3 and 6.12 present the remaining fragments in the arc, showing that for this geometry and impact speed, the fragments that remain in the arch are very similar percentage as in the case of porosity. Furthermore, figure 6.12 represents the behavior of the post-collisional material in the frame of the center of resonance. Interestingly, "Frag 4" was observed to circulate and then librate in another site of the resonance and librate again. This behavior illustrates that following a collision, certain fragments have the potential to escape from the G arc and might populate another arc.

Table 6.3: Fragments result from highest impact velocity from 0.9 g/cm^3 density

SPH results	**Mass percentage**
Escaped mass	82%
Remaining mass	18%



(a) Snapshot from the damaged particles and graphic of the relative mass of fragments and its velocity.

(b) Plot of the velocity and the relative total mass illustrate the fragments after an SPH collision. The full colors show the fragments that remained in the arc after the collision.

Figure 6.11: Fragments and dust from the highest impact velocity from 0.9 g/cm^3 density simulation.

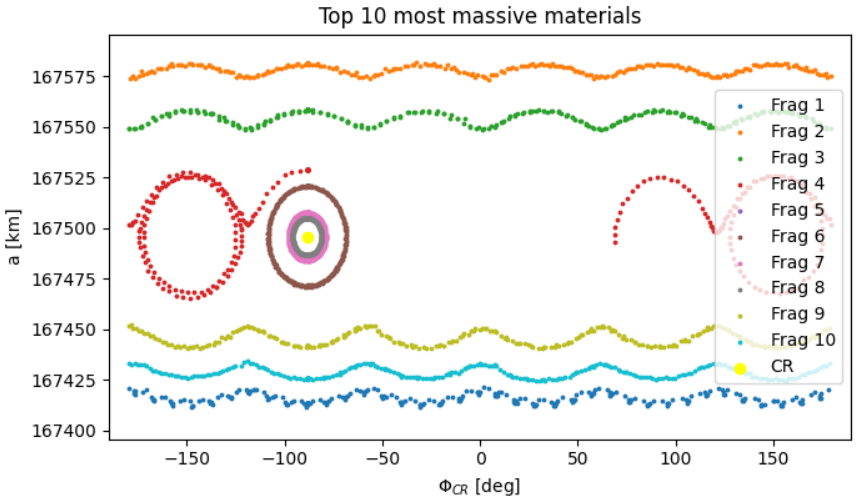


Figure 6.12: Stability in the G arc of the post-collisional material of non porous bodies.

Those results were done by placing the barycenter of the SPH simulation near the center of the Arc (point A from Fig. 6.13). Next, we want to investigate whether the fragments would be retained or lost if it was placed in a different position. Figure 6.13 illustrates the positions at different locations of the arc where we simulated the evolution of the fragments post-impact. The tables 6.5 and 6.4 indicate whether each fragment placed at different points would remain or not in the Arc after the collision.

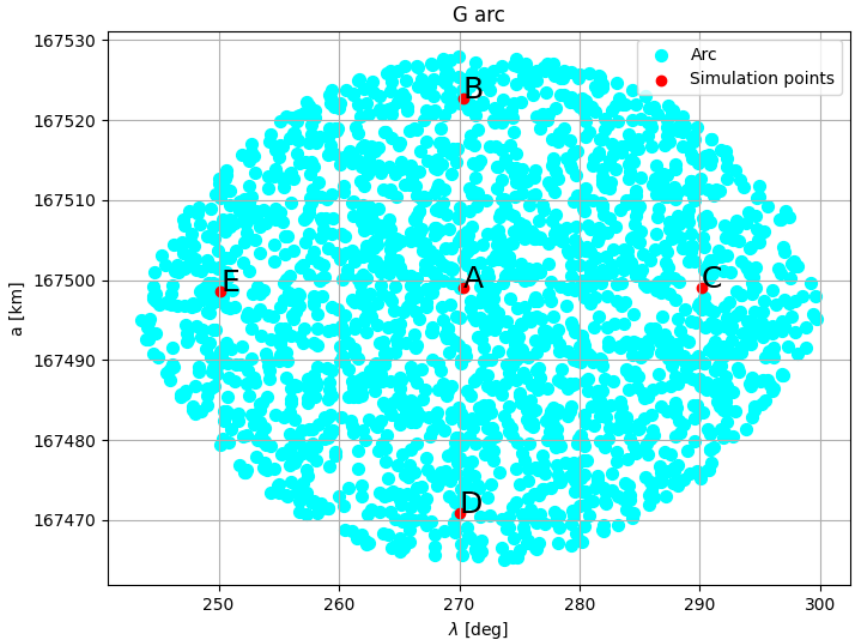


Figure 6.13: Illustration of G arc and the location where fragments were placed.

Those results show that there is not a preference region if an energetic collision happens would be more prominent for the fragments to remain in the arch or not. Also, we found that collisions occur throughout the arc region. This is in agreement with the findings from A'Hearn et al. [2019] who investigated the implications of close encounters between massive bodies on the formation and stability of ring arcs observed in planetary systems.

Table 6.4: Larger fragments from the porous case, showing if they placed at different regions would remain (R) or be lost (L) after the collision.

Fragments	A	B	C	D	E	**v**	**mss %**
1	L	L	L	L	L	5,53	29.88
2	L	L	L	L	L	5,78	22.69
3	R	R	R	L	L	0,99	16.43
4	R	L	R	R	L	5,73	13.08
5	L	L	L	L	L	4,61	11.76
6	L	R	R	L	L	4,81	5.56
7	L	L	R	R	L	6,13	0.01

Table 6.5: Larger fragments from the non-porous case, showing if they placed at different regions would remain (R) or be lost (L) after the collision.

Fragmento	A	B	C	D	E	v	mss %
1	L	L	L	L	L	7,05	13.08
2	L	L	L	L	L	7,07	12.42
3	L	L	L	L	L	5,50	9.46
4	R	L	L	R	R	3,00	7.21
5	L	L	L	L	L	8,43	6.32
6	R	L	R	R	L	5,58	5.70
7	R	L	L	R	L	4,91	4.59
8	R	L	R	R	L	4,36	4.56
9	L	R	R	L	L	6,28	4.42
10	L	L	L	L	L	5,70	4.17
11	L	L	L	L	L	8,37	3.93
12	L	R	L	L	L	1,96	3.82
13	L	L	R	R	L	6,98	3.17
14	R	L	R	R	R	1,12	2.93
15	R	L	R	R	L	7,05	2.47
16	L	R	R	L	L	2,71	1.51
17	L	L	L	L	L	7,15	1.05
18	L	R	R	L	L	6,09	0.94
19	L	L	L	L	L	8,46	0.91
20	L	L	L	L	L	7,88	0.80
21	L	R	R	L	L	3,72	0.74
22	R	R	R	L	L	6,36	0.60
23	R	R	R	L	L	1,82	0.35
24	L	L	L	L	L	4,99	0.33
25	L	L	L	L	L	5,47	0.27

Chapter 7

Final remarks

The studies of the dynamics of planetary rings are usually based on numerical simulations of N-bodies, where collisions involving small particles are generally considered constructive, this means that they generate a new body whose mass is the sum of the masses of the particles involved and the total linear momentum is preserved. This approximation works reasonably well for the up to a few meter-sized bodies. However, observations have shown that the rings are mainly formed by centimeter to meter-sized particles. This is supposed to be a consequence of inefficient models of generation of dust and formation of moonlets, in which two bodies collide and result in another body without a part of the matter being able to be lost.

We reviewed the numerical models available and implemented new methods to analyze the physical properties of those macroscopy bodies. In this sense, we performed simulations based on simulations of SPH and we analyzed the numerical errors related to the limited of the models due to the size of the bodies used in the system. Additionally, we conducted simulations to validate and compare our findings with laboratory experiments, particularly those involving plastic models representing rigid and porous ice. This comprehensive approach aimed to refine our understanding of planetary ring dynamics and particle formation.

The efficiency of all the mechanisms described in this project relies on the assumed strength of the small body in which these mechanisms act. That shows the importance of the definition of strength is so clear and we must address this problem by defining the strength for different kinds of materials inside the planetary rings. The proper strength model describes the disruption of a small body compatible with laboratory experiments. This is the concern to implement and compare different models in the simulations to realize more realistic experiments.

It was important to perform simulations to define the SPH initial conditions for our real systems.

This process reduced the numerical errors, thereby improving the accuracy and reliability of the simulations. We compared the plasticity models available at Fish and M. model is more suitable for the material we are interested in. Working with a plasticity model which takes into account parameters like friction angle and cohesion, can make outcomes more likely according to the laboratory results. Moreover, the SPH particles carry the physical properties of the bodies, so their initial conditions and arrangement can affect the outcome of a simulation. For this reason, we tested different particles' geometry and using the concentric shells produced by SEAGen script reduced the numerical errors, avoided symmetry effects, and the energy stabilizes faster not causing any unexpected damage. Along with particles' geometry, we studied the possibility of a simulation to overestimate the density and it was found that using 55 neighbors was the best fit.

In this work, we also compared our results with the semi-analytical approach and found a divergence of SPH fragment outcomes with Leinhardt and Stewart [2011]. This can be due to the fact Leinhardt and Stewart [2011] method considers only objects in the gravitational regime, and the macroscopic bodies of the arcs have sizes that are in the boundary or even outside of this regime of this regime. For the porous case there was a more clear difference with the prediction of the outcomes from Leinhardt and Stewart [2011], since such property cannot be taken into account.

Then using the defined initial conditions, we performed simulations to study the collision between the possible macroscopic bodies at the G arc of Saturn. Using short-term evolution of the system using N-body simulations, we used SPH to simulate the collisions obtained at N-body and then determined the distributions of the mass, velocity, and orbits of the ejecta. The fragments produced from the SPH simulations were returned to the N-body simulations to analyze if they would remain in the G arc. The fragments with higher velocities tend to make the fragments escape from the system. However, we found that bodies with porosity changed the outcome and generation of dust because they lose energy to crash the porous and deform until start to crash, but the general percentage of lost mass is similar to the non-porous case.

We studied the effects of varying parameters, such as object sizes (both target and impactor), differences in material, porosity and also different geometries and impact velocities. For then be able to understand how those parameters influence dust production. Our next step is then introduce a surrogate model for N-bodies simulations that gives fast, reliable answers for the masses and velocities outcome from collisions between bodies in rings, as a function of the colliding masses and their impact velocity and angle.

Altogether the project is defined by collision outcomes, the physical properties of macroscopic bodies embedded in rings, by implementing into the SPH simulations models that agree with labo-

ratory experiments. Finally, the dynamics, production of dust production could be studied through the grid of simulations we performed, varying physical properties, like sizes and densities, and the impact parameters, such as impact angle and velocity.

This project can also be applied to other systems, using our hybrid method with SPH and N-body simulations, which possibly have macroscopic bodies. Likewise as our presented study for the G arc, through investigations of impacts between interplanetary dust particles on nearby satellites' surfaces, that can not produce sufficient particles to replenish the dusty ring population, we evaluate the possibility for this system to have macroscopic bodies, by performing numerical simulations using N-bodies integrations, to analyze the dynamics of a sample of dust and bodies under the effects of disturbing forces, drag forces, and the gravitational effects of nearby satellites. Then perform SPH collision to understand the physical properties of those bodies and their possible densities, cohesion, fragmentation, or porosity. Then finally, match the results using macroscopic bodies with the profiles of the rings from the observations data, to prove those macroscopic bodies are sufficient to maintain the replacement of visible dust particles in the rings.

Bibliography

Joseph A A'Hearn, Matthew M Hedman, and Maryame El Moutamid. Dynamics of multiple bodies in a corotation resonance: Conserved quantities and relevance to ring arcs. *The Astrophysical Journal*, 882(1):66, 2019.

G. Backhaus. L. m. kachanov, foundations of the theory of plasticity (applied mathematics and mechanics, volume 12). x + 482 s. m. 262 abb. amsterdam/london 1971. north-holland publishing company. preis geb. dfl. 90.00. *ZAMM - Zeitschrift für Angewandte Mathematik und Mechanik*, 53 (5):358–359, 1973. doi: 10.1002/zamm.19730530515.

W. Benz and E. Asphaug. Impact simulations with fracture. i. method and tests. *Icarus*, 107(1): 98–116, jan 1994. doi: 10.1006/icar.1994.1009.

W. Benz and E. Asphaug. Simulations of brittle solids using smooth particle hydrodynamics. *Computer Physics Communications*, 87(1-2):253–265, may 1995. doi: 10.1016/0010-4655(94)00176-3.

W. Benz and E. Asphaug. Catastrophic disruptions revisited. *Icarus*, 142(1):5–20, nov 1999. doi: 10.1006/icar.1999.6204.

Willy Benz. Velocity collisions and the growth of planetesimals. *Space Science Reviews*, 92(1/2): 279–294, 2000. doi: 10.1023/a:1005207631229.

Richard P. Binzel, Michael A'Hearn, Erik Asphaug, M.Antonella Barucci, Michael Belton, Willy Benz, Alberto Cellino, Michel C. Festou, Marcello Fulchignoni, Alan W. Harris, Alessandro Rossi, and Maria T. Zuber. Interiors of small bodies: foundations and perspectives. *Planetary and Space Science*, 51(7-8):443–454, jun 2003. doi: 10.1016/s0032-0633(03)00051-5.

F. Braga-Ribas, B. Sicardy, J. L. Ortiz, C. Snodgrass, F. Roques, R. Vieira-Martins, J. I. B. Camargo, M. Assafin, R. Duffard, E. Jehin, J. Pollock, R. Leiva, M. Emilio, D. I. Machado, C. Colazo, E. Lellouch, J. Skottfelt, M. Gillon, N. Ligier, L. Maquet, G. Benedetti-Rossi, A. Ramos

Gomes, P. Kervella, H. Monteiro, R. Sfair, M. El Moutamid, G. Tancredi, J. Spagnotto, A. Maury, N. Morales, R. Gil-Hutton, S. Roland, A. Ceretta, S. h. Gu, X. b. Wang, K. Harpsøe, M. Rabus, J. Manfroid, C. Opitom, L. Vanzi, L. Mehret, L. Lorenzini, E. M. Schneiter, R. Melia, J. Lecacheux, F. Colas, F. Vachier, T. Widemann, L. Almenares, R. G. Sandness, F. Char, V. Perez, P. Lemos, N. Martinez, U. G. Jørgensen, M. Dominik, F. Roig, D. E. Reichart, A. P. LaCluyze, J. B. Haislip, K. M. Ivarsen, J. P. Moore, N. R. Frank, and D. G. Lambas. A ring system detected around the centaur (10199) chariklo. *Nature*, 508(7494):72–75, mar 2014. doi: 10.1038/nature13155.

Julie Brisset and Connor Westcott. Collisional viscosity of icy dust aggregates in planetary rings. In *AAS/Division for Planetary Sciences Meeting Abstracts*, volume 53 of *AAS/Division for Planetary Sciences Meeting Abstracts*, page 503.06, October 2021.

C. Burger, T. I. Maindl, and C. M. Schäfer. Transfer, loss and physical processing of water in hit-and-run collisions of planetary embryos. *Celestial Mechanics and Dynamical Astronomy*, 130(1), dec 2017. doi: 10.1007/s10569-017-9795-3.

Christoph Burger. Equilibrium conditions of multi-material particle distributions in sph simulations of colliding planetesimals in early planetary systems. 2015. doi: 10.25365/THESIS.39591.

Michael Carroll and Albert C. Holt. Suggested modification of the p-alpha model for porous materials. *Journal of Applied Physics*, 43(2):759–761, feb 1972. doi: 10.1063/1.1661203.

J.E. Chambers. Late-stage planetary accretion including hit-and-run collisions and fragmentation. *Icarus*, 224(1):43–56, may 2013. doi: 10.1016/j.icarus.2013.02.015.

Matthew S Clement, A Morbidelli, S N Raymond, and N A Kaib. A record of the final phase of giant planet migration fossilized in the asteroid belt's orbital structure. *Monthly Notices of the Royal Astronomical Society: Letters*, 492(1):L56–L60, dec 2019. doi: 10.1093/mnrasl/slz184.

Gareth S. Collins, H. Jay Melosh, and Boris A. Ivanov. Modeling damage and deformation in impact simulations. *Meteoritics & Planetary Science*, 39(2):217–231, feb 2004. doi: 10.1111/j.1945-5100.2004.tb00337.x.

Joshua E. Colwell and Larry W. Esposito. A numerical model of the uranian dust rings. *Icarus*, 86 (2):530–560, aug 1990. doi: 10.1016/0019-1035(90)90232-x.

Imke de Pater and Jack J. Lissauer. *Planetary Sciences*. Cambridge University Press, 2001. ISBN 9780521482196.

Imke de Pater, Heidi B. Hammel, Seran G. Gibbard, and Mark R. Showalter. New dust belts of uranus: One ring, two ring, red ring, blue ring. *Science*, 312(5770):92–94, apr 2006. doi: 10.1126/science.1125110.

Walter Dehnen and Hossam Aly. Improving convergence in smoothed particle hydrodynamics simulations without pairing instability. *Monthly Notices of the Royal Astronomical Society*, 425(2): 1068–1082, aug 2012. doi: 10.1111/j.1365-2966.2012.21439.x.

S. F. Dermott, C. D. Murray, and A. T. Sinclair. The narrow rings of jupiter, saturn and uranus. *Nature*, 284(5754):309–313, mar 1980. doi: 10.1038/284309a0.

Steven Diehl, Gabriel Rockefeller, Christopher L. Fryer, David Riethmiller, and Thomas S. Statler. Generating optimal initial conditions for smoothed particle hydrodynamics simulations. *Astronomical Society of Australia*, November 2012.

Neil Divine. Five populations of interplanetary meteoroids. *Journal of Geophysical Research*, 98(E9): 17029, 1993. doi: 10.1029/93je01203.

D. C. Drucker and W. Prager. Soil mechanics and plastic analysis or limit design. *Quarterly of Applied Mathematics*, 10(2):157–165, 1952. doi: 10.1090/qam/48291.

Alexandre Emsenhuber, Martin Jutzi, and Willy Benz. SPH calculations of mars-scale collisions: The role of the equation of state, material rheologies, and numerical effects. *Icarus*, 301:247–257, feb 2018. doi: 10.1016/j.icarus.2017.09.017.

Larry W. Esposito. *Planetary Rings*. Cambridge University Press, mar 2014. doi: 10.1017/cbo9781139236966.

Fish and Anatoly M. Ice strength as a function of hydrostatic pressure and temperature. 97(6), 1997. ISSN Cold Regions Research and Engineering Laboratory (U.S.). URL `http://hdl.handle.net/11681/9233`.

A. M. Fish. Creep and yield model of ice under combined stress. 1991.

Dietmar W. Foryta and Bruno Sicardy. The dynamics of the neptunian adams ring's arcs. *Icarus*, 123(1):129–167, September 1996. ISSN 0019-1035. doi: 10.1006/icar.1996.0146.

David A. Fulk and Dennis W. Quinn. An analysis of 1-d smoothed particle hydrodynamics kernels. *Journal of Computational Physics*, 126(1):165–180, jun 1996. doi: 10.1006/jcph.1996.0128.

R. E. Gagnon and P. H. Gammon. Triaxial experiments on iceberg and glacier ice. *Journal of Glaciology*, 41(139):528–540, 1995. doi: 10.3189/s0022143000034869.

R. A. Gingold and J. J. Monaghan. Smoothed particle hydrodynamics: theory and application to non-spherical stars. *Monthly Notices of the Royal Astronomical Society*, 181(3):375–389, dec 1977. doi: 10.1093/mnras/181.3.375.

D.E. Grady and M.E. Kipp. Continuum modelling of explosive fracture in oil shale. *International Journal of Rock Mechanics and Mining Sciences &amp Geomechanics Abstracts*, 17(3):147–157, jun 1980. doi: 10.1016/0148-9062(80)91361-3.

J.P. Gray and J.J. Monaghan. Numerical modelling of stress fields and fracture around magma chambers. *Journal of Volcanology and Geothermal Research*, 135(3):259–283, jul 2004. doi: 10.1016/j.jvolgeores.2004.03.005.

J.P. Gray, J.J. Monaghan, and R.P. Swift. SPH elastic dynamics. *Computer Methods in Applied Mechanics and Engineering*, 190(49-50):6641–6662, oct 2001. doi: 10.1016/s0045-7825(01)00254-7.

E. Grün, H.A. Zook, H. Fechtig, and R.H. Giese. Collisional balance of the meteoritic complex. *Icarus*, 62(2):244–272, may 1985. doi: 10.1016/0019-1035(85)90121-6.

M. M. Hedman, N. J. Cooper, C. D. Murray, K. Beurle, M. W. Evans, M. S. Tiscareno, and J. A. Burns. Aegaeon (saturn liii), a g-ring object. 2009a. doi: 10.48550/ARXIV.0911.0171.

Matthew M. Hedman, Joseph A. Burns, Matthew S. Tiscareno, Carolyn C. Porco, Geraint H. Jones, Elias Roussos, Norbert Krupp, Chris Paranicas, and Sascha Kempf. The source of saturn's g ring. *Science*, 317(5838):653–656, aug 2007. doi: 10.1126/science.1143964.

M.M. Hedman, C.D. Murray, N.J. Cooper, M.S. Tiscareno, K. Beurle, M.W. Evans, and J.A. Burns. Three tenuous rings/arcs for three tiny moons. *Icarus*, 199(2):378–386, feb 2009b. doi: 10.1016/j.icarus.2008.11.001.

K. Holsapple, I. Giblin, K. Housen, A. Nakamura, and E. Ryan. Asteroid impacts: Laboratory experiments and scaling laws. In *Asteroids III*, pages 443–462. 2002. URL `https://ui.adsabs.harvard.edu/abs/2002aste.book..443H`.

K A Holsapple. The scaling of impact processes in planetary sciences. *Annual Review of Earth and Planetary Sciences*, 21(1):333–373, may 1993. doi: 10.1146/annurev.ea.21.050193.002001.

Keith A. Holsapple. On the "strength" of the small bodies of the solar system: A review of strength theories and their implementation for analyses of impact disruptions. *Planetary and Space Science*, 57(2):127–141, feb 2009. doi: 10.1016/j.pss.2008.05.015.

W. B. Hubbard, A. Brahic, B. Sicardy, L.-R. Elicer, F. Roques, and F. Vilas. Occultation detection of a neptunian ring-like arc. *Nature*, 319(6055):636–640, feb 1986. doi: 10.1038/319636a0.

Fridtjov Irgens. *Continuum Mechanics*. Springer, 2008. ISBN 9783540742982.

Stephen J. Jones. The confined compressive strength of polycrystalline ice. *Journal of Glaciology*, 28 (98):171–178, 1982. doi: 10.3189/s0022143000011874.

Martin Jutzi. SPH calculations of asteroid disruptions: The role of pressure dependent failure models. *Planetary and Space Science*, 107:3–9, mar 2015. doi: 10.1016/j.pss.2014.09.012.

Martin Jutzi, Willy Benz, and Patrick Michel. Numerical simulations of impacts involving porous bodies. *Icarus*, 198(1):242–255, nov 2008. doi: 10.1016/j.icarus.2008.06.013.

Martin Jutzi, Patrick Michel, Kensuke Hiraoka, Akiko M. Nakamura, and Willy Benz. Numerical simulations of impacts involving porous bodies. *Icarus*, 201(2):802–813, jun 2009. doi: 10.1016/j.icarus.2009.01.018.

D Koschny. Impacts into ice–silicate mixtures: Ejecta mass and size distributions. *Icarus*, 154(2): 402–411, dec 2001. doi: 10.1006/icar.2001.6708.

Alexander V. Krivov, Miodrag Sremčević, Frank Spahn, Valeri V Dikarev, and Konstantin V Kholshevnikov. Impact-generated dust clouds around planetary satellites: spherically symmetric case. *Planetary and Space Science*, 51(3):251–269, mar 2003. doi: 10.1016/s0032-0633(02)00147-2.

Manfred A. Lange, Thomas J. Ahrens, and Mark B. Boslough. Impact cratering and spall failure of gabbro. *Icarus*, 58(3):383–395, jun 1984. doi: 10.1016/0019-1035(84)90084-8.

Victor Lattari, Rafael Sfair, and Patricia Buzzatto. Formation of small satellite and dust rings at g arc. *(in preparation)*, 2022.

Victor Correa Lattari. Master's thesis, UNESP, 2019.

Zoë M. Leinhardt and Sarah T. Stewart. COLLISIONS BETWEEN GRAVITY-DOMINATED BODIES. i. OUTCOME REGIMES AND SCALING LAWS. *The Astrophysical Journal*, 745(1):79, dec 2011. doi: 10.1088/0004-637x/745/1/79.

J. Leliwa-Kopystyński, M.J. Burchell, and D. Lowen. Impact cratering and break up of the small bodies of the solar system. *Icarus*, 195(2):817–826, jun 2008. doi: 10.1016/j.icarus.2008.02.010.

Larry D. Libersky and A. G. Petschek. Smooth particle hydrodynamics with strength of materials. In *Advances in the Free-Lagrange Method Including Contributions on Adaptive Gridding and the Smooth Particle Hydrodynamics Method*, pages 248–257. Springer Berlin Heidelberg, 1990. doi: 10.1007/3-540-54960-9_58.

Larry D. Libersky, Albert G. Petschek, Theodore C. Carney, Jim R. Hipp, and Firooz A. Allahdadi. High strain lagrangian hydrodynamics. *Journal of Computational Physics*, 109(1):67–75, nov 1993. doi: 10.1006/jcph.1993.1199.

Larry D. Libersky, Phil W. Randles, Ted C. Carney, and David L. Dickinson. Recent improvements in SPH modeling of hypervelocity impact. *International Journal of Impact Engineering*, 20(6-10): 525–532, jan 1997. doi: 10.1016/s0734-743x(97)87441-6.

L. B. Lucy. A numerical approach to the testing of the fission hypothesis. *The Astronomical Journal*, 82:1013, dec 1977. doi: 10.1086/112164.

Gustavo Madeira, R Sfair, D C Mourão, and S M Giuliatti Winter. Production and fate of the g ring arc particles due to aegaeon (saturn LIII). *Monthly Notices of the Royal Astronomical Society*, 475 (4):5474–5479, jan 2018. doi: 10.1093/mnras/sty179.

P Michel. Formation of asteroid families by catastrophic disruption: Simulations with fragmentation and gravitational reaccumulation. *Icarus*, 160(1):10–23, nov 2002. doi: 10.1006/icar.2002.6948.

Patrick Michel, Willy Benz, Paolo Tanga, and Derek C. Richardson. Collisions and gravitational reaccumulation: Forming asteroid families and satellites. *Science*, 294(5547):1696–1700, nov 2001. doi: 10.1126/science.1065189.

Patrick Michel, Willy Benz, and Derek C. Richardson. Disruption of fragmented parent bodies as the origin of asteroid families. *Nature*, 421(6923):608–611, feb 2003. doi: 10.1038/nature01364.

Patrick Michel, Willy Benz, and Derek C. Richardson. Catastrophic disruption of asteroids and family formation: a review of numerical simulations including both fragmentation and gravitational reaccumulations. *Planetary and Space Science*, 52(12):1109–1117, oct 2004. doi: 10.1016/j.pss.2004.07.008.

Patrick Michel, Willy Benz, and Derek C. Richardson. Catastrophic disruption of pre-shattered parent bodies. *Icarus*, 168(2):420–432, apr 2004b. doi: 10.1016/j.icarus.2003.12.011.

Kelly E. Miller, Gianrico Filacchione, Jeffrey Cuzzi, Philip D. Nicholson, Matthew M. Hedman, Kevin Baillie, Robert E. Johnson, Wei-Ling Tseng, Paul R. Estrada, J. Hunter Waite, Mauro Ciarniello, Cécile Ferrari, Zhimeng Zhang, Amanda Hendrix, and Julianne I. Moses. The composition of saturn's rings. November 2023.

J. J. Monaghan and J. C. Lattanzio. A refined particle method for astrophysical problems. *Astronomy and Astrophysics*, 149(1):135–143, August 1985. URL `https://ui.adsabs.harvard.edu/abs/1985A&A...149..135M`.

B. E. Morgado, B. Sicardy, F. Braga-Ribas, J. L. Ortiz, H. Salo, F. Vachier, J. Desmars, C. L. Pereira, P. Santos-Sanz, R. Sfair, T. de Santana, M. Assafin, R. Vieira-Martins, A. R. Gomes-Júnior, G. Margoti, V. S. Dhillon, E. Fernández-Valenzuela, J. Broughton, J. Bradshaw, R. Langersek, G. Benedetti-Rossi, D. Souami, B. J. Holler, M. Kretlow, R. C. Boufleur, J. I. B. Camargo, R. Duffard, W. Beisker, N. Morales, J. Lecacheux, F. L. Rommel, D. Herald, W. Benz, E. Jehin, F. Jankowsky, T. R. Marsh, S. P. Littlefair, G. Bruno, I. Pagano, A. Brandeker, A. Collier-Cameron, H. G. Florén, N. Hara, G. Olofsson, T. G. Wilson, Z. Benkhaldoun, R. Busuttil, A. Burdanov, M. Ferrais, D. Gault, M. Gillon, W. Hanna, S. Kerr, U. Kolb, P. Nosworthy, D. Sebastian, C. Snodgrass, J. P. Teng, and J. de Wit. A dense ring of the trans-neptunian object quaoar outside its roche limit. *Nature*, 614(7947):239–243, February 2023. ISSN 1476-4687. doi: 10.1038/s41586-022-05629-6.

Carl D. Murray and Stanley F. Dermott. *Solar System Dynamics*. Cambridge University Press, feb 2000. doi: 10.1017/cbo9781139174817.

Jean-Paul Nadreau and Bernard Michel. Yield and failure envelope for ice under multiaxial compressive stresses. *Cold Regions Science and Technology*, 13(1):75–82, oct 1986. doi: 10.1016/0165-232x(86)90009-1.

J. L. Ortiz, R. Duffard, N. Pinilla-Alonso, A. Alvarez-Candal, P. Santos-Sanz, N. Morales, E. Fernández-Valenzuela, J. Licandro, A. Campo Bagatin, and A. Thirouin. Possible ring material around centaur (2060) chiron. *A&A 576, A18 (2015)*, January 2015. doi: 10.1051/0004-6361/201424461.

J. L. Ortiz, P. Santos-Sanz, B. Sicardy, G. Benedetti-Rossi, D. Bérard, N. Morales, R. Duffard, F. Braga-Ribas, U. Hopp, C. Ries, V. Nascimbeni, F. Marzari, V. Granata, A. Pál, C. Kiss, T. Pribulla, R. Komžík, K. Hornoch, P. Pravec, P. Bacci, M. Maestripieri, L. Nerli, L. Mazzei, M. Bachini, F. Martinelli, G. Succi, F. Ciabattari, H. Mikuz, A. Carbognani, B. Gaehrken, S. Mottola, S. Hellmich, F. L. Rommel, E. Fernández-Valenzuela, A. Campo Bagatin, S. Cikota, A. Cikota, J. Lecacheux, R. Vieira-Martins, J. I. B. Camargo, M. Assafin, F. Colas, R. Behrend, J. Desmars, E. Meza, A. Alvarez-Candal, W. Beisker, A. R. Gomes-Junior, B. E. Morgado, F. Roques, F. Vachier, J. Berthier, T. G. Mueller, J. M. Madiedo, O. Unsalan, E. Sonbas, N. Karaman, O. Erece, D. T. Koseoglu, T. Ozisik, S. Kalkan, Y. Guney, M. S. Niaei, O. Satir, C. Yesilyaprak, C. Puskullu, A. Kabas, O. Demircan, J. Alikakos, V. Charmandaris, G. Leto, J. Ohlert, J. M. Christille, R. Szakáts, A. Takácsné Farkas, E. Varga-Verebélyi, G. Marton, A. Marciniak, P. Bartczak, T. Santana-Ros, M. Butkiewicz-Bak, G. Dudziński, V. Alí-Lagoa, K. Gazeas, L. Tzouganatos, N. Paschalis, V. Tsamis, A. Sánchez-Lavega, S. Pérez-Hoyos, R. Hueso, J. C. Guirado, V. Peris, and R. Iglesias-Marzoa. The size, shape, density and ring of the dwarf planet haumea from a stellar occultation. *Nature*, 550(7675):219–223, oct 2017. doi: 10.1038/nature24051.

Daniel J. Price. Smoothed particle hydrodynamics and magnetohydrodynamics. *Journal of Computational Physics*, 231(3):759–794, feb 2012. doi: 10.1016/j.jcp.2010.12.011.

P.W. Randles and L.D. Libersky. Smoothed particle hydrodynamics: Some recent improvements and applications. *Computer Methods in Applied Mechanics and Engineering*, 139(1-4):375–408, dec 1996. doi: 10.1016/s0045-7825(96)01090-0.

Jessica D. Ruprecht, Amanda S. Bosh, Michael J. Person, Federica B. Bianco, Benjamin J. Fulton, Amanda A.S. Gulbis, Schelte J. Bus, and Amanda M. Zangari. 29 november 2011 stellar occultation by 2060 chiron: Symmetric jet-like features. *Icarus*, 252:271–276, may 2015. doi: 10.1016/j.icarus.2015.01.015.

P. J. G. Schreurs. Computational material models - lecture notes. *Eindhoven University of Technology, Department of Mechanical Engineering, Eindhoven, Netherlands*, 2014.

C. Schäfer, S. Riecker, T. I. Maindl, R. Speith, S. Scherrer, and W. Kley. A smooth particle hydrodynamics code to model collisions between solid, self-gravitating objects. *Astronomy & Astrophysics*, 590:A19, apr 2016. doi: 10.1051/0004-6361/201528060.

C.M. Schäfer, O.J. Wandel, C. Burger, T.I. Maindl, U. Malamud, S.K. Buruchenko, R. Sfair, H. Audiffren, E. Vavilina, and P.M. Winter. A versatile smoothed particle hydrodynamics code for graphic cards. *Astronomy and Computing*, 33:100410, oct 2020. doi: 10.1016/j.ascom.2020.100410.

R. Sfair and S. M. Giuliatti Winter. The role of mab as a source for the μ ring of uranusthe role of mab as a source for the μ ring of uranus. *Astronomy & Astrophysics*, 543:A17, jun 2012. doi: 10.1051/0004-6361/201117346.

Mark R. Showalter and Jack J. Lissauer. The second ring-moon system of uranus: Discovery and dynamics. *Science*, 311(5763):973–977, feb 2006. doi: 10.1126/science.1122882.

Mark R. Showalter, Jeffrey N. Cuzzi, and Stephen M. Larson. Structure and particle properties of saturn's e ring. *Icarus*, 94(2):451–473, dec 1991. doi: 10.1016/0019-1035(91)90241-k.

Joachim Gerhard Stadel. *Cosmological N-body simulations and their analysis*. University of Washington, 2001.

R. F. Stellingwerf and C. A. Wingate. Impact modelling with sph (invited paper). *Mem. Societa Astronomica Italiana*, 65:1117, January 1994. URL `https://ui.adsabs.harvard.edu/abs/1994MmSAI..65.1117S`.

Kai-Lung Sun, Martin Seiss, and Frank Spahn. Dust in the arcs of methone and anthe. *arXiv e-prints*, art. arXiv:1510.07722, October 2015. doi: 10.48550/arXiv.1510.07722. URL `https://ui.adsabs.harvard.edu/abs/2015arXiv151007722S`.

TheEfficientEngineer. `https://efficientengineer.com/`. Accessed: 2023-02-15.

Matthew S. Tiscareno, Philip D. Nicholson, Jeffrey N. Cuzzi, Linda J. Spilker, Carl D. Murray, Matthew M. Hedman, Joshua E. Colwell, Joseph A. Burns, Shawn M. Brooks, Roger N. Clark, Nicholas J. Cooper, Estelle Deau, Cecile Ferrari, Gianrico Filacchione, Richard G. Jerousek, Stéphane Le Mouélic, Ryuji Morishima, Stu Pilorz, Sébastien Rodriguez, Mark R. Showalter, Sarah V. Badman, Emily J. Baker, Bonnie J. Buratti, Kevin H. Baines, and Christophe Sotin. Close-range remote sensing of saturn's rings during cassini's ring-grazing orbits and grand finale. *Science*, 364(6445), jun 2019. doi: 10.1126/science.aau1017.

P. B. Siqueira V. Lattari, R. Sfair and C. M. Schaefer. Dust production through collisions between small-bodies: An application to the g-ring arc. *in preparation*, 2024.

Waloddi Weibull. A statistical theory of the strength of materials. *Generalstabenslitografiska anstalts foerlag*, 1939.

Appendices

Appendix A

Parameters of SPH simulations.

Table A.1: Material-Dependent Constants

	μ (GPa)	Y_0 (GPa)	E_{melt} (GPa)
Ice	2.8	1.0	0.7

Shear modulus μ, and yield stress Y_0 in SI units from Benz and Asphaug [1995].

Table A.2: Tillotson Eos Parameters

	ρ_0 (kg/m^3)	A_T (GPa)	B_T (GPa)	E_0 (MJ/kg)	E_{iv} (MJ/kg)	E_{CV} (MJ/kg)	a_T	b_T	α_T	β_T
Ice	917	9.47	9.47	10	0.773	3.04	0.3	0.1	10.0	5.0

Table A.3: Weibull distribution parameters for water ice.

Ice	m	k (m^{-3})	Reference
	9.1	1.0^{46}	Lange et al. [1984]
	9.6	1.4^{46}	Benz and Asphaug [1999]